Experimental demonstration of Displacement Noise Free Interferometry

by

Antonio Perreca

A thesis submitted to
The University of Birmingham
for the degree of
DOCTOR OF PHILOSOPHY

Astrophysics and Space Research Group
School of Physics and Astronomy
The University of Birmingham
June 2010

Abstract

General relativity describes gravity as the curvature of space-time. The theory predicts the existence of gravitational waves (GWs), which can be described as ripples in space-time propagating at the speed of light. So far no direct detection of GWs has been achieved. The sensitivities of the currently leading laser interferometric GW detectors are limited by various noise sources, i.e. seismic, thermal, shot noises etc.

Several conceptual studies are underway investigating new techniques that aim to improve sensitivities enough to fulfil the requirements of the next generation of detectors. One of these new techniques under investigation is displacement and frequency noise free interferometry (DFI). This thesis reports on the experimental demonstration of a new method of partial DFI that is effective in the GW detection frequency band.

The isolation of a mimicked GW signal from displacement noise of one mirror is demonstrated for a detuned Fabry-Perot cavity. A significant reduction in the displacement noise of the cavity input mirror was achieved by properly combining the reflected and transmitted signals from the cavity. This result represents the first experimental demonstration of this recently proposed DFI scheme, and lays the foundations for future work aimed at implementing DFI schemes in up-coming laser interferometric GW detectors.

…alla mia cara Mamma

Statement of originality

The thesis presents research work carried out the University of Birmingham, between September 2006 and March 2010.

Chapter 1 contains an introduction of the general topology of the current, second and third generation of GW detectors based on a review of papers already published. However the description of a proposed topology for third generation GW detectors is based on new original work reported in:
A. Freise, S. Chelkowski, S. Hild, W. Del Pozzo, A. Perreca, and A. Vecchio. ”Triple michelson interferometer for a third-generation gravitational wave detector.” *Classical and Quantum Gravity*, 26(8):085012, 2009,
of which I am one of the coauthors.

Chapter 2 provides a detailed description of the conceptual model for a proposed detuned Fabry-Perot (FP) cavity based DFI, largely taken from:
S. P. Tarabrin and S. P. Vyatchanin. ”Displacement-noise-free gravitational-wave detection with a single Fabry-Perot cavity: A toy model.” *Phys. Letters A*, 372:6801-6812, 2008.

Chapter 3 describes original work that I led and carried out in the laboratory for the construction of a full experimental setup to investigate the feasibility of the DFI technique in the low frequency region.

Chapter 4 details an analysis of a simulated detuned FP-cavity originally developed by myself for this thesis.

Chapter 5 shows a new experimental demonstration of the proposed detuned FP-cavity based DFI model, that I carried out (in collaboration with S. Chelkowski, S.

Hild and A. Freise). Material described in this Chapter (and partly in Chapter 3 and 4) provides the basis for a paper accepted by Physical Review D which I led:
A. Perreca, S. Chelkowski, S. Hild and A. Freise. ”Experimental demonstration of a Displacement noise Free Interferometry scheme for gravitational wave detectors showing displacement noise reduction at low frequencies.” *arXiv:0912.4749*, 2010.

Appendix A describes the original design of the Length and Sensing Control system for Advanced Virgo that I did in collaboration with S. Hild, M. Mantovani and A. Freise. This Chapter is largely taken from a document delivered to the Virgo Project:
S. Hild, M. Mantovani, A. Perreca, and A. Freise. ”Advanced virgo design: The advanced ligo approach for choosing modulation frequencies.” *Technical Report VIR-066A-08*, Virgo, 2009.

Appendix B provides original material that describes mathematically the homodyne detector features.

Appendix C is an additional analysis of a simulated detuned FP-cavity originally made by myself.

Appendix D contains the circuit diagrams of the electronic devices mainly used for the DFI experiment described in this thesis. These circuits have been designed by H. Vahlbruch and B. Hage with new inputs added by myself.

Contents

List of figures

List of tables

Glossary

AQ	amplitude quadrature
BS	beam splitter
BSH	beam splitter of homodyne detector
DFI	displacement noise free interferometry
DN	displacement noise
EM	end mirror
EOM	electro-optical modulator
FP	Fabry-Perot
FSR	free spectral range
FWHM	full width half maximum
GW	gravitational wave
HD	homodyne detector
HR	high reflectivity
HV	high voltage
IM	input mirror

LCGT	large-scale cryogenic gravitational wave telescope
LIGO	laser interferometer gravitational wave observatory
LO	local oscillator
LSCS	length sensing and control system
Mx	mixer
Nd:YAG	neodymium-doped yttrium aluminum garnet
OLTF	open loop transfer function
PBS	polarising beam splitter
PDH	Pound-Drever-Hall
PQ	phase quadrature
PRC	power recycling cavity
PRM	power recycling mirror
PZT	piezoelectric transducer
RO	relaxation oscillation
ROC	radius of curvature
SNR	signal to noise ratio
SRC	signal recycling cavity
SRM	signal recycling mirror
TDI	time delay interferometry
TF	transfer function
TN	thermal noise

Chapter 1.

Topology of Gravitational Wave detectors

1.1. Introduction

The search for gravitational waves goes back to the years between 1916 and 1918, when Albert Einstein predicted their existence as a direct consequence of the theory of General Relativity [Har03]. Until then Newton's principle of gravitation had been adopted according to which gravity propagates instantaneously.

Gravity is the weakest of the four known fundamental forces in nature and despite its weakness, its long range and attractive-only behaviour make it the shaping force in an astrophysical context. With the introduction by Einstein's of Special Relativity in 1905, and of General Relativity in 1915 our understanding of the gravitational force radically changed from the old Newtonian conception of infinitely fast propagation effect between bodies. The finite nature of the speed of light, according to GR, implies that gravitational signals must travel at a finite speed, the speed of light itself. General Relativity describes gravity as the curvature of the space-time, this implies that changes in the gravitational field of a body can be described as ripples in the space-time itself propagating with the speed of light. These ripples are called *gravitational waves*. To date no gravitational waves have been detected, even though strong indirect observational evidence exists in literature Hulse-Taylor Pulsar) [HT75].

Instruments now under construction are expected to provide direct detections of GW in the next few years. GW detection is possible by measuring the variation δl of the distance between two free masses at separation l. The wave amplitude h is defined by the ratio $\delta l/l$, but the predicted intensities are so tiny that they are expected to be of the order $h \approx 10^{-21}$. Gravitational wave detectors use this behaviour, looking for changes of the length of mechanical systems such as bars of aluminium [BM72] or in the arms of Michelson-type interferometers to reveal GWs.

Such detectors have to look for gravitational radiation from real astrophysical objects since it is not possible to generate detectable levels of such radiation artificially. The weak coupling of gravity with matter guarantees that the known matter in the present Universe is nearly transparent to gravitational waves. Thus the detection of such tiny space-time disturbances would not only be the most striking confirmation of General Relativity, but open a whole new branch in astronomy. The identification of sources using gravitational waves would allow the determination of their masses and distances independently fashion and thus a way of testing present cosmological models.

The sensitivity of the current GW detectors is limited by several noise sources.

One group, usually referred to as *displacement noises* (DNs), directly moves the reflective part of the test masses. Future GW detectors are expected to be limited by displacement noise such as seismic noise, gravity gradient noise, thermal noise and radiation pressure noise at frequencies below 100 Hz. Several studies are currently ongoing to create a new generation of GW detectors with a strongly improved sensitivity [FCH$^+$09]. In a context of future GW detectors a new idea called displacement and frequency noise free interferometry (DFI) was proposed by S.Kawamura and Y.Chen [KC04]. DFI is based on the fact that gravitational waves and displacement noise as well as frequency noise affect the light in a different manner and aims at reducing all displacement noises and frequency noise simultaneously. The realisation of an experiment with multiple read-out channels where each single channel carries the gravitational wave signal and the noise information differently allows the creation of a channel that is completely free from laser and displacement noises [CK06, CPS$^+$06].

However the current experimental demonstrations of DFI have been carried outside the GW detectors frequency band. Recently a new DFI scheme has been proposed which works in a low frequency region. A detuned Fabry-Perot (FP) cavity configuration [TV08] in combination with two lasers is used to partially remove the displacement noise from both cavity mirrors. One laser is used for the input cavity mirror (IM) and one is used for the end cavity mirror (EM) (Double Pumped Fabry-Perot cavity). This thesis is aimed at the first experimental proof of DFI in the GW detector frequency band providing the demonstration of the principle of the detuned FP-cavity based DFI scheme proposed in [TV08]. Here one laser is used in combination with two homodyne detectors to suppress strongly the displacement noise of the input mirror of a FP-cavity with respect to a simulated GW signal. As a result we obtain a gain in the GW signal to displacement noise ratio in the whole frequency range of interest of ~ 60.

1.1.1. Structure of the thesis

The aim of this thesis is to describe the first experimental demonstration of displacement noise free laser interferometry (DFI) in the gravitational wave detection band. The structure follows a logical order to provide the basic concept of DFI before the individual steps necessary for the experimental proof are presented.

Chapter 1 is an overview of the topology of current and future generations of GW detectors. The basic principle of the detection and limitations of GW detectors are provided.

Chapter 2 provides an overview of displacement noise free laser interferometry with a more detailed description of the conceptual model for a proposed detuned Fabry-Perot cavity based DFI.

Chapter 3 provides a description of the experimental setup with all its optical and electronic components. It is shown that the experimental demonstration of the proposed detuned FP-cavity DFI scheme can be performed with the use of a single laser.

Chapter 4 provides the description of a simulated detuned FP-cavity. Some features of the homodyne detector angle are studied to build the basis of the experimental measurements. GW signals and DNs are simulated and consequently used to show the feasibility of the proposed detuned FP-cavity based DFI model.

Chapter 5 describes the measurements made to demonstrate the validity of the proposed scheme. GW and DN measurements are made and consequently used to give an experimental proof of the new DFI scheme. The gravitational wave wave signal to displacement noise ratio is improved in the frequency range of 10 Hz to 10 kHz with a typical factor of ~ 60.

In Chapter 6 an overview of the experiment and relative use of the detuned FP-cavity for future gravitational wave detectors are presented.

Appendix A describes the design of the length sensing and control system (LSCS) of the Advanced Virgo interferometer.

1.2. Principle of detection with a Michelson Interferometer

A Michelson interferometer is a device that detects the interference at the output of two light beams travelling along its arms which are at 90° angle to each other. It translates differences between the length of the arms into differences in phase of its two beams. Fig. 1.1 shows the GW effect on a Michelson interferometer, where for simplicity the GW is assumed travelling orthogonal to the interferometer plane.

In order to understand the principle of detection with a Michelson it is worthwhile to consider its response to a sample GW signal.

A sinusoidal GW with amplitude h and frequency f_{gw} can be written as follows, for simplicity optimal GW polarisation and directions are assumed :

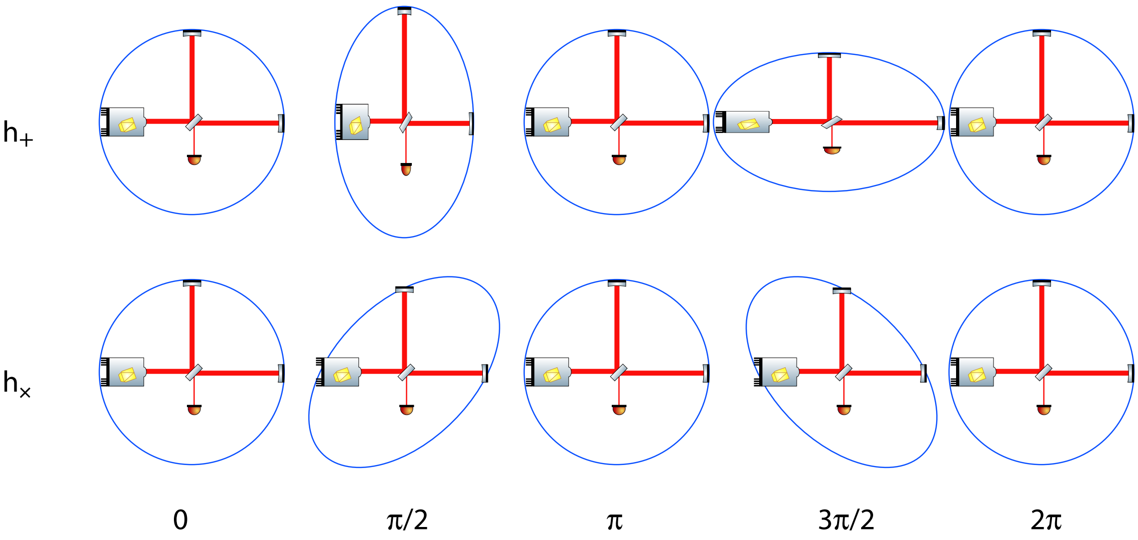

Figure 1.1.: In a Michelson interferometer the laser light is divided in two equal beams which travel along the arms, reflect on the mirror and travel back to the output interfering with each other. The circle in the image represents the space occupied by the interferometer, and its distortion as a sample gravitational wave passes through. From left to right the distortion is shown for the two possible gravitational wave polarisations (h_+) and (h_x). This plot is taken from [Che07].

$$h(t) = he^{i2\pi f_{gw} t} \tag{1.1}$$

The light pumped from the laser at frequency f takes a time $\tau = 2L/c$ to travel one round trip in each arm of length L. When a GW interacts with the detector it changes the two arms length and the light takes a different round trip time. This difference can be translated into phase difference at the output of the detector which can be expressed as [Sau94]:

$$\Delta\phi(t) = h\tau \frac{2\pi c}{\lambda} sinc(f_{gw}\tau) e^{i\pi f_{gw}\tau} \tag{1.2}$$

where λ is the light source wavelength and $sinc(f_{gw}\tau) = \sin(\pi f_{gw}\tau)/(\pi f_{gw}\tau)$. Thus the GW affects the travelling light by modulating the light phase at the GW frequency f_{gw} with a modulation index of $(2\pi/\lambda)\sin(\pi f_{gw}\tau)/(\pi f_{gw}\tau)$. It is interesting to notice that the term $\sin(\pi f_{gw}L/c)$ can be maximised by choosing the optimal interferometer arm length $L \sim c/f_{gw}$ to let the detection be more sensitive at a specific GW frequency f_{gw}. In other words, in Fig. 1.2 it can be seen how the modulation varies with arm length and frequency. For GW frequencies below 1 kHz the maximum of the modulation index occurs for arm lengths of at least 75 km, that is in practice too long for ground-based GW detectors. However advanced optical techniques are used to enlarge the optical path of the laser light which results in an increased detection sensitivity.

It is worth noticing that the phase difference $\Delta\phi$ at the output of the interferometer is translated into optical power sensed by a photodetector as follows [Sau94]:

$$P_{out} = \frac{P_{in}}{2}(1 + \cos 2\Delta\phi) \tag{1.3}$$

where P_{out} is the power at the output and P_{in} is the power of the light source. This shows that the GW signal is proportional to the input power (P_{in}).[1]

1.3. Ground based gravitational wave detectors

In order to detect gravitational waves, current detectors are now taking data. One is LIGO (*Laser Interferometer Gravitational wave Observatory*). That comprises three devices: one in Livingston, Louisiana; the other two in Hanford, Washington.

---

[1] The GW signal can be detected at the output of the interferometer with modern techniques (as 'heterodyne technique') which ensures that the GW signal is proportional to the illuminating light whilst the working point of the detector is at the dark fringe ($P_{out} = 0$) [Miz95].

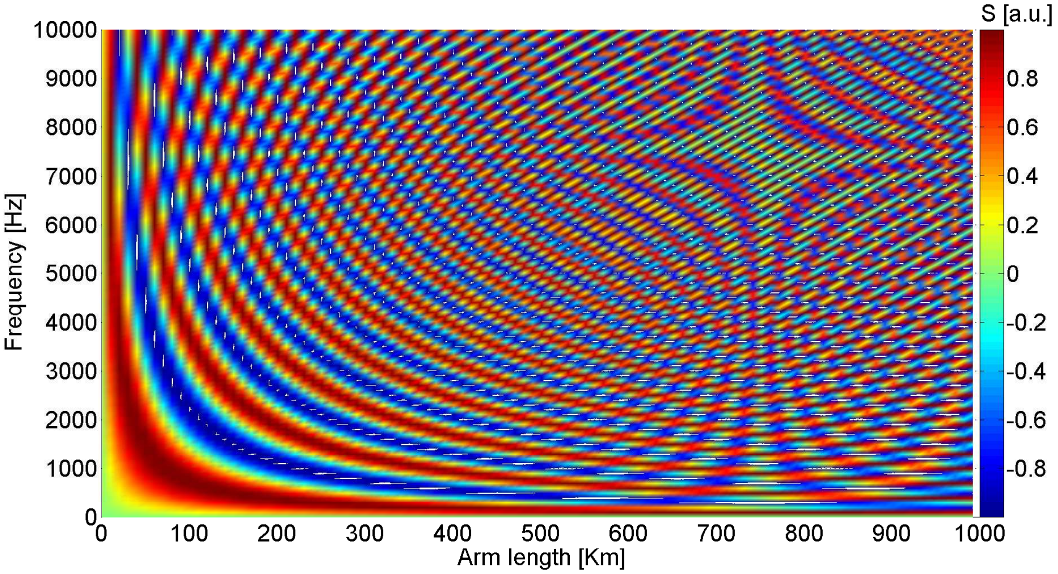

Figure 1.2.: Michelson sensitivity for a simultaneous scan of arm length and gravitational wave (GW) frequency. A GW modulates the phase of the traveling light at GW frequency itself. The interferometer design can be optimised to its sensitivity (S) GW band by using an optimal arm length. The red bands represent the maximum Michelson normalized sensitivity for any frequency and arm length. The sinusoidal contribute to the modulation index shows the repetition of the red band. The first band is the most significant one. For GW frequencies below 1 kHz the optimal arm length starts from 75 km.

Those are Michelson interferometers whose arms are 2 and 4 kilometers in length [BW99].

The French/Italian Virgo detector [AAA+08], whose arms are 3 km long has a good low-frequency sensitivity, down to 10 Hz. It is located at Cascina (Pisa).

The Japanese TAMA300 detector, which has arms of 300 m length, is located at the TA0 Tokyo Astronomical Observatory [TTA+07].

These interferometers have resonant cavities in the arms of the detectors and also they use a technique known as *power recycling* (see Sec. 1.3.2) by placing a mirror,

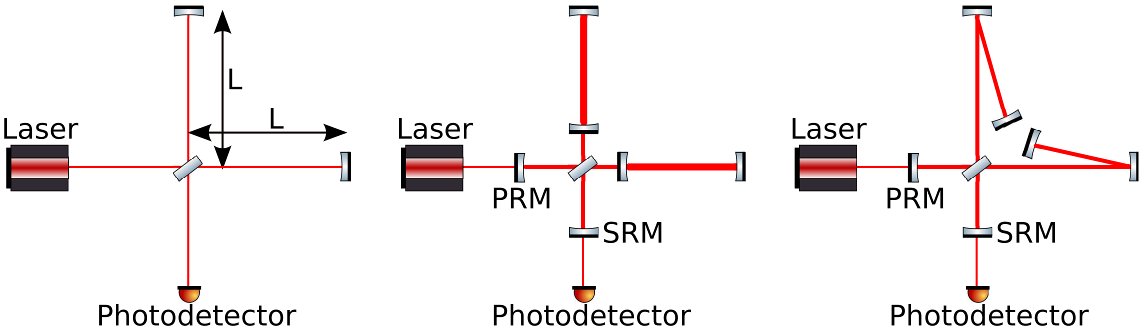

Figure 1.3.: GW wave detector layout. On the left is shown the basic layout of a Michelson. In the middle is shown a Michelson with Fabry-Perot cavities in its arms and with the power and signal recycling mirrors (PRM, SRM). On the right a folded Michelson with delay-lines and the power and signal recycling mirrors. This plot is taken from [Che07].

named power recycling mirror (PRM), between the laser and the beamsplitter to increase the power into the detector [Mee88].

The German/British detector, GEO600, whose arms are 600 m long, is different [WAA$^+$04] from the others. It does not have cavities in the arms but it makes use of a delay line system and a technique called *signal recycling* (see Sec. 1.5.1) [HSM$^+$98, MS91, SM91, FHS$^+$00]. This technique provides a signal enhancement as a mirror at the output, named signal recycling mirror (SRM), sends the signal sidebands back into the interferometer (see Fig. 1.3).

1.3.1. Delay line and Fabry-Perot cavity

The optimised sensitivity of GW detectors requires very long arms which is unrealistic for ground based interferometers. To increase the effective length of the arm the optical path can be folded in a way that the travel time of the light between the test masses is increased. This means that the light experiences a longer interaction time with GWs and accumulates a bigger phase shift resulting in a greater sensitivity of the instruments. The time, τ_s, the light needs to leave the interferometer is called *storage time*. The folding techniques, used so far, include Fabry-Perot cavity or Delay-lines into the arms [FBBM86].

For a Michelson interferometer with delay lines, in the ideal case of folding mirrors with reflectivities of unity, the storage time is:

$$\tau_{s,dl} = 2L/c \tag{1.4}$$

where L is the length of the total optical path. The bandwidth of this kind of interferometers can be estimated as:

$$\Delta f_{dl} = 1/2\tau_{s,dl} \tag{1.5}$$

The transfer function of such instruments can be obtained by replacing τ with $\tau_{s,dl}$ into equation 1.2

$$\Delta\phi_{dl} = h(t)\tau_{s,dl}\frac{2\pi c}{\lambda} sinc(f_{gw}\tau_{s,dl})e^{i\pi f_{gw}\tau_{s,dl}} \tag{1.6}$$

On the other hand the definition of storage time in a Fabry-Perot cavity is a little different from the delay lines case since the light photons have a different storage time from each other. Here the storage time is intended as the average time of a photon which remains in the cavity.

For a Fabry-Perot cavity of length L, with the input cavity mirror of reflectivity of

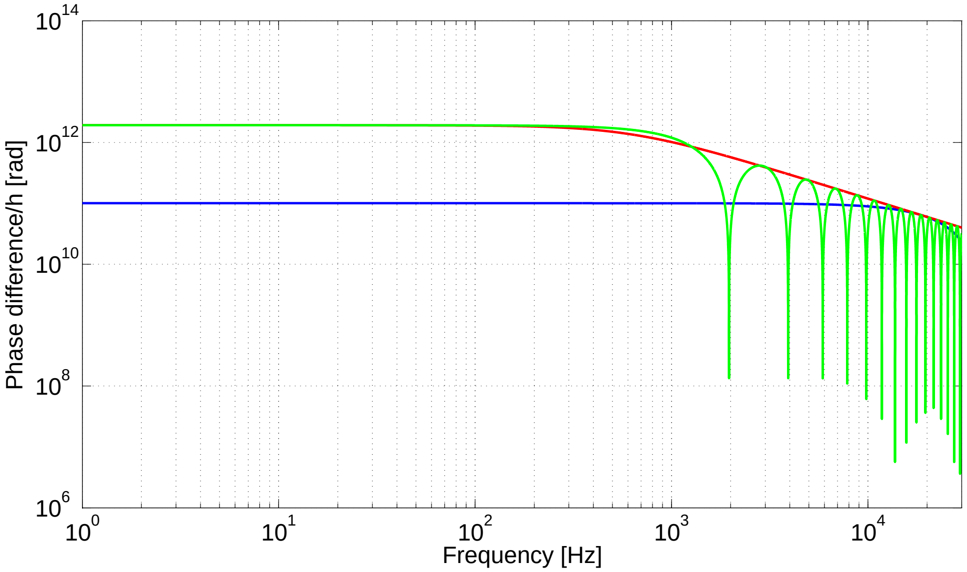

Figure 1.4.: GW response comparison between a folded and a non-folded Michelson. The detector is pumped with light of wavelength $\lambda = 0.5\mu$m. The blue curve shows the transfer function normalised to h of a non-folded Michelson of 4 km arm length. The sensitivity shows a magnitude of 10^{11} rad and a bandwidth of 18 kHz. The red curve represents the transfer function normalised to h of a Michelson folded with FP cavities of length of 4 km and finesse of 30 in its arms. The sensitivity improves up to $2{\cdot}10^{12}$ with a smaller bandwidth of 600 Hz. The green curve shows the sensitivity of a Michelson with a delay-line, of $\sim$ 150 km, showing a wider bandwidth and notch points at which this detector type are insensitive to gravitational waves.

unity, the light storage time is given by [Sau94]

$$\tau_{s,fp} = \frac{F}{2\pi \cdot FSR} = \frac{L}{c}\frac{F}{\pi} \tag{1.7}$$

where F is the cavity *finesse* and FSR is the *Free Spectral Range* of the cavity (Section 3.3.1). The bandwidth of the cavity is given by:

$$\Delta f_{fp} = FSR/2F \approx 1/4\pi\tau_{s,fp} \tag{1.8}$$

which differs by a factor of 2π from the bandwidth Δf_{dl} of a folded interferometer with delay lines.

The response of this folded interferometer can be expressed as [Mee88]

$$\Delta\phi_{fp} = h\tau_{s,fp}\frac{8\pi c}{\lambda}\frac{1}{\sqrt{1+(4\pi f_{gw}\tau_{s,fp})^2}} \tag{1.9}$$

where it can be seen that the cavity behaves as a one pole filter. It is important to notice that in the limit $f_{gw}\tau_{fp} \gg 1$ (*time-storage limit*) the response can be approximated as

$$\Delta\phi_{fp} \approx \frac{2c}{\lambda f_{gw}} \tag{1.10}$$

where the response is inversely proportional to GW frequency and is not dependent on the storage time. This represents the upper limit of the storage time above which the cavity negatively affects the response of the detector. Note that all the considerations are under the condition of a GW travelling orthogonally the plane where the detector is sitting.

It is interesting to compare the GW response between the two designs types and the non-folded Michelson interferometer shown in Fig. 1.4. The blue curve shows the transfer function normalised to h of a non-folded Michelson of 4 km arm length. The sensitivity shows a magnitude of 10^{11} rad and a bandwidth of 18 kHz. The red curve represents the transfer function normalised to h of a Michelson folded with cavities of length of 4 km and finesse of 30 in its arms. The sensitivity improves to $2 \cdot 10^{12}$ rad with a lower bandwidth of 600 Hz. If one wants to consider a Michelson with a delay-line, the same sensitivity can be reached with an arm length of $\sim$ 150 km, which is given by $4c\tau_{s,fp}$. The green curve shows such response. It can be noticed there is a higher bandwidth of 2π and several notch points at which the detector is completely insensitive to GW. With a price of narrower bandwidth the Fabry-Perot has the advantage of not having any points at which the detector is insensitive to GW's. Furthermore the longer the time storage in the delay-line interferometer the more the notch points are at lower frequencies.

1.3.2. Power Recycling cavity

As discussed previously the interaction of GW's with detectors affects the phase of the travelling light which has a maximum when the storage time of the light is half the GW period. This phase shift is measured at the output of the interferometer while it is held in its working point when the beams experience destructive interference on the beam splitter, the so called dark fringe. Then almost the whole amount of light returns back to the laser. Positioning a partially reflective mirror, as shown in Fig. 1.3, the PRM mirror, this returning light, in phase with the 'new' light coming from the laser, is recycled by the interferometer. In other words the PRM creates an additional cavity between the PRM itself and the two input cavity mirrors, resulting in a similar interferometer with a more powerful light source. This also means that the power recycling does not change the frequency shape of the detector response, rather it improves sensitivity by a scaling factor proportional to the power stored inside the interferometer [Miz95]. This can be seen as a consequence of improvement in the shot noise (see sec.1.4.1) which is the limitation of the sensitivity of GW detectors at frequencies above 500 Hz.

1.4. Limiting noise sources

Recalling that GW detectors aim to measure variations of distance between their mirror test-masses, which result in a tiny phase difference between the travelling light inside the two arms, their sensitivity to GW detection is limited by undesirable sources which can completely mask the GW signal. The limiting noise sources can be divided in two main categories:

- *Phase Noises* are spurious signals which affect directly the phase of the traveling light inside the interferometer;
- *Displacement Noises* (DNs) are spurious signals which impose position variations of the mirrors test masses.

1.4.1. Sources of Phase Noise

Shot noise

Fluctuations of the detected photocurrent, the so called shot noise, impose a limitation in the sensitivity given by the optical readout scheme. This noise originally comes from the quantisation of the light energy on the photodetector.

Considering that a number of photoelectrons measured in a time τ obey Poisson statistics it can be shown for a simplified model [Cav80, Cav81] that the displacement sensitivity is a function of laser power (P_{in}), the wavelength (λ) of the laser, the arm length L, and a bandwidth Δf as follow:

$$h_{sn}(f) = \frac{1}{L}\sqrt{\frac{\hbar c \lambda}{4\pi P_{in}}} \tag{1.11}$$

where c is the velocity of light and $\hbar$ is the reduced Planck's constant. This equation shows that the photon shot noise is described by a white amplitude spectral density. Thus improvements in sensitivity can be obtained either by increasing the power of the laser or increasing the arm length. It must be noticed that since the shot noise is proportional to $\sim \sqrt{P}$ and the GW signal is $\sim P$ then GW signal to shot noise ratio is proportional to $\sim \sqrt{P}$.

Radiation Pressure noise

In GW interferometers the amount of measured light at the output is related to the differential phase between the two light beams coming from the arms after bouncing from the mirror test-masses. This photon bouncing causes a recoil effect on the atoms in test masses which can affect the measurement of the phase of the light at the output as radiation pressure noise. Thus high power increases the fluctuations in radiation pressure on the mirrors and it can be shown that for a simple Michelson interferometer the displacement sensitivity is given by [HRS05, Sau94]:

$$h_{rp}(f) = \frac{1}{m f^2 L}\sqrt{\frac{\hbar P_{in}}{2\pi^3 c \lambda}} \tag{1.12}$$

where m is the mass of the mirror test mass. Here it can be notice that the radiation pressure noise, at despite of shot noise, is proportional to $1/f^2$ and to $\sqrt{P_{in}}$ [Cav80]. Thus high power improves the shot noise at the price of increased radiation pressure noise at low frequency.

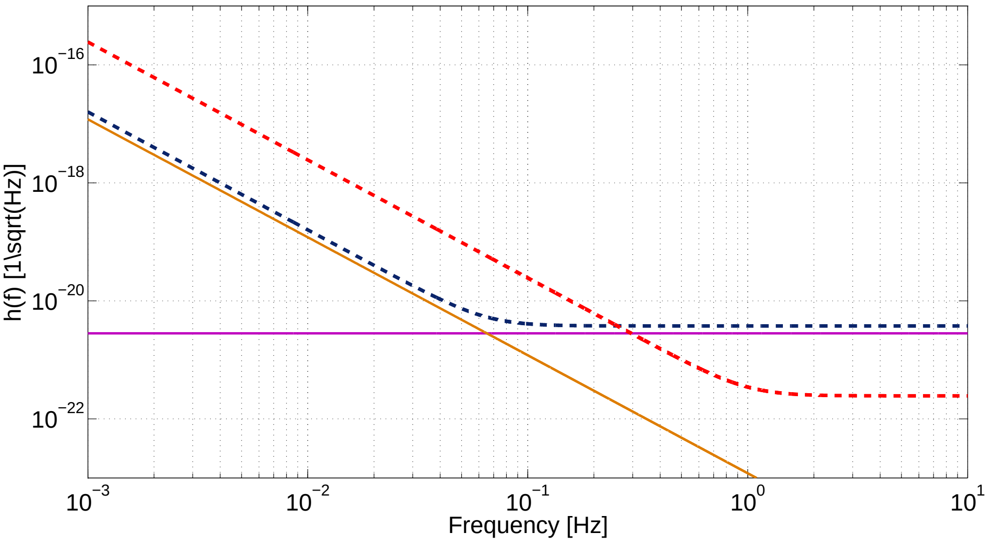

Figure 1.5.: Shot noise and radiation pressure noise amplitude spectral density. The considered interferometer is a 4 km Michelson interferometer with test masses of 10 kg and laser light of wavelength $\lambda = 0.5\,\mu$m at $P_{in} = 20$ W. The orange curve is the radiation pressure noise. The pink curve is the shot noise and the corresponding readout noise is dark-dashed line, which is the sum of the two contributes. For laser light power at 4.7 kW the minimum of the amplitude spectral density is at 1 Hz.

A compromise between these two complementary noises at any frequency is given by choosing $P_{in} = P_0$ as follows:

$$P_0 = \pi \lambda c m f^2 \tag{1.13}$$

which represents the value of P_{in} at which shot noise and radiation pressure are the same giving the minimum noise spectral density.

Fig. 1.5[2] shows plots of the amplitude spectral density of the shot noise and radiation pressure for a 4 km Michelson interferometer with test masses of 10 kg and laser light of wavelength $\lambda = 0.5\,\mu$m at $P_{in} = 20\,$W. It is possible to notice that at low frequency the radiation pressure noise (orange curve) is dominant while the shot noise (pink curve) dominates at higher frequency. These two noises can be described as one noise called *readout noise* (dark-dashed curve). Thus if, for example, one wants to have the minimum spectral density at 1 Hz (red-dashed curve) the relative light power is $P_0 = 4.7$kW.

Laser frequency noise

Amplitude and phase variations of the light sources can cause undesirable noise at the interferometer output. Small imperfections of the optical cavity lengths ΔL_c results in an additional phase shift which couples to the light as follows [HWK+91, CYWM00]:

$$\varphi_s = \frac{4\pi\Delta L_c}{\lambda}\delta_s^2(f) \tag{1.14}$$

where $\delta_s^2\ Hz/\sqrt{Hz}$ is the spectral density of the light fluctuations and λ is the wavelength of the light source. Imperfections $\Delta L_c/L \approx 1\%$ in the arms optical path admit a maximum fluctuation in spectral density of 10^{-5}Hz/$\sqrt{\text{Hz}}$.

---

[2] A revised version of readout noise can be found in [Cor08].

Residual gas noise

Propagation of light depends on the refractive index, thus fluctuations of gas density generate variations of the optical path. The phase difference when air travels in the air and vacuum is [Sau94]:

$$\phi = (n_{air} - 1)\frac{2\pi}{\lambda} \tag{1.15}$$

where n_{air} is the refractive index of air. Therefore it is necessary to keep both the arms under vacuum at the same pressure and temperature.

1.4.2. Sources of Displacement Noise

Seismic noise

This is a noise coming from the earth shaking. In a very quiet place the seismic spectral density is [BBB^{+}01, HRS05]:

$$h_s \approx 10^{-7} f^{-2}\, m/\sqrt{Hz} \tag{1.16}$$

In order to obtain a 'good' detector sensitivity over a certain range of frequency, the displacement of each test mass has to be attenuated by a factor greater than 10^9 in the horizontal direction. Since the coupling between vertical and horizontal movements is of the order of 10^{-3}, isolation in the vertical direction is required [HRS05]. The isolation in the horizontal direction is performed by using a multistage pendulum, which can be seen as a low-pass filter. In other words if one considers a single pendulum system, the transfer function from the suspension point to the mass shows a resonance frequency above of which this response falls off behaviour as f^{-2}. On the other hand vertical isolation is reached with the suspension of a mass on a spring.

In the Virgo detector the seismic noise is attenuated in the vertical direction to a useful level with the adoption of a seven stage horizontal pendulum system with six of the upper stages suspended by cantilever springs [BV02]. A triple pendulum system is adopted for the GEO600 detector (operation down to 50 Hz). This system has the first two stages hung from cantilever springs to provide the needed vertical isolation [Gos04].

Gravity Gradient noise

This noise can be associated with the time variability of the matter surrounding the detector. When the matter changes its distribution it causes the fluctuations of the gravitational field which couple directly to mirrors test masses [Sau84]. Thus gravity gradient noise can be seen as a consequence of seismic noise and its amplitude spectral density, for an interferometer with mirrors test masses separated by L, can be written as follows

$$h_G = \frac{1}{L}\frac{2G\rho}{3\sqrt{\pi}}\frac{h_s}{f^2} \tag{1.17}$$

where G is the gravitational constant, ρ is the density of the matter surrounding the test masses and h_s is the amplitude spectral density of the seismic noise.

Fig. 1.6 shows the noise contributions due to seismic and gravity gradient in a Michelson located in a place where the seismic noise is modelled differently from equation 1.16. In a very quit place the seismic noise is dominant. The gravity gradient noise currently is not limiting the sensitivity of the ground based interferometers.

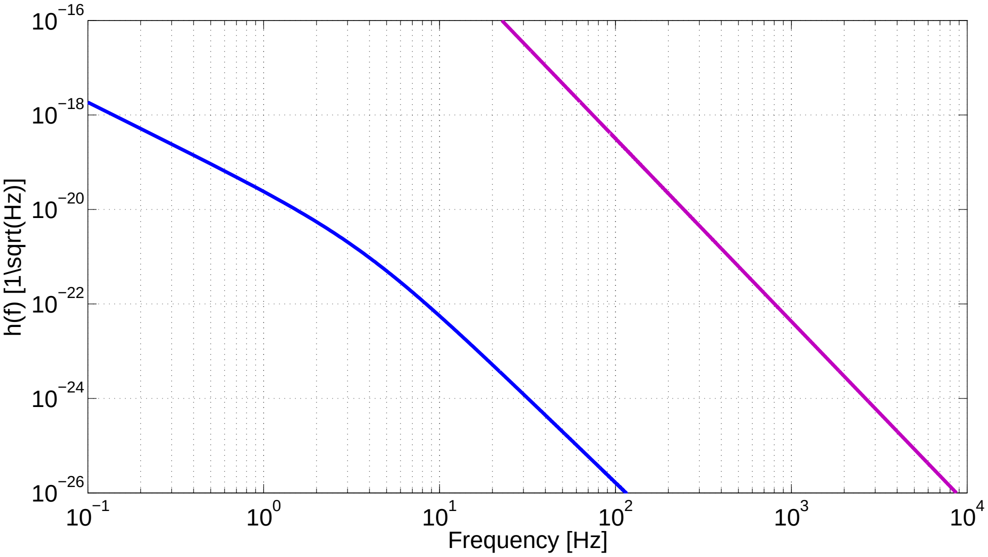

Figure 1.6.: Seismic and gravity gradient amplitude spectral density noise. The considered Michelson interferometer is 4 km long with test masses suspended from a 10 m pendulum system. The pink curve represents the seismic noise and the blue curve the gravity gradient noise.

Thermal noise

One more fundamental noise source is due to the fact that the mirror used as test masses are at finite temperature. Consequently the atoms which comprise the masses, as well as the wires used for the suspension, vibrate. Vibrations of the test mass atoms cause vibrations of mirrors which can cover the GW signal [Sau90, Lev98, SY09].

One aspect of thermal noise can be associated with the Brownian motion of atoms forming the suspended mass system. The internal friction of the material dissipates energy causing noise. Thus the *fluctuation-dissipation theorem* gives an important relation between the resulting displacement of the test masses and the dissipation of the material. In particular the thermal noise, $h_{tn}(f)$, associated to a pendulum system with a resonance frequency f_0, is given by [Sau94, HRS05]:

$$h_{tn}(f) = \frac{k_B T f_0^2 \phi(f)}{2\pi^3 f m[(f_0^2 - f^2)^2 + f_0^4 \phi^2(f)]} \tag{1.18}$$

where k_B is the Boltzmann constant and $\phi(f)$ is the mechanical dissipation factor of the oscillator of mass m at temperature T. From this equation can be noticed that at resonance frequency the thermal noise is proportional to $1/\phi$. Thus the higher the dissipation of the material the lower is the resonance peak resulting in the same time in a larger frequency range of the thermal noise. For this reason the current GW detectors use material for the suspensions with a low dissipation factor (e.g. fused silica is used for the test masses). In particular GEO600 uses fused silica fibers also for the suspensions in contrast with the Virgo, LIGO and TAMA300 detectors where carbon steel wires are used.

It can be also noticed from equation 1.18 another feature of the pendulum system which imposes a low thermal noise spectrum for frequency above the resonance frequency. Indeed at frequency higher than f_0 the thermal noise spectrum shows a $1/f^5$ slope. It has to mentioned also that test masses are designed in a way that their internal modes are located at very high frequency (order of kHz) in order to avoid any disturb in the GW frequency band while the wires present longitudinal modes around 1 Hz and transverse modes around hundreds of Hz. For this reason the transverse modes, called also violin modes, are present in the sensitivity curves of the current GW detectors. One other aspect of the thermal noise which can be relevant in the current GW detectors is associated with the so called thermoelastic noise where the dissipation is due to the temperature fluctuation which couples with thermal expansion of the material [HRS05].

1.4.3. Sensitivity

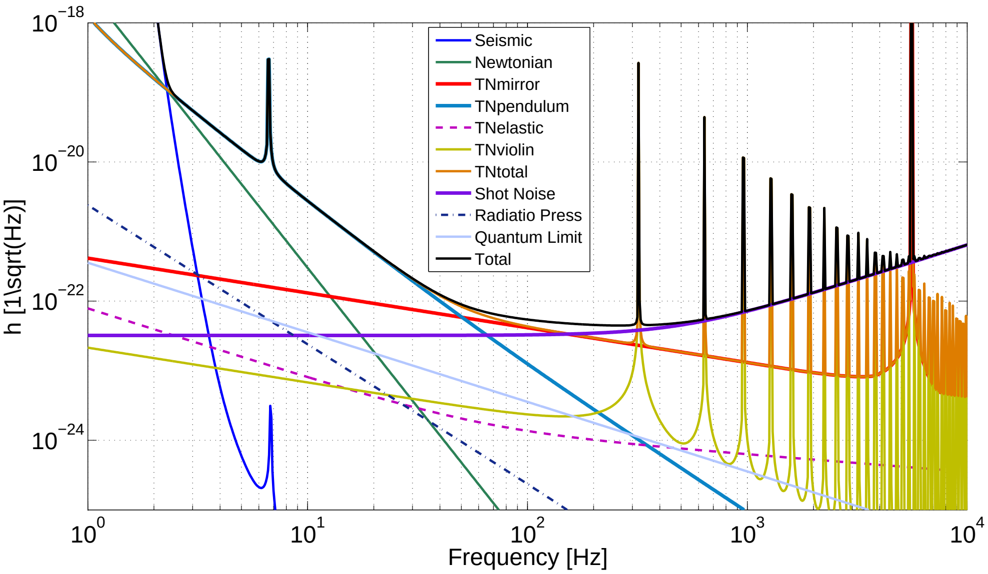

Figure 1.7.: Virgo design sensitivity. Seismic, pendulum TN, mirror TN and shot noises limit the Virgo designed sensitivity. Violins transversal modes are also shown in the sensitivity curve. This plot is taken from [Pun04].

The noise sources mentioned above cause unwanted spurious signals which limit the detector sensitivity. The sources of noise affect the sensitivity in a different manner over the frequency range. In Fig. 1.7 the Virgo design sensitivity can be seen. The designed sensitivity sets limitation on the GW detection mainly at low frequency where seismic and pendulum thermal noise (TN) are dominant respectively up to ∼ 3 Hz and up to ∼ 50 Hz. In high frequency band, starting from ∼ 300 Hz limitations are due to the shot noise. In this band the violin transversal mode of the wires can also be noticed. In the middle frequency range, where the detector is most sensitive, limitations are due to the mirror TN.

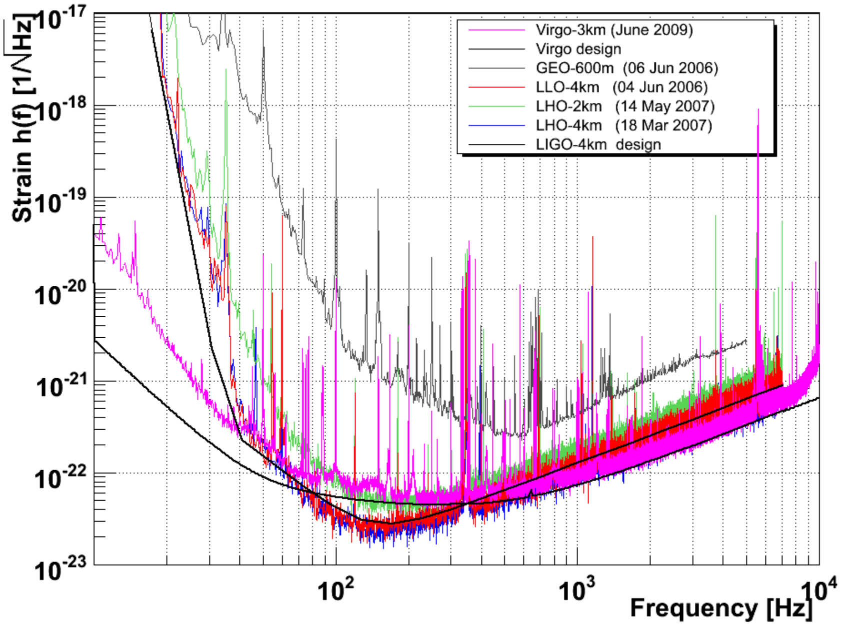

Figure 1.8.: Ground based GW detector sensitivities. LLO-4 km is the LIGO detector in Livingston; LHO-2 km and LHO-4 km are the two detectors in Hanford respectively 2 and 4 km long. Virgo shows the best performance at frequencies below 40 Hz and matches LIGO LHO-4 km sensitivity which is very close to its design. The experimental sensitivity in Virgo below 200 Hz is still far from its design. This plot is taken from [AAA$^+$08].

In 2007 the collaboration between LIGO and Virgo started with the purpose of sharing and analysis of data. Fig. 1.8 shows the comparison between LIGO, Virgo and GEO sensitivities. It can be seen that at high frequency Virgo matches the LIGO LHO-4 km (LIGO 4 km long in Hanford) sensitivity and it has the best performances at frequencies below ∼ 40 Hz. In the intermediate frequency band Virgo sensitivity is worse than designed. In this band LIGO is better by almost one order of magnitude.

However, the main GW sources are expected to be in the frequency range, up to hundreds Hz, as signals emitted by binaries Neutron Stars (NS-NS) binaries Black Holes (BH-BH) and at higher frequency signals emitted by pulsars and NS. Given a higher sensitivity further can be the sources, thus an improvement of one order of magnitude of the sensitivity would increase the probability of the detection. For example detection of GW from NS-NS would increase the event-rate (per year) from 0.1 to 500, while the event-rate of BH-BH could be even of the order of thousands higher [HRS05]. For this reason the second generation of GW detectors is essential.

1.5. Second generation GW detectors

Although current GW detectors have performed long-duration data recording runs, sensitivities have to be improved to make the detection possible. During the next decade an upgrading of all of these interferometers is scheduled, the so-called *second-generation* instruments. The second generation of laser interferometric detectors aim to improve their sensitivities by one order of magnitude over the whole frequency range of interest. This generation of GW detectors is represented by Advanced LIGO [Fri03], Advanced Virgo [FFG$^+$05], LCGT [KtLC06] and GEO-HF [WAA$^+$06] and are planning advanced technology upgrades of the existing detectors, i.e. high laser power, new materials, etc.

The noise anatomy of Advanced LIGO is shown in figure 1.9. The use of a higher power laser will be one of the upgrades of the GW detectors. This will improve the sensitivity at high frequency at the price of higher radiation pressure noise, which will be dominant at low frequency. In the middle frequency band the mirror TN gives the limit to the Advanced LIGO sensitivity. The reduction of coating thermal noise (in Fig. 1.9 referred as 'internal noise') forms a significant challenge to be overcome in designing the second generation of GW detectors. All advanced detectors will implement the SRM between the output and the beam splitter as shown in Fig. 1.3.

1.5.1. Signal recycling

One of the parameters which affects a detectors sensitivity is the power of the light stored in the device. It has to be mentioned that high light power, with use of

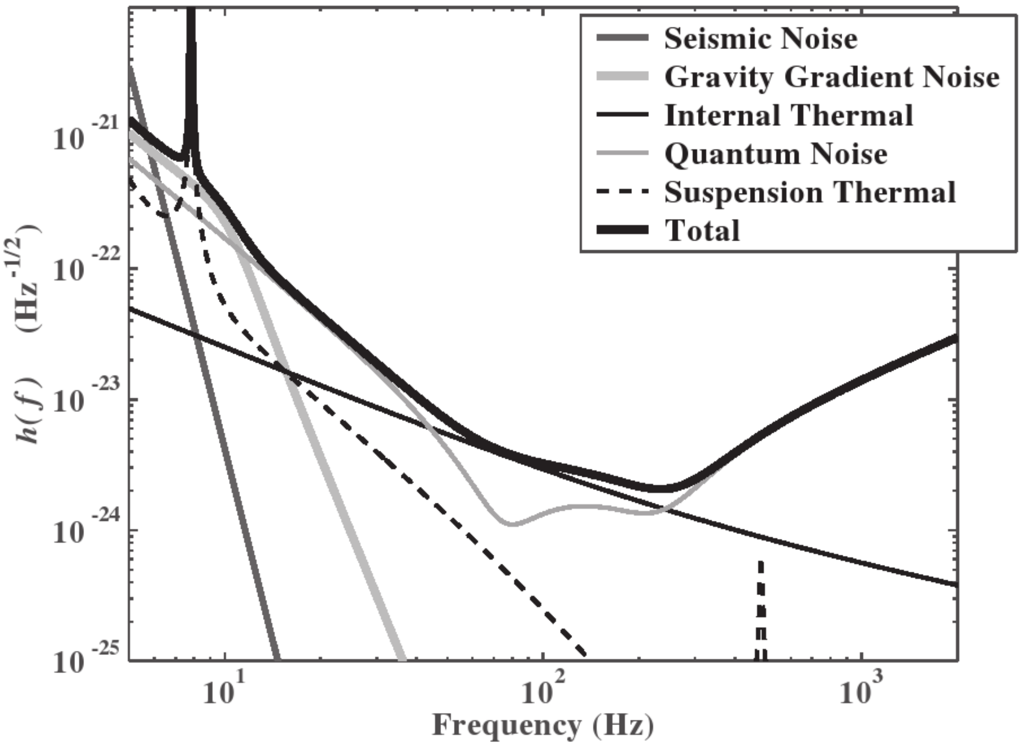

Figure 1.9.: Advanced LIGO sensitivity. The next generation of LIGO will be limited in sensitivity at low frequency by the radiation pressure noise and at high frequency by the shot noise. The middle range is dominated by the coating thermal noise. This plot is taken from [HRS05].

a FP-cavity or delay lines, influences the light storage time in the arms [Hei99]. The longer the storage time the greater the interaction time of light with GWs. However there is an upper limit of the storage time above which the sensitivity of the device decreases as $1/f$. It has to be noticed that when GWs arrive the interaction with light produces sidebands inside the interferometer. If no recycling and no FP cavities are used the GW sidebands (or signal sidebands) will leave the interferometer quickly. A signal recycling cavity will be adopted in the second generation of GW detectors to increase the signal storage time (as in GEO600 provided by delay lines which double the optical path to 1200 m). In this case the signal sideband is resonant in the SRC. The SRC keeps the GW sidebands trapped inside the interferometer where they are enhanced by the resonance factor of the signal recycling cavity itself. The drawback of this technique is a correspondingly narrower bandwidth.

In an optical setup with arm cavities this could be a limitation since high finesse arm cavities cannot be used. Indeed high finesse is obtained with high reflectivities of the the cavity mirrors thus light could leave the arms after too much time. In Advanced LIGO and Advanced Virgo the use of the signal recycling cavity can be modified by placing the SRM roughly in the same position of the previous case and adding some detuning to the SRM position. In this case the signal storage time decreases independent of the finesse of the arm cavities, widening the bandwidth compared to the configuration with the power recycling cavity only. When the tuning of the cavity is such that the signal sideband is anti-resonant in the recycling cavity the technique is called *resonant sideband extraction* [HSM$^+$98, MS91, SM91, FHS$^+$00]. Benefits of this configuration are that it allows the use of high finesse in the arm cavities and consequently high power stored in the arms, thus the enhancement from the power recycling can be reduced. In turn this means that less power light passes through optics and then less thermal lensing effects are experienced.

Fig. 1.10 shows an example of the effect of the SRM at transmittance $T_{MSR} = 2\,\%$ in GEO600 with a light power of 1.8 kW. It can be noticed that for zero detuning (signal recycling) has a higher sensitivity at the price of a narrower bandwidth.

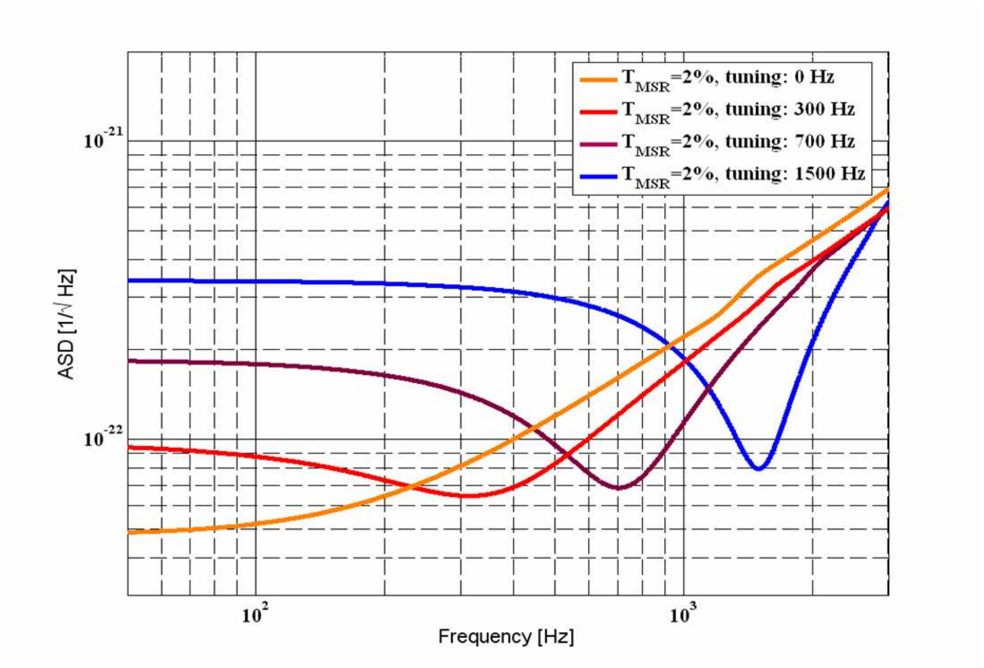

Figure 1.10.: Signal recycling and signal extraction sidebands. From signal recycling to signal extraction sideband the mirror SRM is tuned from zero to half FSR. At zero tuning the signal recycling cavity is resonant and traps the signal in the interforemeter; at half FSR the signal recycling cavity is anti-resonant and the signal sideband remain in the detector less time. This plot is taken from [Hil07].

1.6. A step toward the third generation GW detectors

(This is a Section mainly extracted from a paper already published [FCH^{+}09]).

The third-generation of gravitational wave observatories will focus not on the first detection of gravitational waves but rather recording astronomically useful data. This can be done by improving the sensitivity of the initial detectors and second generation respectively of by a factor of 100 and a factor of 10, in the whole frequency range. The design study for the Einstein Telescope (ET) is the first step to the third generation of GW detectors [ETh07, ETd]. Several studies are ongoing to improve the sensitivity to the aimed goal [EBN+09, VCH+05, CDKME09], although the field is very wide and many aspects must be taken into account. For example the reduction of seismic and gradient noises will be likely performed by locating the detectors underground [HT98, TW99]. This also means that the third generation will be not upgrading the current infrastructures, thus studies of new sites are also under way.

One more aspect to be considered is the topology of the new generation instruments. So far only Michelson topology has been considered for the first and second generations. A step toward the third generation GW detectors is presented in [FCH+09].

In particular a Michelson topology is investigated with a triangular geometry. Three coplanar Michelson are located at the same site to form an equilateral triangle. Here some features of this new detector are evaluated.

The first aspect of such a geometry comes from the fact that three Michelson's located in same place form multiple readout channels for the GW signal. This means that their linear combinations can be performed numerically to create a new GW channel to enhance the sensitivity of the detector. Two techniques like *time-delay interferometry* (TDI) [AET99, TA99, ETA00, AET03] and *displacement and frequency noise free interferometry* (DFI) (Chapter 2), although they have been developed for different purposes, can be considered for the triple Michelson geometry shown in Fig. 1.11. Both take advantages of the multiple readout channels to create one additional numerical channel. TDI uses this channel to remove the laser frequency noise, whereas DFI uses this channel to suppress all forms of displacement

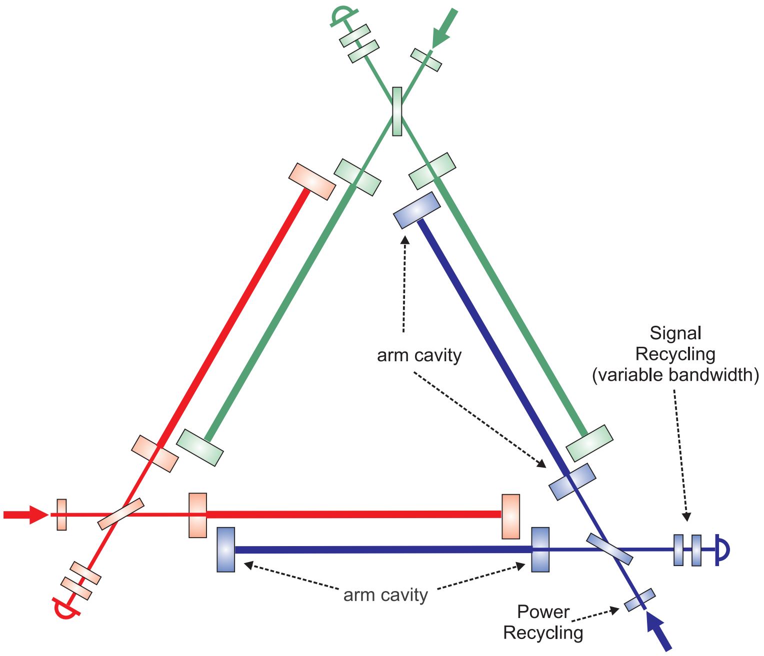

Figure 1.11.: Triple Michelson. Three coplanar Michelson are located in the same site to form an equilateral triangle. This configuration is provided with resonant arm cavities, power recycling and tunable signal recycling cavities. This plot is taken from [FCH+09].

noise. In other words the new channel can be interpreted as the output of 'virtual' interferometers. An example is given by the two 60° Michelson with uncorrelated noise described in [Cut98].

These two techniques (TDI, DFI) are currently used for the the construction of a particular channel, the so-called *null-streams*, which is a powerful technique of data analysis to identify noise signals that could be wrongly interpreted as GW signals. It is obtained from a linear combination of detector signals such that GW signals are suppressed while the noise signals are left with a certain amplitude.

In general, given three instruments (not all co-aligned) it is always possible to form one null-stream where the sensitivity of this stream depends on the relative instrument rotation [CLS+06, FCH+09]. From [JKS98] the response function h

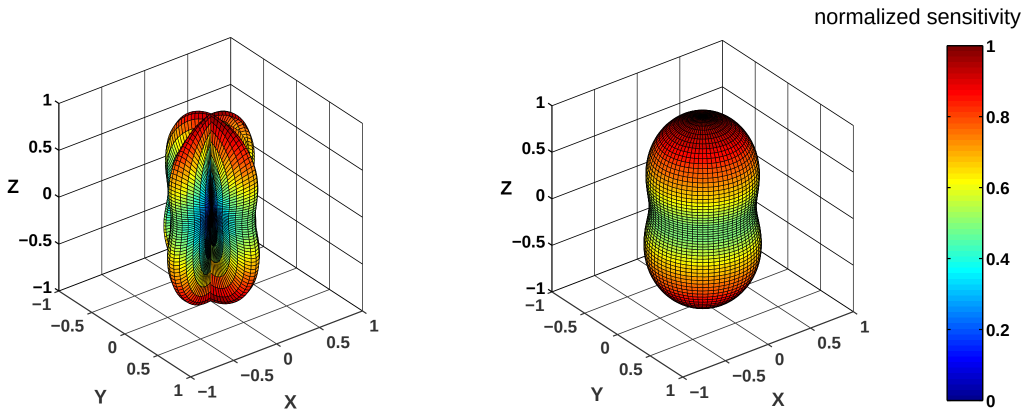

Figure 1.12.: The responses of detectors to a polarised GW traveling along the z-axis as a function of the detector orientation. The left-hand side shows the normalised sensitivity to one of a single Michelson, while the right-hand side shows the normalised sensitivity of the triple Michelson shown in Fig. 1.11. Data points represent the sensitivity of the detector which has its normal passing the respective data point and its origin. The magnitude of the sensitivity is expressed with color. This plot is taken from [FCH+09].

of a Michelson interferometer to gravitational waves can be written as a function dependent on the detector rotation γ around its normal, as follows:

$$\begin{aligned} h(\gamma) = \quad & \sin\zeta\left[\left(C_1 \sin 2\gamma + C_2 \cos 2\gamma\right) h_+ \right. \\ & \left. + \left(C_3 \sin 2\gamma + C_4 \cos 2\gamma\right) h_\times \right] \end{aligned} \tag{1.19}$$

with ζ the opening angle of the interferometer arms, h_x and h_+ represent the two GW polarisations and C_n functions of time. In particular for three Michelson interferometers oriented at 0°, 120° and 240°, it can be written:

$$-h_{0^\circ} = h_{240^\circ} + h_{120^\circ} \tag{1.20}$$

This shows two important features of the triangular geometry. One is that from two detector signals, the signal of a third can be obtained, the second is that is possible to create a null stream simply by adding all the outputs.

One more advantage of such geometry comes from better sky coverage. A single Michelson is more sensitive to one GW polarisation than to the other one, and one must consider that most GW will not be optimally polarised. The three Michelson geometry is sensitive to both polarisations at once, increasing the real sensitivity to most likely gravitational wave sources.

Thus the three Michelson geometry increases the sensitivity since it is sensitive to the second polarisation as well. Indeed using equation 1.20 the output signal can be synthesized for a Michelson at 45° rotated from equal interferometers rotated by 120° and 240°:

$$h_{45^\circ} = \frac{1}{\sqrt{3}}(h_{240^\circ} - h_{120^\circ}) \tag{1.21}$$

Fig. 1.12 shows the responses of detectors to a polarised GW traveling along the z-axis as a function of the detector orientation (antenna patterns). The sensitivity of a triple Michelson in a triangular geometry shows better performances than a single Michelson. The latter shows orientation at which it is insensitive to a certain GW polarisation, whereas the former does not present such limitations.

Chapter 2.

Displacement noise Free Interferometry for a Fabry-Perot cavity

As described in Chapter 1 current gravitational wave detectors are limited in sensitivity by several kinds of fundamental noises. Improvements in sensitivity is the goal to be reached in the next decade for the second and third generation of gravitational wave detectors. Sources of noise below 500 Hz belong to the displacement noises group which, in order to improve the sensitivity in this frequency band, is proving to be a great challenge for scientists. In this context a few years ago a new promising technique, later called *Displacement Noise-Free Interferometry* (DFI) was proposed by Y. Chen and S. Kawamura [KC04]. They used in this work a toy model composed of three aligned test masses analysed in the TT coordinate system, in which test masses when subjected to GW signals behave differently from motions due to displacement noises [Rak05]. Using an appropriate combination of light travel between the test masses, this difference allows the constructions of an observable which is free from any kind of displacement noise while the GW signal is still present. The implementation of this technique in GW detection, when laser interferometry is used, requires a further step for laser frequency noise, which affects all laser detectors. In the paper [CK06] Y. Chen and S. Kawamura, using the same approach of the previous paper, proposed a scheme in which both displacement and time noise were suppressed. Using N detectors, with connections between each of the pairs in d spatial dimensions, they showed that, when $N > d + 2$, it is possible to construct at least $N(N - d + 2)$ light travel combinations that are free from both displacement and time noises. They have proved that the GWs sensitivity was limited at low frequency by the frequency factor $\sim f^3$ for a two-dimensional interferometer. Later an optical design consisting of two pairs of two equal arm Mach-Zehnder placed in three spatial dimensions was proposed in [CPS$^+$06] where the GWs sensitivity was limited at low frequency by the frequency factor $\sim f^2$. A partial experimental proof of DFI is described in [SKW$^+$07] where a pair of bi-directional Mach-Zehnders were used to remove displacement from the folded mirror in the frequency band $[10^5 - 10^8]$ Hz. A complete experimental demonstration of DFI is provided in a recent work [KSN$^+$09] where the three-dimensional configuration proposed in [CPS$^+$06] has been implemented, as displacement noise from mirrors and beam-splitters were reduced in frequency-band $[10^5 - 10^8]$ Hz.

However, the large-baseline gravitational wave detectors do not work in this band. Recently a new DFI scheme has been proposed which works in a low frequency region. A detuned Fabry-Perot (FP) cavity configuration [TV08] in combination with two lasers is used to remove partially the displacement noise from both cavity mirrors. One laser is used for the input cavity mirror (IM) and one is used for the end cavity mirror (EM), known as Double Pumped Fabry-Perot cavity.

Such a configuration, although it does not include the frequency noise aspect of DFI, allows the isolation of the GW signal from displacement noise in a wide range of frequencies. Basically for each laser the reflected and transmitted output signals of the detuned FP-cavity carry different GW and displacement noise information, due to the existence of the prompt reflected light, and a proper combination of both signals results in the suppression of the displacement noise of the cavity's input mirror. Here the mechanism of noise cancelation is completely different from Chen-Kawamura's mechanism. The latter uses the distributed nature of GWs which result in different kinds of responses. In the long wave approximation $\lambda_{gw} \gg L$, where λ_{gw} is the GW wavelength and L is the cavity length, the leading order of the DFI signal for the detuned FP-cavity is $h(L/\lambda_{gw})^0$ which is much better than the $h(L/\lambda_{gw})^2$ that can be obtained from the Chen-Kawamura DFI scheme [CPS+06]. Nevertheless the detuned FP-cavity scheme loses the optical resonant gain from the cavity which is in the order of $c/\gamma L$, where γ is the cavity half bandwidth. Hence, the sensitivity of this scheme concerning GWs is strongly reduced compared to conventional interferometers and the noise performance of auxiliary optics becomes much more important.

This Chapter describes the idea behind the DFI topology of a detuned FP-cavity which has been proposed by S. P. Tarabrin , S. P. Vyatchanin. The description is largely based on the work referred in [TV08], and experimental demonstration will be provided in the following Chapters.

2.1. Simplified idea of DFI behind the detuned Fabry-Perot cavity

This Section explains the basic idea behind the DFI feature of a FP-cavity locked in a detuned state. The treatment is done neglecting time delay and considering GWs as classical forces applied on cavity mirrors in the inertial laboratory frame.

Fig. 2.1 shows the set-up of a *Double Pumped Fabry-Perot* cavity which is basically the toy-model proposed in [TV08], where the cavity is pumped from both sides using the two lasers L_1 and L_2. The cavity is assembled by the two partially reflective mirrors a and b. The laser L_1 pumps the cavity through the mirror a and the two detectors D_1 and D_2 measure the phases of the reflected and transmitted signals respectively. In order to simplify the analysis, the laser L_1 and the detector D_1 are rigidly mounted on the platform P_1 and the detector D_2 is rigidly mounted on platform P_2. On the other side the laser L_2 pumps the cavity through the mirror b and the two detectors D_3 and D_4 measure the phases of the reflected and transmitted signals respectively. The laser L_2 and the detector D_3 are rigidly mounted on platform P_2 and the detector D_4 is rigidly mounted on platform P_1. In other words relative movements of optical elements rigidly mounted on the same platforms are not taken in account but only the movements of platforms center of masses are considered.

Considering the cavity pumped through mirror a, if ξ_{gw} is the phase induced by GW displacement, ξ_a and ξ_b are the phases induced by the two mirrors a and b respectively, the measured transmitted signal $a^{\mathrm{t}}_{\mathrm{out}}$ can be written as follows:

$$a^{\mathrm{t}}_{\mathrm{out}} = \mathrm{q}_1(\xi_{\mathrm{gw}} + \xi_b - \xi_a), \tag{2.1}$$

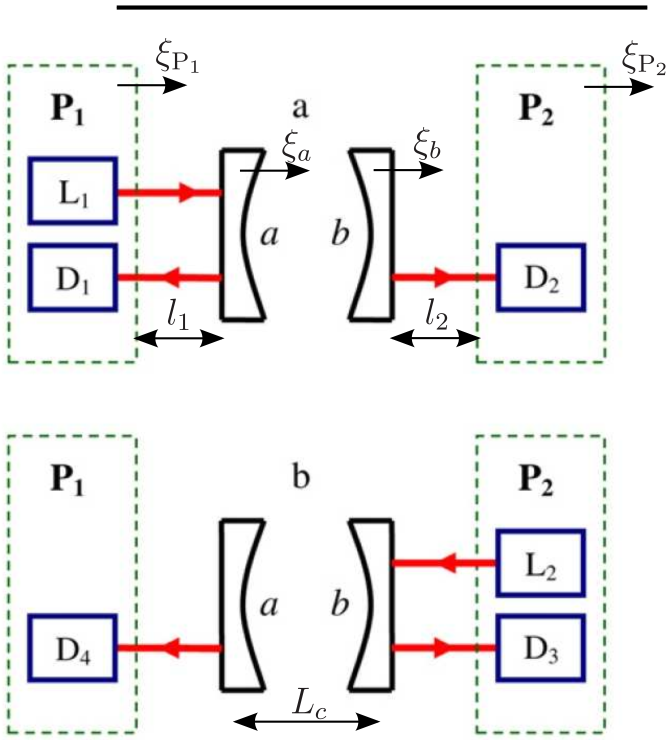

Figure 2.1.: Double pumped Fabry-Perot cavity. (a) The laser L_1 pumps the cavity through the mirror a and the two detectors D_1 and D_2 measure the reflected and transmitted signals respectively. (b) The laser L_2 pumps the cavity through the mirror b and the two detectors D_3 and D_4 measure the reflected and transmitted signals respectively. This plot is taken from [TV08].

where q_1 is the cavity gain factor. On the other hand, if ξ_{P_1} is the phase induced by platform P_1 displacement, the measured reflected signal a^{r}_{out} can be expressed as:

$$a^{\mathrm{r}}_{\mathrm{out}} = \mathrm{p}(\xi_a - \xi_{\mathrm{P}_1}) + \mathrm{q}_2(\xi_{\mathrm{gw}} + \xi_b - \xi_a), \tag{2.2}$$

where p is the gain factor of the so called prompt reflected light by the input cavity mirror and q_2 is the cavity gain factor. All the measurement are made with respect to platform P_1.

Similarly in the case of same lasers and same detunings when the cavity is pumped through the mirror b using the laser L_2 the phases of the reflected signal $b^{\mathrm{r}}_{\mathrm{out}}$ and the transmitted light $b^{\mathrm{t}}_{\mathrm{out}}$ can be written with respect to platform P_2 as follows:

$$\begin{aligned} b^{\mathrm{t}}_{\mathrm{out}} &= \mathrm{q}_1(\xi_{\mathrm{gw}} + \xi_b - \xi_a), && (2.3) \\ b^{\mathrm{r}}_{\mathrm{out}} &= \mathrm{p}(\xi_{\mathrm{P}_2} - \xi_b) + \mathrm{q}_2(\xi_{\mathrm{gw}} + \xi_b - \xi_a), && (2.4) \end{aligned}$$

ξ_{P_2} is the phase induced by platform P_2 displacement.

The following linear combination

$$s = a^{\mathrm{r}}_{\mathrm{out}} + \frac{\mathrm{p} - \mathrm{q}_2}{\mathrm{q}_1} a^{\mathrm{t}}_{\mathrm{out}} + b^{\mathrm{r}}_{\mathrm{out}} - \frac{\mathrm{q}_2}{\mathrm{q}_1} b^{\mathrm{t}}_{\mathrm{out}} = \mathrm{p}(\xi_{\mathrm{gw}} + \xi_{\mathrm{P}_2} - \xi_{\mathrm{P}_1}), \tag{2.5}$$

removes displacement noise from both cavity mirrors while the gravitational wave signal is retained, although displacement noise of both platforms is still present. It has to be noted that the noise suppression is not possible in two cases: The first is when the cavity is locked on a resonant state, which means $\mathrm{p} = 0$, the second case is when the two cavity mirrors are attached simultaneously to the platforms, which means $\xi_{\mathrm{a}} = \xi_{\mathrm{P}_1}$ and $\xi_{\mathrm{b}} = \xi_{\mathrm{P}_2}$.

2.2. Model of a single pumped Fabry Perot cavity

The proposed detuned FP-cavity configuration uses two lasers to remove the displacement noise from both cavity mirrors. The demonstration provided in [TV08] shows, as a first step, the use of one laser to remove the displacement noise from the IM. Afterwards the use of the second laser is used symmetrically to remove the displacement noise from the EM. This Section describes the fields of the cavity that will be used later to show the cancelation of the displacement noise from the IM which represents the theoretical view of the experimental demonstration provided in this thesis.

Fig. 2.2 shows the model of a single pumped FP-cavity. The cavity is assembled using the two movable and partially reflective mirrors a and b with transmission coefficients of $\mathrm{T} \ll 1$. The laser L pumps the cavity through the mirror a and simultaneously its beam is used as a reference beam in the two homodyne detectors HD_1 and HD_2 [TV08]. Auxiliary mirrors together with the laser and detectors are rigidly mounted on the platform P_1 and other auxiliary mirrors are rigidly mounted on platform P_2. This requirement is not restrictive as relative fluctuations of such elements would result in additional noises which are not essential to the description of the DFI detuned cavity model. The distances between platforms and cavity mirrors, l_1 and l_2, are supposed to be much smaller than the cavity length L_c.

Assuming the cavity is lying in the x-y plane, and is aligned to the GW x-axis, with respect to the local reference frame of the center of mass of platform P_1 the coordinates of the cavity mirrors and platforms can be written as:

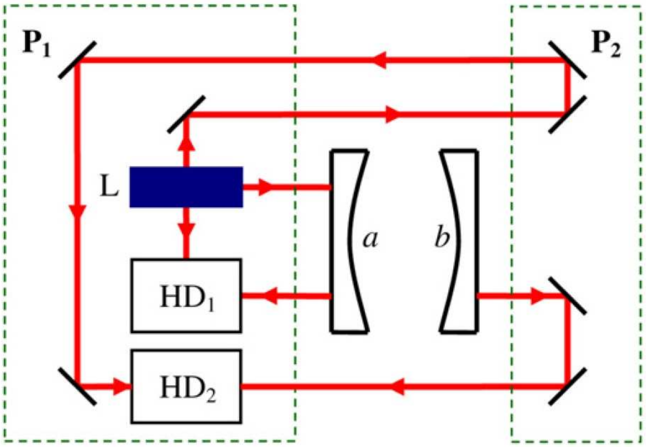

Figure 2.2.: Toy model. The cavity consists of the two movable and partially reflective mirrors a and b with transmission coefficients of $\mathrm{T} \ll 1$. The laser L pumps the cavity through the mirror a and simultaneously its beam is used as reference beam (LO) into the two homodyne detectors HD1 and HD2. The LO travels the same distance compared with the transmitted light in order to avoid additional phase shift induced by different optical path. The auxiliary mirrors, laser and detectors are rigidly mounted on the platform P_1, and other auxiliary mirrors are rigidly mounted on platform P_2. This plot is taken from [TV08].

$$
\begin{aligned}
x_{P_1}(t) &= 0, \\
x_a(t) &= l_1 + X_a(t) \approx X_a(t), \\
x_b(t) &= l_1 + L_c + X_b(t) \approx L_c + X_b(t), \\
x_{P_2}(t) &= l_1 + L_c + l_2 + X_{P_2} \approx L_c + X_{P_2}, \qquad (2.6)
\end{aligned}
$$

where X_a, X_b and X_{P_2} are the displacement noise with respect to platform P_1. Here the terms l_1 and l_2 are omitted since $l_{1,2} \ll L_c$ and do not change the results presented in this Chapter.

2.2.1. From TT-gauges to LL-gauges

It is important to remember that General Relativity is a gauge invariant theory, i.e. all measurable quantities in it do not depend on the choice of the gauge (reference frame) [FH05]. However the description of the GW interaction with interferometers in TT and LL gauges results in some differences [Rak05]. Basically in the TT-gauge the coordinates are fixed and the mutual distances between test masses change. Here the coordinates of the test masses do not change by interacting with GWs but they follow the test masses motion, which are meant as free falling objects. The interaction of GWs in this case results entirely in a light phase shift. In contrast in the LL-gauge a GW would move test masses from their positions, which results in changes in distance caused by their physical displacement. Here the coordinates of the test masses change when compared with the coordinate of the reference frame and their proper distance changes as well. In other simplified words in TT-gauge the coordinates moves with the test masses while in LL-gauge the coordinates do not follow the test masses. The interaction of GWs with interferometers in this case appears as tidal forces applied to the test masses (which means that that GWs are undistinguishable from any other non-gravitational forces), plus a small correction of the order of $(x/\lambda_{\rm gw})^2 h$ where x is the distance between two test masses, $\lambda_{\rm gw}$ is the GW wavelength and h is the GW amplitude [Tar07]. However, whatever gauge is used, the final measurable result is the same.

Since the test masses do not follow geodesics, the analysis of GW detectors is more appropriate in the local reference frame (LL gauge), which is a non inertial frame. The required inertial state of test masses imposed by the TT gauge description is not realistic. Test masses in ground based interferometers are subjected to several non-gravitational forces, consequently the proper reference frame is non-inertial [Tar07].

2.2.2. Quantised electromagnetic wave formalism

Taking into account the effect of the GWs and accelerating fields on the optical fields, the equivalence between TT gauges and LL-gauges is ensured [Rak05]. In this case, the electromagnetic wave propagating along the x-axis at frequency ω_0 and wave vector k_0, can be described by the electromagnetic field operator $A(x,t)$ as a sum of a strong field, which approximates the light wave of amplitude A_0 and a weak field $a(x,t)$ which describes the fluctuations of the light field [TV08]:

$$\begin{aligned} A(x,t) &= \sqrt{\frac{2\pi\hbar\omega_0}{S\mathrm{c}}}[A_0 + a(x,t)]e^{-\mathrm{i}(\omega_0 t \mp k_0 x)}, \qquad \text{with} \\ a(x,t) &= \int_{-\infty}^{+\infty} a(\omega_0+\Omega)e^{-\mathrm{i}\Omega(\mathrm{t}\mp\mathrm{x/c})}\frac{d\Omega}{2\pi}, \end{aligned} \tag{2.7}$$

where Ω is the GW frequency, S the cross section of the beam, $\hbar$ the Plank's constant and c the speed of light.

Assuming GWs and acceleration fields only couple to the strong light field, or equally said with the first order approximation in GW amplitude h and displacement ξ can be written [Tar07][TS08]:

$$A(x,t) = \sqrt{\frac{2\pi\hbar\omega_0}{S\mathrm{c}}}[A_0 + A_0 g_\pm(x,t) + A_0 w_\pm(x,t) + a(x,t)]e^{-\mathrm{i}(\omega_0 t \mp k_0 x)}, \tag{2.8}$$

where $g_\pm$ is the coupling term between GW and electro magnetic wave and $w_\pm$ is the redshift effect of the electro magnetic wave caused by the non inertial reference frame.

The $g_\pm$ term is defined as:

$$g_\pm(x,t) = \int_{-\infty}^{+\infty} g_\pm(x,\omega_o+\Omega)e^{-\mathrm{i}\Omega t}\frac{d\Omega}{2\pi}, \qquad \text{with} \tag{2.9}$$

$$g_\pm(x,\omega_o+\Omega) = h(\Omega)\left[\frac{1}{4}\omega_0\Omega\frac{x^2}{c^2} \mp \mathrm{i}\frac{1}{2}k_0x + \frac{1}{2}\frac{\omega_0}{\Omega}(e^{\pm\mathrm{i}\Omega x/c}-1)\right] \tag{2.10}$$

The $w_\pm$ term is defined as:

$$w_\pm(x,t) = \int_{-\infty}^{+\infty} w_\pm(x,\omega_0+\Omega)e^{-\mathrm{i}\Omega t}\frac{d\Omega}{2\pi}, \qquad \text{with} \tag{2.11}$$

$$w_\pm(x,\omega_o+\Omega) = -k_0\xi(\Omega)\left[\frac{\Omega}{c}x \pm \mathrm{i}(e^{\pm\mathrm{i}\Omega x/c}-1)\right]. \tag{2.12}$$

2.2.3. Input, output and circulating cavity waves

Fig. 2.3 shows the fields found in the F-P cavity as described in Section 2.2. $A_{in}(x,t)$ describes the wave pumped by the laser through the mirror a. The two outputs $A^r_{out}(x,t)$ and $A^t_{out}(x,t)$ are respectively the reflected and transmitted waves. The fields inside the cavity are divided into two: $A_+(x,t)$ represents the wave circulating along the positive direction of the x axis and $A_-(x,t)$ represents the wave circulating along the negative direction of the x axis. The cavity is pumped through the mirror b by the vacuum state wave $A_{vac}(x,t)$.

Using the the quantised formalism described in Section 2.2.2 the cavity fields can be described as follow:

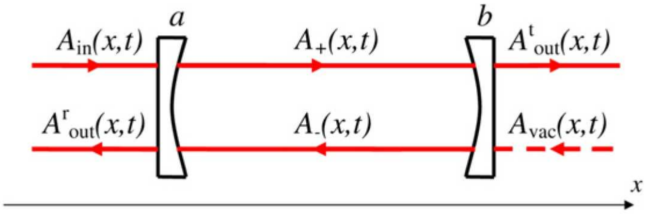

Figure 2.3.: Fields in a Fabry-Perot cavity. $A_{in}(x,t)$ describes the wave pumped by the laser through the mirror a. The enhanced light field inside the cavity, here represented by $A_+(x,t)$ and $A_-(x,t)$ according to the direction of the propagation, leaks outside the cavity. The leakage through the mirror b forms the transmitted output of the cavity $A^t_{out}(x,t)$. The leakage through the mirror a in addition to the prompt reflected light from the mirror a forms the reflected output of the cavity $A^r_{out}(x,t)$. The cavity is also pumped through the mirror b by the vacuum state wave $A_{vac}(x,t)$. This plot is taken from [TV08].

Input wave

$$\begin{aligned} A_{in}(x,t) &= \sqrt{\frac{2\pi\hbar\omega_0}{Sc}}A_{in0}[1+g_+(x,t)+w_+(x,t)]e^{-\mathrm{i}(\omega_1 t-k_1 x)}+ \\ &+ \sqrt{\frac{2\pi\hbar\omega_0}{Sc}}a_{in}(x,t)e^{-\mathrm{i}(\omega_1 t-k_1 x)}, \end{aligned} \tag{2.13}$$

where $a_{in}(x,t)$ describes the laser fluctuations, which in the current formalism is represented by a weak field.

Vacuum wave

$$A_{vac}(x,t) = \sqrt{\frac{2\pi\hbar\omega_0}{Sc}}a_{vac}(x,t)e^{-\mathrm{i}(\omega_1 t+k_1(x-L_c))}, \tag{2.14}$$

where $a_{vac}(x,t)$ describes the vacuum noise.

Circulating wave

$$\begin{aligned} A_{\pm}(x,t) &= \sqrt{\frac{2\pi\hbar\omega_0}{S\mathrm{c}}}A_{\pm 0}[1+g_{\pm}(x,t)+w_{\pm}(x,t)]e^{-\mathrm{i}(\omega_1 t\mp k_1 x)}+ \\ &+ \sqrt{\frac{2\pi\hbar\omega_0}{S\mathrm{c}}}a_{\pm}(x,t)e^{-\mathrm{i}(\omega_1 t\mp k_1 x)}, \end{aligned} \tag{2.15}$$

where $a_{\pm}(x,t)$ is the phase shift acquired by the light circulating in the cavity.

Reflected wave

$$\begin{aligned} A^r_{out}(x,t) &= \sqrt{\frac{2\pi\hbar\omega_0}{S\mathrm{c}}}A^r_{out0}[1+g_{-}(x,t)+w_{-}(x,t)]e^{-\mathrm{i}(\omega_1 t+k_1 x)}+ \\ &+ \sqrt{\frac{2\pi\hbar\omega_0}{S\mathrm{c}}}a^r_{out}(x,t)e^{-\mathrm{i}(\omega_1 t+k_1 x)}, \end{aligned} \tag{2.16}$$

where $a^r_{out}(x,t)$ describes the reflected signal of the cavity, whose quadratures are measured in the homodyne detector HD$_1$ [TV08]. The first addend describes the light propagation in the absence of the cavity which automatically vanishes at the origin point of the coordinates $x_{P_1}=0$ where $w=g=0$.

Transmitted wave

$$\begin{aligned} A^t_{out}(x,t) &= \sqrt{\frac{2\pi\hbar\omega_0}{S\mathrm{c}}} A^t_{out0}[1 + g_-(x,t) + w_-(x,t)]e^{-\mathrm{i}(\omega_1 t + k_1 x)} + \\ &+ \sqrt{\frac{2\pi\hbar\omega_0}{S\mathrm{c}}} a^t_{out}(x,t) e^{-\mathrm{i}[\omega_1 t - k_1(x - L_c)]}, \end{aligned} \tag{2.17}$$

where $a^t_{out}(x,t)$ describes the transmitted signal of the cavity whose quadratures are measured in the homodyne detector HD$_2$ [TV08]. As in the case of the reflected wave the first addend describes the light propagation in the absence of the cavity, but this time the addend does not vanish automatically. Indeed, the transmitted wave is detected at the origin of the coordinates after one round trip of light travel, as the light acquires on additional phase shift on the backward trip compared to the phase acquired by the local oscillator. This problem can be overcome by sending the reference light to platform P$_2$, as shown in Fig. 2.2. This will cause the reference light to travel the same distance as the transmitted wave, thus acquiring the same phase. The two equally acquired phases are completely subtracted in the homodyne detection.

It is worth noting that with such an optical setup, where the two homodyne detectors are located on the platform P$_1$, the same results could be obtained analysing the toy model into the general inertial frame.

The FP responses $a^t_{out}(x,t)$ and $a^t_{out}(x,t)$ are obtained as the solutions of the boundary conditions for a FP-cavity. This will now be further explained.

2.2.4. Boundary conditions and solutions

The continuity of the field on the mirrors surfaces is imposed as follow:

$$
\begin{aligned}
A_+(x_a,t) &= TA_{in}(x_a,t) - RA_-(x_a,t), && (2.18)\\
A^r_{out}(x_a,t) &= RA_{in}(x_a,t) + TA_-(x_a,t), && (2.19)\\
A_-(x_b,t) &= TA_{vac}(x_b,t) - RA_+(x_b,t), && (2.20)\\
A^t_{out}(x_b,t) &= RA_{vac}(x_b,t) + TA_+(x_b,t). && (2.21)
\end{aligned}
$$

This set of equations is solved in [TV08] where the first order of Ω/ω_1 solutions in the spectral domain are written as follow:

$$
\begin{aligned}
a^r_{out} = {}& \frac{R - Re^{2\mathrm{i}(\delta_1+\Omega)\tau}}{1 - R^2e^{2\mathrm{i}(\delta_1+\Omega)\tau}}a_{in} + \frac{T^2e^{\mathrm{i}(\delta_1+\Omega)\tau}}{1 - R^2e^{2\mathrm{i}(\delta_1+\Omega)\tau}}a_{vac} + \\
& - \frac{RT^2A_{in0}e^{2\mathrm{i}\delta_1\tau}}{1 - R^2e^{2\mathrm{i}\delta_1\tau}}\mathrm{i}\frac{2k_1(X_be^{\mathrm{i}\Omega\tau} - \sigma_1X_a) + \delta\Psi_{emw}}{1 - R^2e^{2\mathrm{i}(\delta_1+\Omega)\tau}}
\end{aligned} \tag{2.22}
$$

$$
\begin{aligned}
a^t_{out} = {}& \frac{T^2e^{\mathrm{i}(\delta_1+\Omega)\tau}}{1 - R^2e^{2\mathrm{i}(\delta_1+\Omega)\tau}}a_{in} + \frac{R - Re^{2\mathrm{i}(\delta_1+\Omega)\tau}}{1 - R^2e^{2\mathrm{i}(\delta_1+\Omega)\tau}}a_{vac} + \\
& + \frac{R^2T^2A_{in0}e^{3\mathrm{i}\delta_1\tau}}{1 - R^2e^{2\mathrm{i}\delta_1\tau}}\mathrm{i}\frac{2k_1(X_be^{\mathrm{i}\Omega\tau} - X_a) + \delta\Psi_{emw}}{1 - R^2e^{2\mathrm{i}(\delta_1+\Omega)\tau}}e^{\mathrm{i}\Omega\tau}
\end{aligned} \tag{2.23}
$$

where $\tau = L/c$ is the time delay, and δ_1 is the detuning of the cavity and Ψ_{emw} describes the coupling of the light field with the GW and accelerating field in the approximation $\Omega/\omega_1 \ll 1$ and has the following form:

$$\begin{aligned}\Psi_{emw} &= \Psi_{emw+gw} + \Psi_{emw+acc} \\ &= -k_1 L h(\Omega)\left(1 - \frac{\sin \Omega\tau}{\Omega\tau}\right) e^{\mathrm{i}\Omega\tau} - k_1 \xi_{\mathrm{P}_1}(\Omega)(1 - 2e^{\mathrm{i}\Omega\tau} + e^{2\mathrm{i}\Omega\tau}). \quad (2.24)\end{aligned}$$

The factor σ_1 describes the difference between a^r_{out} and a^t_{out} which is equal to 1 when the cavity is on the resonant state. It is defined as:

$$\sigma_1(\Omega) = e^{-2\mathrm{i}\Omega\tau}[1 - R^2 e^{2\mathrm{i}\delta_1\tau} - R^2 e^{2\mathrm{i}(\delta_1+\Omega)\tau} + R^2 e^{2\mathrm{i}(2\delta_1+\Omega)\tau}]/T^2 \quad (2.25)$$

Rewriting equations 2.22 and 2.23 in term of displacements ξ_a, ξ_b, ξ_{P_1}, the cavity responses are:

$$\begin{aligned}a^r_{out} &= \mathcal{R}_1 a_{in} + \mathcal{T}_1 a_{vac} \\ &- \frac{RT^2 A_{in0} e^{2\mathrm{i}\delta_1\tau}}{\mathcal{T}^2_{\delta_1}\mathcal{T}^2_{\delta_1+\Omega}} 2\mathrm{i}k_1[(\xi_b + \xi_{gw})e^{\mathrm{i}\Omega\tau} - \sigma_1\xi_a] \\ &- \frac{RT^2 A_{in0} e^{2\mathrm{i}\delta_1\tau}}{\mathcal{T}^2_{\delta_1}\mathcal{T}^2_{\delta_1+\Omega}} \mathrm{i}k_1\xi_{\mathrm{P}_1}(2\sigma_1 - 1 - e^{2\mathrm{i}\Omega\tau}), \quad (2.26)\end{aligned}$$

$$\begin{aligned}a^t_{out} &= \mathcal{T}_1 a_{in} + \mathcal{R}_1 a_{vac} \\ &+ \frac{R^2T^2 A_{in0} e^{3\mathrm{i}\delta_1\tau}}{\mathcal{T}^2_{\delta_1}\mathcal{T}^2_{\delta_1+\Omega}} 2\mathrm{i}k_1[(\xi_b + \xi_{gw})e^{2\mathrm{i}\Omega\tau} - \xi_a e^{\mathrm{i}\Omega\tau}] \\ &+ \frac{R^2T^2 A_{in0} e^{3\mathrm{i}\delta_1\tau}}{\mathcal{T}^2_{\delta_1}\mathcal{T}^2_{\delta_1+\Omega}} \mathrm{i}k_1\xi_{\mathrm{P}_1}(1 - e^{2\mathrm{i}\Omega\tau})e^{\mathrm{i}\Omega\tau}, \quad (2.27)\end{aligned}$$

where

$$\mathcal{T}^2_{\delta_1} = 1 - R^2 e^{2\mathrm{i}\delta_1\tau}, \qquad \mathcal{T}^2_{\delta_1+\Omega} = 1 - R^2 e^{2\mathrm{i}(\delta_1+\Omega)\tau}, \tag{2.28}$$

$$\mathcal{R}_1 = \frac{R - R e^{2\mathrm{i}(\delta_1+\Omega)\tau}}{1 - R^2 e^{2\mathrm{i}(\delta_1+\Omega)\tau}}, \qquad \mathcal{T}_1 = \frac{T^2 e^{\mathrm{i}(\delta_1+\Omega)\tau}}{1 - R^2 e^{2\mathrm{i}(\delta_1+\Omega)\tau}} \tag{2.29}$$

with $\mathcal{R}_1$ and $\mathcal{T}_1$ being the reflection and the transmission coefficient of a Fabry-Perot cavity. It can be noticed that the amplitude A_{in0} of input wave A_{in} is amplified inside the cavity by the factor $1/\mathcal{T}^2_{\delta_1}$. The GW frequency Ω affect the gain cavity factor by $\mathcal{T}^2_{\delta_1+\Omega}$. Since the cavity responses have been obtained when a single laser is used the same can be done when the cavity is pumped with a second laser from the other side and thus the mechanism of noise cancellation can be applied as described in the next Section.

2.3. Double pumped Fabry-Perot cavity

Fig. 2.4 shows a Fabry-Perot cavity pumped with two laser from both sides. The cavity is assembled using two partially reflective mirrors, a and b, spaced by a distance L. Laser L$_1$ pumps the cavity through the mirror a and laser L$_2$ pumps the cavity through the mirror b. Both lasers are rigidly mounted on platforms P$_1$ and P$_2$ respectively. A_{in} describes the input wave emitted by the laser L$_1$ and correspondingly the two outputs waves are described by A^r_{out} in reflection and by A^t_{out} in transmission. A_{vac} is the correspondent vacuum field pumping the cavity through the mirror b. B_{in} describes the input wave emitted by the laser L$_2$ and correspondingly the two outputs waves are described by B^r_{out} in reflection and by B^t_{out} in transmission. B_{vac} is the correspondent vacuum field pumping the cavity through the mirror a. The two light fields are orthogonally polarised. The detection scheme concerning the laser L_1 of such a model is shown in Fig. 2.2. Due to the symmetry of the model the detection scheme for laser L_2 can be equally thought of with two more homodyne detectors rigidly mounted together with laser L_2 on platform P_2.

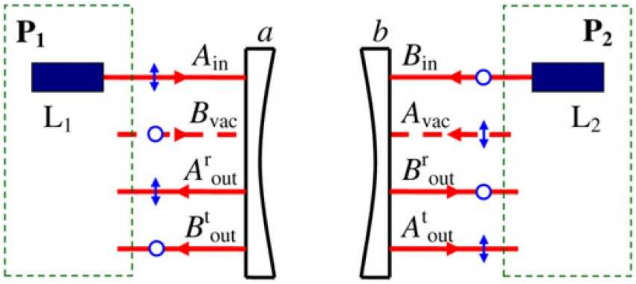

Figure 2.4.: Double pumped Fabry-Perot fields. The cavity is assembled from two partially reflective mirrors, a and b, spaced by a distance L. Two lasers are used to pump the cavity from both sides in order to obtain multiple channels to be used to construct the desired DFI channel. More specifically laser L_1 creates two channels given by the reflected A^r_{out} and transmitted A^t_{out} outputs of the cavity, whereas L_2 creates two channels given by the reflected B^r_{out} and transmitted B^t_{out} output of the cavity. A linear combination of these channels is used to construct a DFI channel which suppress the DN from the cavity mirrors. This plot is taken from [TV08].

The cavity response functions b^r_{out} and b^t_{out} when the cavity is pumped by the laser L_2 through the mirror b can be obtained from equations (2.26) and (2.27) replacing δ_1 with δ_2, ξ_a with ξ_b, ξ_b with $-\xi_a$, ξ_{P_1} with $-\xi_{P_2}$ and σ_1 with σ_2:

$$\begin{aligned} b^r_{out} &= \mathcal{R}_2 b_{in} + \mathcal{T}_2 b_{vac} + \\ &- \frac{RT^2 B_{in0} e^{2\mathrm{i}\delta_2\tau}}{\mathcal{T}^2_{\delta_2}\mathcal{T}^2_{\delta_2+\Omega}} 2\mathrm{i}k_2[(-\xi_a+\xi_{gw})e^{\mathrm{i}\Omega\tau}+\sigma_2\xi_b] + \\ &+ \frac{RT^2 B_{in0} e^{2\mathrm{i}\delta_2\tau}}{\mathcal{T}^2_{\delta_2}\mathcal{T}^2_{\delta_2+\Omega}} 2\mathrm{i}k_2\xi_{\mathrm{P}_2}(2\sigma_2-1-e^{2\mathrm{i}\Omega\tau}), \end{aligned} \tag{2.30}$$

$$\begin{aligned}
b^t_{out} &= \mathcal{T}_2 b_{in} + \mathcal{R}_2 b_{vac} + \\
&+ \frac{R^2T^2B_{in0}e^{3\mathrm{i}\delta_2\tau}}{\mathcal{T}^2_{\delta_2}\mathcal{T}^2_{\delta_2+\Omega}} 2\mathrm{i}k_2[(-\xi_a+\xi_{gw})e^{2\mathrm{i}\Omega\tau}+\xi_b e^{\mathrm{i}\Omega\tau}] + \\
&- \frac{R^2T^2B_{in0}e^{3\mathrm{i}\delta_2\tau}}{\mathcal{T}^2_{\delta_2}\mathcal{T}^2_{\delta_2+\Omega}} \mathrm{i}k_2\xi_{\mathrm{P}_2}(1-e^{2\mathrm{i}\Omega\tau})e^{\mathrm{i}\Omega\tau}, \qquad (2.31)
\end{aligned}$$

where (as similarly described in equations 2.28 and 2.29)

$$\mathcal{T}^2_{\delta_2} = 1 - R^2e^{2\mathrm{i}\delta_2\tau}, \qquad \mathcal{T}^2_{\delta_2+\Omega} = 1 - R^2e^{2\mathrm{i}(\delta_2+\Omega)\tau}, \qquad (2.32)$$

$$\mathcal{R}_2 = \frac{R - Re^{2\mathrm{i}(\delta_2+\Omega)\tau}}{1-R^2e^{2\mathrm{i}(\delta_2+\Omega)\tau}}, \qquad \mathcal{T}_2 = \frac{T^2e^{\mathrm{i}(\delta_2+\Omega)\tau}}{1-R^2e^{2\mathrm{i}(\delta_2+\Omega)\tau}} \qquad (2.33)$$

and

$$\sigma_2(\Omega) = e^{-2\mathrm{i}\Omega\tau}[1 - R^2e^{2\mathrm{i}\delta_2\tau} - R^2e^{2\mathrm{i}(\delta_2+\Omega)\tau} + R^2e^{2\mathrm{i}(2\delta_2+\Omega)\tau}]/T^2. \qquad (2.34)$$

The physical meaning of these coefficients can be deduced as for the laser L_1 case.

2.3.1. Displacement noise suppression procedure

As described previously the general DFI idea is to manipulate the multiple responses provided by the setup as an appropriate combination of them (the so called DFI response), resulting in the suppression of the displacement noise while the GW signal is still present.

Multiplying a^r_{out} by the factor $Re^{\mathrm{i}(\delta_1+\Omega)\tau}$ and multiplying a^t_{out} by σ_1, the combination

s_1 is defined as follow:

$$s_1 = Re^{\mathrm{i}(\delta_1+\Omega)\tau} a^r_{out} + \sigma_1 a^t_{out} \tag{2.35}$$

Multiplying b^r_{out} by the factor $Re^{\mathrm{i}(\delta_2+\Omega)\tau}$ and summing it to b^t_{out}, the combination s_2 is defined as follows:

$$s_2 = Re^{\mathrm{i}(\delta_2+\Omega)\tau} b^r_{out} + b^t_{out} \tag{2.36}$$

The DFI response is given by the following combination of s_1 and s_2 [TV08]:

$$s = s_1 + \frac{e^{\mathrm{i}\delta_1\tau}(1-e^{2\mathrm{i}\delta_1\tau})}{e^{\mathrm{i}\delta_2\tau}(1-e^{2\mathrm{i}\delta_2\tau})} s_2 e^{\mathrm{i}\Omega\tau}. \tag{2.37}$$

The meaning of the DFI response can be kept if the combination s is written in a different form. Replacing equations 2.26 and 2.27 in equation 2.35, equations 2.30 and 2.31 in equation 2.36 and assuming $A_{in0}/\mathcal{T}^2_{\delta_1} = B_{in0}/\mathcal{T}^2_{\delta_2}$, the combination s can be presented in the following explicit form:

$$\begin{aligned}
s &= a_{in}e^{-\mathrm{i}(\delta_1-\Omega)\tau} + \frac{1-e^{2\mathrm{i}\delta_1\tau}}{1-e^{2\mathrm{i}\delta_2\tau}}b_{in}e^{\mathrm{i}(\delta_1+2\Omega)\tau} \\
&+ \frac{R}{T^2}[e^{2\mathrm{i}\Omega\tau}(e^{2\mathrm{i}\delta_1\tau}-1)+\mathcal{T}_{\delta_1}^2e^{-2\mathrm{i}\delta_1\tau}]a_{vac} \\
&+ \frac{e^{-\mathrm{i}\delta_1\tau}(1-e^{2\mathrm{i}\delta_1\tau})}{e^{-\mathrm{i}\delta_2\tau}(1-e^{2\mathrm{i}\delta_2\tau})}Rb_{vac}e^{\mathrm{i}\Omega\tau} \\
&+ R^2e^{-\mathrm{i}(\delta_1+\Omega)\tau}(1-e^{2\mathrm{i}\delta_1\tau})\frac{A_{in0}}{\mathcal{T}_{\delta_1}^2} \\
&\times \mathrm{i}k_0[-\xi_{\mathrm{P}_1}+2(\xi_{\mathrm{P}_2}+\xi_{\mathrm{gw}})e^{\mathrm{i}\Omega\tau}-\xi_{\mathrm{P}_1}e^{2\mathrm{i}\Omega\tau}] \qquad (2.38)
\end{aligned}$$

The s combination shows that the DFI response is free from displacement noise from the cavity mirrors ξ_a and ξ_b while it still contains the term ξ_{gw} which is phase accumulated by the light due to the GW interaction.

It the particular case of equal detuning ($\delta_1 = \delta_2$), in the long-wave approximation where $\Omega L/c \ll 1$, assuming $\mathcal{A} = A_{in0=B_{in0}}$, s can be rewritten as follows:

$$\begin{aligned}
s &\approx a_{in}+b_{in}+a_{vac}+b_{vac} \\
&- \frac{\mathrm{i}\delta_1}{\gamma-\mathrm{i}\delta_1}\mathcal{A}2\mathrm{i}k_0\left(\frac{1}{2}Lh+\xi_{\mathrm{P}_2}-\xi_{\mathrm{P}_1}\right) \qquad (2.39)
\end{aligned}$$

It is interesting to note that equation 2.39, which can be associated with equation 2.5, shows that the double pumping F-P cavity shows a response with no cavity gain, and its sensitivity is limited by the displacement noise of the platforms.

In conclusion it has been demonstrated theoretically the DFI feature of a FP-cavity when the cavity itself is pumped from both sides with two lasers (or equivalently with two orthogonal polarised light fields) using the transmitted and the reflected responses as channels to be combined. It was shown that a proper combination of these channels allows the DN suppression from both cavity mirrors while the GW is still present. This is the basis for the realisation of the real experiment described in the next Chapters.

Chapter 3.

Construction of a DFI detuned cavity

3.1. From two lasers to one laser

The DFI scheme described in Chapter 2 shows that a detuned FP-cavity configuration [TV08] in combination with two lasers can be used to remove the displacement noise from both cavity mirrors. In such a double pumped Fabry-Perot cavity one laser is used for the input cavity mirror (IM) and one is used for the end cavity mirror (EM) (Double Pumped Fabry-Perot cavity). This configuration requires two homodyne detectors for each laser. From the experimental point of view the use of two lasers can be avoided by using auxiliary optics to have the laser pumping each side of the cavity with a different polarisation of light. The aim of this work is to demonstrate the feasibility of a DFI scheme for a detuned FP-cavity showing suppression of displacement noise at low frequencies, by showing the displacement noise cancelation only on the input cavity mirror.

Combining the responses a^t_{out} and a^r_{out} described in equations 2.1 and 2.2 a DFI channel can be created which is free from displacement noise of the input cavity mirror while the GW signal is still present:

$$s = a^{\mathrm{r}}_{\mathrm{out}} + \frac{\mathrm{p} - \mathrm{q}_2}{\mathrm{q}_1} a^{\mathrm{t}}_{\mathrm{out}} = \mathrm{p}(\xi_{\mathrm{gw}} + \xi_{\mathrm{P}_2} - \xi_{\mathrm{P}_1} + \xi_{\mathrm{b}}), \tag{3.1}$$

where $\mathrm{q_i}$ are the cavity gain factors and ξ_{i} are phase induced by the "i^{th}" optical element.

Alternatively the potential for DFI can be shown using the detuned cavity responses multiplying a^r_{out} by the factor $Re^{\mathrm{i}(\delta_1+\Omega)\tau}$ and multiplying a^t_{out} by σ_1, the DFI combination s_1 is defined as follow:

$$s_1 = Re^{\mathrm{i}(\delta_1+\Omega)\tau} a^r_{out} + \sigma_1 a^t_{out} \tag{3.2}$$

where σ_1 is defined in equation 2.25, δ_1 is the cavity detuning and Ω the GW frequency. In explicit form, using equations 2.26 and 2.27, s_1 can be rewritten as (see Section 2.3.1):

$$\begin{aligned} s_1 &= a_{in} e^{-\mathrm{i}(\delta_1-\Omega)\tau} \\ &+ \frac{R}{T^2}[e^{2\mathrm{i}\Omega\tau}(e^{2\mathrm{i}\delta_1\tau} - 1) + \mathcal{T}^2_{\delta_1} e^{-2\mathrm{i}\delta_1\tau}] a_{vac} \\ &+ R^2 e^{\mathrm{i}\delta_1\tau}(1 - e^{2\mathrm{i}\delta_1\tau}) \frac{A_{in0}}{\mathcal{T}^2_{\delta_1}} 2\mathrm{i}k_0(\xi_{\mathrm{b}} + \xi_{\mathrm{gw}}) e^{2\mathrm{i}\Omega\tau} \\ &- R^2 e^{\mathrm{i}\delta_1\tau}(1 - e^{2\mathrm{i}\delta_1\tau}) \frac{A_{in0}}{\mathcal{T}^2_{\delta_1}} \mathrm{i}k_0 \xi_{\mathrm{P}_1}(1 + e^{2\mathrm{i}\delta_1\tau}) e^{\mathrm{i}\Omega\tau} \end{aligned} \tag{3.3}$$

In this thesis DFI is addressed only insofar as it deals with the suppression of displacement noise of the input cavity mirror.

3.1.1. Laser

(This Section follows the description presented in [Che07]). The light source used for the DFI experiment is a solid state Nd:YAG laser which yields 1 W power with $\lambda_0 = 1064\,\mathrm{nm}$ wavelength. It is a *Mephisto* manufactured by *Innolight*. A schematic of this laser is shown in Fig. 3.1. Two diodes, electrically driven by a stable low noise injection system with a maximum current of 3 A, provide the radiation to the monolithic nonplanar crystal Nd:YAG. The two light pumps are combined onto a polarising beam splitter (PBS) and opportunely focused to match the crystal's fundamental mode. The crystal forms a ring cavity that the pump light field circulates in, transforming it to a wavelength of $\lambda_0 = 1064\,\mathrm{nm}$ wavelength.

The injection current is internally restricted to its clamping value by a limiting circuit to protect the diode laser. In Fig. 3.2 the power radiated by the laser is shown responding to the electric current applied to the crystal.

A photodetector is used to sense a fraction of the generated laser light and variations in the emitted radiation are analysed. The fluctuations of the emitted light are mainly due to the relaxation oscillation effect that is a typical noise source of solid state lasers [HRH$^+$97]. The sensed signal, after been opportunely filtered and amplified, is fed back to the diode pump sources to reduce such intensity fluctuations. This is an optional servo loop called *Noise Eater*.

The laser system is also provided with a temperature stabilising control of the laser diode junction to prevent wavelength variations of the emitted light. Furthermore the wavelength of the Nd:YAG laser also depends on the crystal temperature which

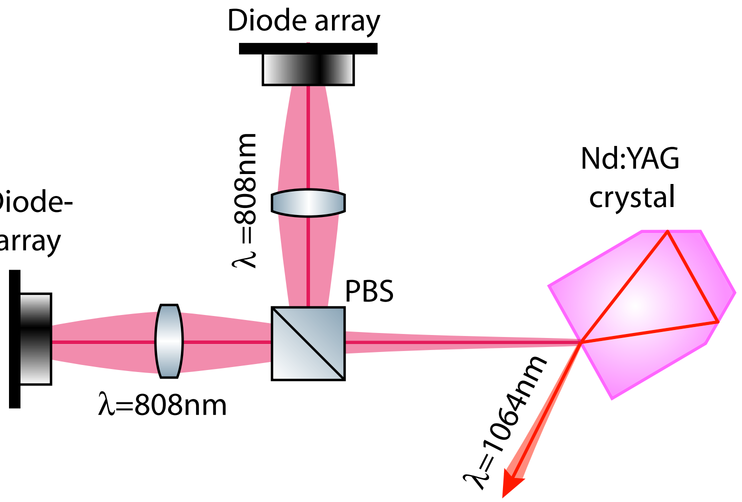

Figure 3.1.: Laser scheme. Two diodes, electrically driven by a stable low noise injection system with a maximum current of 3 A, provide the radiation to the monolithic nonplanar crystal Nd:YAG. Two light pumps are combined on a polarising beam splitter (PBS) and opportunely focused to match the fundamental mode of the crystal. This plot is taken from [Che07].

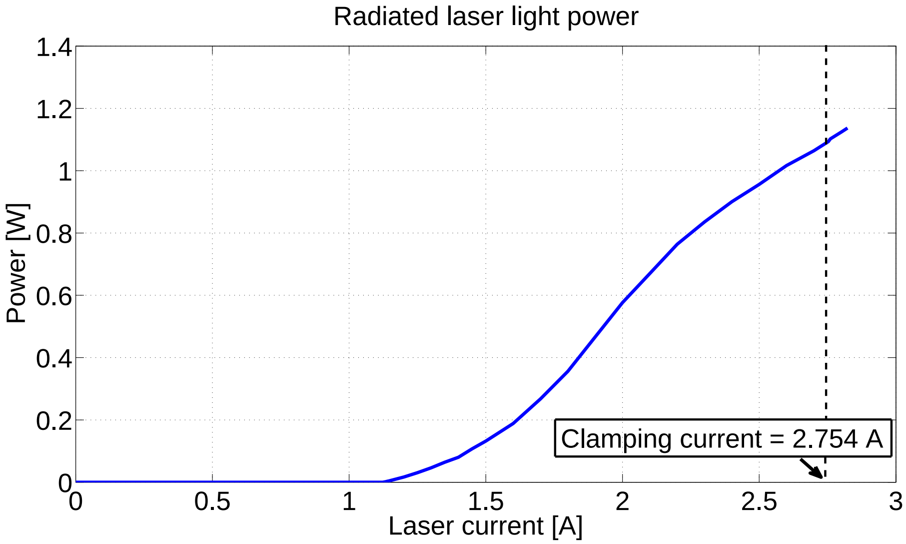

Figure 3.2.: Power radiated vs. injection current. The electrical protection system clamps the current at 2.750 A. The crystal temperature is fixed at 32.8 °C.

Output power	1 W
Beam quality	$M^2 < 1.1$
Thermal tuning coefficient [GHz/K]	-3
Thermal tuning range [GHz]	30
Thermal response bandwidth [Hz]	1
PZT tuning coefficient [MHz/V]	>1
PZT tuning range [MHz]	± 100
PZT response bandwidth [kHz]	100
Emission spectrum	single-frequency
Coherence length [km]	>1
Relative Intensity Noise, RIN [dB/Hz]	<-100
Noise eater option, RIN [dB/Hz]	<-150
Output polarised beam	$\mathrm{I_s/I_p} \cong 5/1$

Table 3.1.: General specification of the ND:YAG laser

is also stabilised using a temperature actuator. Thermal expansion of the crystal corresponds to a change in length of it and therefore its internal ring cavity, causing the wavelength of the emitted light to vary. Such temperature actuator reaches a thermal tuning range of 3 GHz/K with a response bandwidth of 1 Hz. An additional actuator, a piezoelectric transducer (PZT), is attached to the laser crystal to change its length, for fast tuning of laser frequency. The frequency tuning range obtainable is 2 MHz/V with a response bandwidth of 100 kHz.

The relevant specifications of the laser are collected in the Tab. 3.1.

The output beam of the ND:YAG laser is elliptically polarised with an intensity ratio of $I_s/I_p \cong 5/1$, where I_s and I_p are respectively the intensities of the s and p components of the light. A combination of a quarter-waveplate and half-waveplate is able to transform the light to any of the linear polarisation states. The quarter-waveplate eliminates the residual elliptical polarisation while the half-waveplate rotates a linearly polarised light from one state to another.

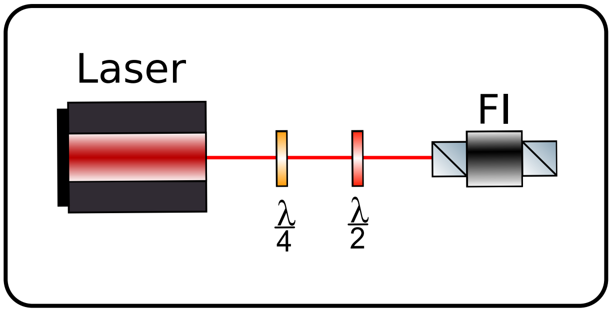

Figure 3.3.: Laser source setup. The generated laser light is elliptically polarised with an intensity ratio of $I_s/I_p \cong 5/1$. A quarter-waveplate transforms the elliptical polarised light in linear polarised light. The half-waveplate is used to rotate the linear polarised state into the other linear polarised state to maximise the light reaching the experiment. The Faraday isolator (FI) itself is used to protect the laser from the light reflected back from the experiment.

In order to maintain good laser function a Faraday isolator is used afterwards to suppress the light reflected from the experiment back to the laser, avoiding any disturbances of the generated light. The linear polarisation state of the light is optimised for transmission through the Faraday isolator, maximizing the light power that reaches the experiment.

The Fig. 3.3 shows the light source setup used in the DFI experiment.

3.1.2. Laser beam source profile characterisation

The current of the laser crystal is $I = 2.200\,\mathrm{A}$ and the crystal temperature is set to $T = 32.8\,^\circ\mathrm{C}$. The light source has been characterised by measuring its beam profile. Both the vertical and horizontal beam sections are measured along the laser beam path above the Faraday isolator with a CCD-sensor (*WinCamD*) and displayed by *Dataray* software. The data are then fitted to a mathematical model [Hei95]. Fig. 3.4 shows the measured results and both sections with fitted curves.

Vertical waist size	197.0 μm
Horizontal waist size	183.2 μm
Vertical waist position	-23.4 cm
Horizontal waist position	-24.3 cm

Table 3.2.: Laser beam profile features. The zero reference point is the front edge of the Fraday isolator.

The gaussian nature of the beam allows it to be completely determined once its beam waist size and its beam waist position are known. In the Tab. 3.2 the values calculated by the fitting function are given, taking as zero reference position the edge of the Faraday isolator farthest from the laser.

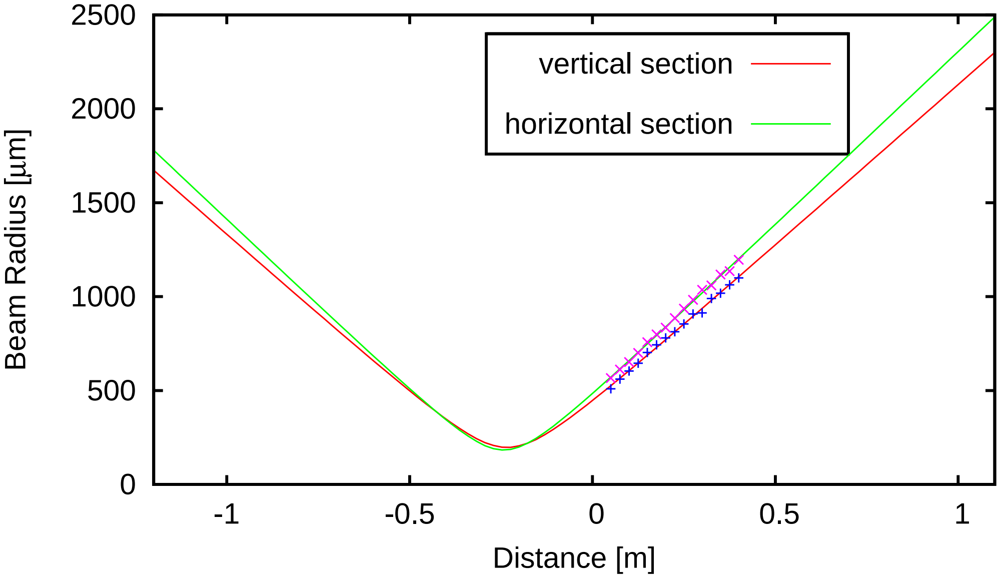

Figure 3.4.: Laser beam profile of the light source. The measurements of the beam profile have been made along the path in front of the Faraday isolator. The injection current of the laser diode is $I = 2.200\,\mathrm{A}$ and the laser crystal temperature is $T = 32.8\,^{\circ}\mathrm{C}$.

3.2. Feedback control system

Control theory is a research area based on mathematical and engineering techniques aimed at automatising and improving mechanical systems. Several types of control loops are described in literature as in [DFT91]. The basic concept is that of keeping one or more system output variables on a prefixed value, the so called *reference*. Dynamical behavior of systems imposes the output variable to be monitored over time. When the output variable of the system deviates from its reference a signal proportional to the deviation is generated, the *error signal*, and elaborated by the *controller* which manipulates the input variables of the system, acting on an *actuator* compensating the unwanted output variations. The physical variable to be controlled is detected by the *sensor*, which usually is a transducer, a device used to convert physical quantity to another.

In this experiment, the crucial physical variables requiring feedback control are the length of the cavity and the relative phases of the two beams in the homodyne detectors. In order to demonstrate the DFI method experimentally it is necessary to keep the cavity in a detuned state. This is achieved with a feedback control loop based on the Pound-Drever-Hall (PDH) technique. The advantage of this technique is the decoupling of the laser frequency from the laser intensity, resulting in a low noise control loop. Frequency drift of the laser and displacement of the mirrors can cause a deviation of the cavity from the required detuned working point. These effects can be corrected for by either tuning the laser frequency or the cavity length, thereby keeping the cavity at the correct working point. In the former case, with the PDH method, one can measure the laser frequency with a FP-cavity and feedback this measurement to the laser to correct and suppress drift and fluctuations in frequency. In this thesis the latter case is adopted, where the laser frequency is measured with the same cavity and the feedback signal is applied to a PZT actuator attached to the cavity input mirror. The cavity length is changed in this way to compensate for laser frequency and mirror position fluctuations. Similarly the two homodyne detectors required by the DFI detuned cavity setup can be locked with a modulation-demodulation technique to maintain the homodynes detectors desired working point given by a fixed phase difference between the LO and the input beam (see Section 3.4.1).

The stabilisation of both the optical systems, cavity and homodyne detectors, can be described as in Fig. 3.5 where the sensor is assembled by the photodectors (PD), the mixer (Mx) and the oscillator (Osc). The light is modulated into the optical system with use of an electro-optic-modulator. The optical output of the system is measured and converted into a voltage signal in the photodetector and sent to the mixer to be demodulated with the use of a 12 MHz oscillator. The resulting measured output is compared with the reference signal and opportunely filtered by the servo amplifier to provide a voltage signal which is applied to the actuator. The actuator is, both for the cavity and for the homodynes, a transducer (PZT) which transforms the input voltage into mechanical movements. In the cavity case this can be either the PZT attached to the laser or the PZT attached onto the input cavity mirror whereas for the homodyne detector only the PZT attached onto one of the optical elements along one of its beam path.

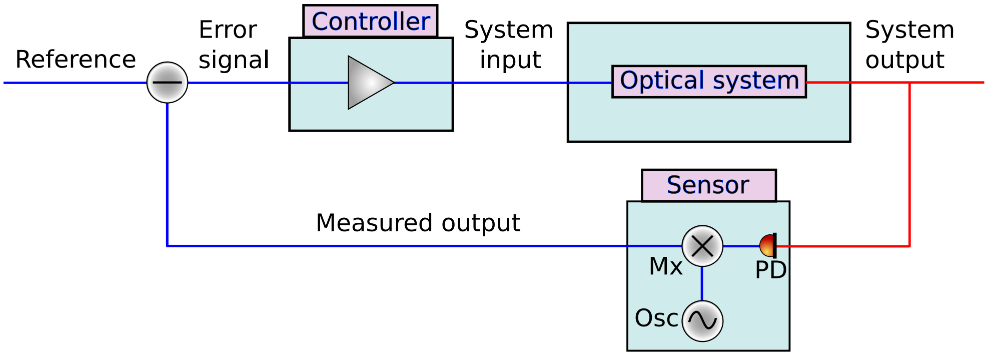

Figure 3.5.: Schematic feedback control loop. The DFI experiment requires three different optical systems to be stabilised: The Fabry-Perot cavity and two homodyne detectors. All these systems can be controlled with a modulation-demodulation method. The cavity has to be locked on a 12 MHz state, while the homodyne detectors can be locked respecting all their quadratures.

3.2.1. Optical modulation of the light

Electro-Optic-Modulators (EOMs), *New Focus* products, are used in the DFI detuned FP-cavity to provide a phase modulation of the light field in a wide range of frequencies. EOM consist basically of an anisotropic crystal, *Magnesium Oxide* doped with *Lithium Niobate* ($\mathrm{MgO : LiNbO_3}$), and two electrodes used to apply an external electric field along the crystal axis orthogonal to the direction of light propagation. Modulation is produced by aligning the polarisation of the input light with the crystal axis along which the electric field is applied [New01], whereas any misalignment can create unwanted light amplitude modulation. In particular the optimal case is when when the light is s-polarised, also called vertically polarised light.

EOMs are based on the *Pockels cell* effect which is the linear dependence of the

	model 4001	model 4004
Wavelength	1.0 - 1.6 μm	1.0 - 1.6 μm
Type	Resonant PM	Broadband PM
Operating Frequency	0.01 - 250 MHz	DC-100 MHz
Modulation Depth	$>$ 0.2 rad/V	15 mrad/V
Max V_π	16 V	210 V
Max. Optical Power	1W/mm^2	1W/mm^2
Aperture	2 mm	2 mm

Table 3.3.: Characteristics of *New Focus* electro-modulators [New01].

crystal's refractive index on the applied electric field. It can be expressed as follow:

$$\Delta n \propto n_e^3 E \tag{3.4}$$

where Δn is the change in the index of refraction, n_e is the unperturbed index of refraction and E is the applied electric field.

Two different EOMs are used in this work for two different purposes. The 4001 model is a narrow-band phase modulator and it is used to provide the cavity stabilisation signal using the Pound-Drever-Hall scheme, while the 4004 model is a wide-band phase modulator and it is used to produce a simulated GW-signal. Characteristics of both EOMs are collected in the table 3.3.

3.2.2. Mixer

The Pound-Drever-Hall technique used to stabilise the cavity requires the use of a mixer to extract the error signal. The mixer used (see Appendix D.4) is an electronic device with three ports: Two inputs and one output. The input which contains the signal is RF *(Received Frequency)*. The other input which is generated electronically by an oscillator at fixed frequency, Ω, is LO *(Local Oscillator)*. The mixing of the two inputs produces an output with frequency between Ω and the signal frequency, ω, which is called IF *(Intermediate Frequency)*. Actually the output, which can be understood as the product of the two inputs, contains multiple components at the sum and difference of the two inputs frequencies and their harmonics. An ideal mixer produces only the sum and the difference components, which can be selected with a proper filter: the selection of the components gives respectively an *up conversion* and *down conversion*.

3.2.3. Servo amplifier

The error signal extracted from the mixer is processed by the servo amplifier (see Appendix D.3) to produce a feedback signal. Appropriately designed analogue filters allow the system to maintain a physical variable on a prefixed value, known as the operating point. Deviations from the operating point are compensated for by the servo which produces signals proportional to the deviations but with opposite phase. The output of the servo is used to close the loop on an actuator system. In particular the servo used in the DFI setup has a proportional gain and three different integrators. The roll-off frequencies of such filters are 100 Hz, 1 kHz, 10 kHz. The Fig. 3.6 shows the measured servo transfer function from its error-in input to feedback signal output when the integrators are all switched off.

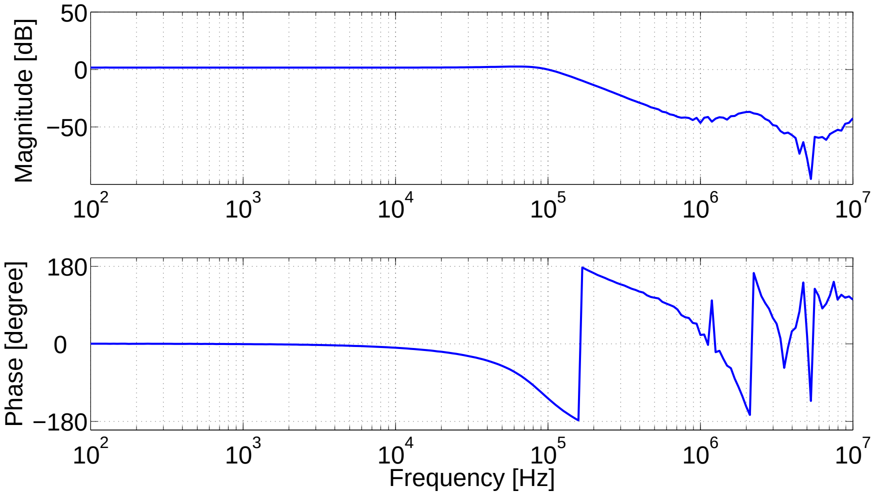

Figure 3.6.: The measured servo transfer function. The plot shows a 100 kHz low pass filter effect.

3.2.4. Local oscillator

The local oscillator provided to both the EOM and the mixer is a device which produce a 12 MHz frequency waveform. The schematic can be found in the Appendix D.5. Fig. 3.7 shows a partial simulated transfer function of the oscillator.

3.2.5. Photodetectors

The optical reflected and transmitted signals from the cavity are converted by a *BPX* ”Manufacturer” photodiode into electrical current signals. The photodiode is arranged in a self-made electrical circuit to convert the current signal in voltage signal using a *transimpedance stage*. The voltage signal is amplified by two amplification stages, one providing the AC output and the other the DC. The DC stage feature is to amplify the voltage signal keeping low frequency components; The AC stage amplifies the voltage signal and high-pass filters the signal. In this work

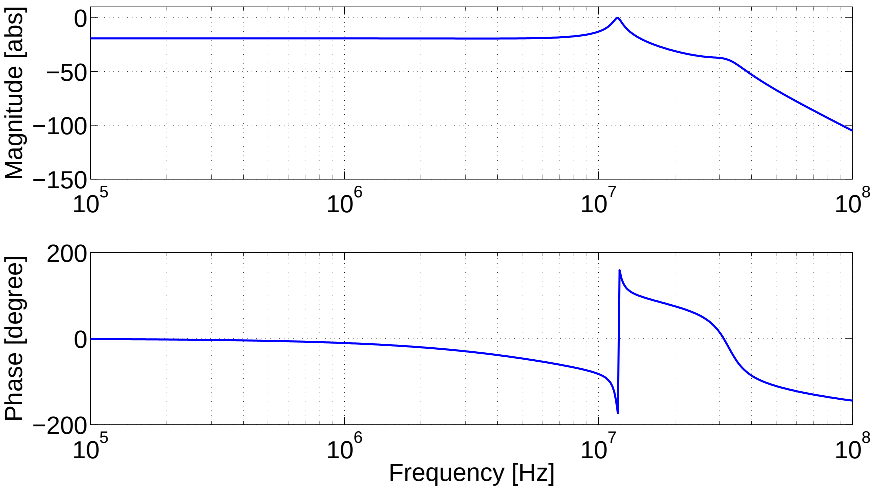

Figure 3.7.: The simulated transfer function of the 12 MHz oscillator from pin 8 to the output as shown in Fig. D.12. The plot shows the 12 MHz bandwidth filter effect.

the photodiode and the electrical circuit together are called the *photodetector*. The schematic of the photodetectors used in the current DFI experiment is in Appendix D.1. In particular the *locking photodetector* detects the light reflected back from the cavity forming part of the sensor used in the cavity control loop. The homodyne photodetectors are used for the homodyne detection at the DFI outputs. The balanced homodyne detection requires that the homodyne photodetectors are as equal as possible. Figures 3.8 and 3.9 show the transfer functions of the locking and the homodyne photodetectors from the optical input to both the DC and AC outputs respectively.

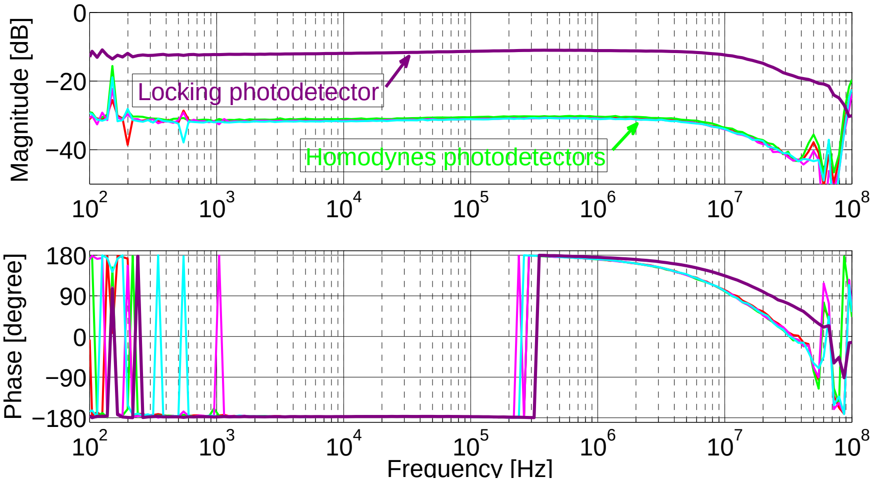

Figure 3.8.: The measured DC transfer functions of photodetectors. These are measured transfer functions from the optical input to the DC output channels of the photodetectors. All the measured transfer functions show a flat response at low frequencies.

3.3. The DFI core

The core instrument of the work presented here is a FP-cavity. This system is used to provide multiple readout channels, given by the reflected and transmitted light from the cavity. In this Section the design and the method used to keep it at a desired working point are described.

3.3.1. Fabry-Perot cavity design

An EOM (see Section 3.2.1) is situated in the centre of the cavity to provide a simulated gravitational wave signal. This places a constraint on the cavity design, due to the 2 mm aperture and the maximum optical power limitation. These constraints lead to the design which requires an input beam waist size between 250 and 500 μm and a Rayleigh range at least equal to the length of the crystal as required by the

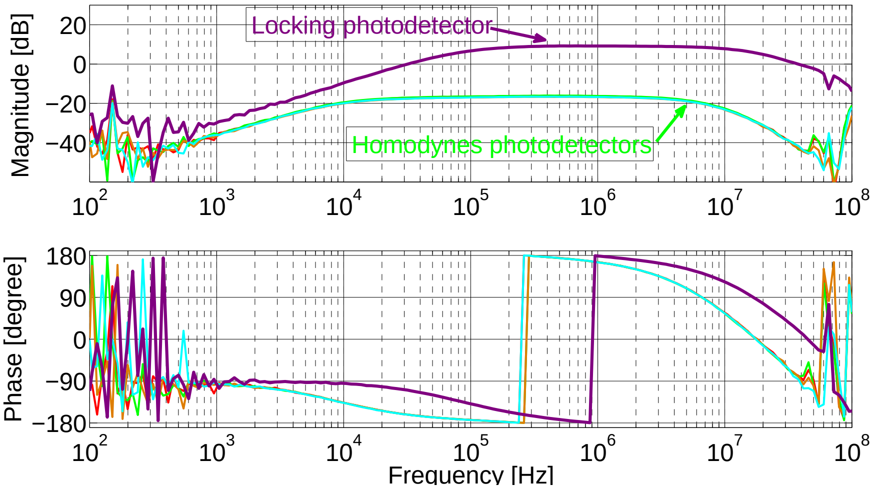

Figure 3.9.: The transfer functions of the AC photodetectors. Those are transfer functions measured from the optical input to the AC output. All the measured transfer functions show a high-pass filter effect: The locking photodetector has a roll-off frequency at 160 kHz while the homodyne photodetectors have a roll off frequency at 15 kHz.

manufacturer ([New01]). The cavity length and the radius of curvature of both cavity mirrors determine the shape of the TEM_{00} eigenmode [Yar89]. Defining the following quantities as

$$\mathrm{z}_1 = (\mathrm{Rc2} \cdot \mathrm{L} - \mathrm{L}^2)/(\mathrm{Rc1} - \mathrm{Rc2} + 2\mathrm{L}) \qquad \text{and} \qquad \mathrm{z}_2 = \mathrm{L} + \mathrm{z}_1 \tag{3.5}$$

where Rc1 and Rc2 are the radii of curvatures of the input and output cavity mirrors respectively and L is the cavity length. It is possible to express the Rayleigh range,

$\mathrm{z_r}$, as a function of radius of curvature, Rc1 as follows:

$$\mathrm{z_r} = \sqrt{(\mathrm{Rc1} - \mathrm{z_1})\mathrm{z_1}}, \tag{3.6}$$

and the beam waist radius, ω_0, the beam radius ω_1 at the cavity input mirror and the beam radius ω_2 at the end cavity mirror as

$$\omega_0 = \sqrt{\mathrm{z_r}\lambda/\pi}, \qquad \omega_1 = \omega_0\sqrt{1 + (\mathrm{z_1}/\mathrm{z_r})^2}, \qquad \omega_2 = \omega_0\sqrt{1 + (\mathrm{z_2}/\mathrm{z_r})^2}. \tag{3.7}$$

The detuned state of the cavity required by the DFI configuration [TV08] imposes a careful choice of the amplitude reflectivities $\mathrm{r_1}, \mathrm{r_2}$ of the two cavity mirrors which affect the cavity Finesse as shown in the reference [Hei99]:

$$\mathrm{Finesse} = \frac{\mathrm{FSR}}{\mathrm{FWHM}} = \frac{\pi}{2\arcsin\left(\frac{1-\mathrm{r_1r_2}}{2\sqrt{\mathrm{r_1r_2}}}\right)} \approx \frac{\pi\sqrt{\mathrm{r_1r_2}}}{1-\mathrm{r_1r_2}} \approx \frac{\pi}{1-\mathrm{r_1r_2}} \tag{3.8}$$

where FSR=c/2L is called *Free Spectral Range* and FWHM is the *Full Width* at *Half Maximum.* The parameters of the designed FP-cavity are collected in Table 3.4.

Fig. 3.10 shows the optical setup of the cavity used in the DFI experiment. The light source is turned into an s-polarised state by half-waveplate. A telescope assembled by the lenses f1 and f2 is used to obtain a beam waist of 400 μm located in the

Cavity length	L	30 cm
Free spectral range	FSR	500 MHz
Radius of curvature of the input mirror	Rc1	1 m
Radius of curvature of the output mirror	Rc2	1 m
Beam waist	ω_0	347 μm
Beam size onto input cavity mirror	ω_1	377 μm
Beam size onto output cavity mirror	ω_2	377 μm
Rayleigh range	z_r	35.7 cm
Power reflectivity of the input cavity mirror	r_1^2	0.985
Power reflectivity of the output cavity mirror	r_2^2	0.985
Finesse	F	208
Full Width at Half Maximum	FWHM	2.4 MHz

Table 3.4.: The designed optical parameters of the cavity.

center of EOM1, which is used in turn to produce the 12 MHz sidebands. The half-waveplate and the polarising beam splitter (PBS1) are used to set the power input to the cavity cavity beam at 1.5 mW. A telescope consisting of lenses f3 and f4, is used to match the TEM_{00} mode of a beam into the cavity, resulting in a beam waist of 360 μm located in the middle of the cavity.

3.3.2. Cavity stabilisation

The laser light field $E_{inc}(\omega)$, after being passed through EOM1 (see Fig. 3.10), can be expressed as a sum of three terms, a carrier at frequency ω and two sidebands at $\omega \pm \Omega$, with Ω being the modulation frequency and m the modulation depth:

$$\begin{aligned} E_{inc} &= E_0 e^{i(\omega t + m \sin \Omega t)} \\ &\approx E_0[J_0(m)e^{i\omega t} + J_1(m)e^{i(\omega+\Omega)t} - J_1(m)e^{i(\omega-\Omega)t}] \end{aligned} \tag{3.9}$$

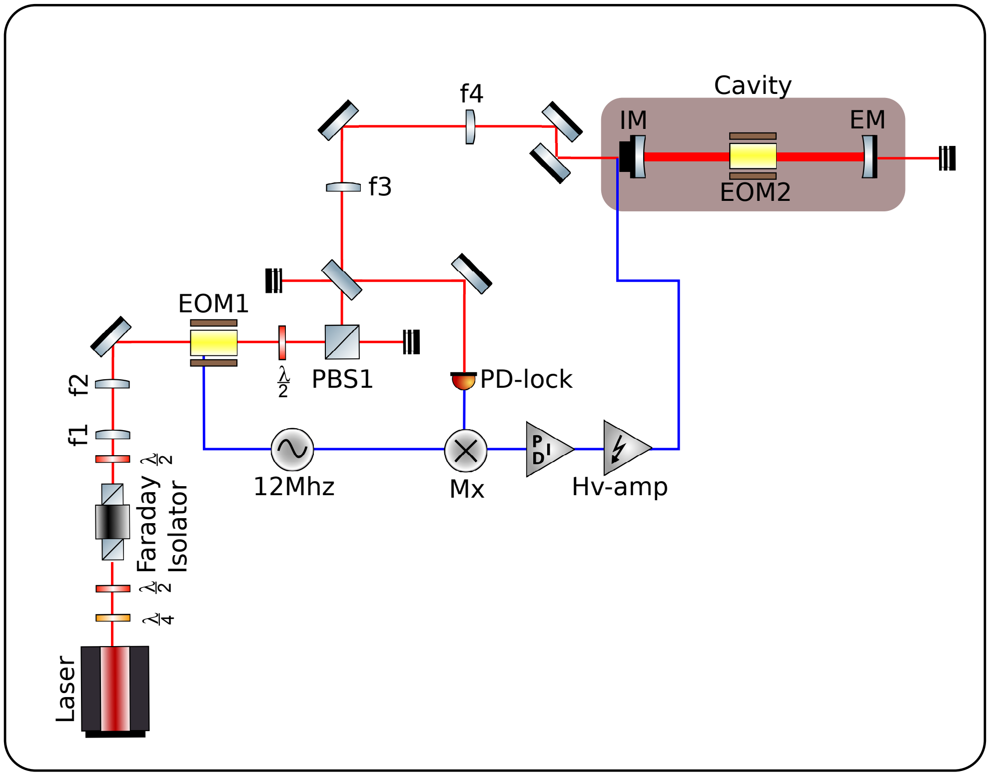

Figure 3.10.: The FP-cavity setup. The cavity is pumped through the mirror IM with s-polarised light modulated at 12 MHz by the electro-optic-modulator EOM1. The pump light is set at 1.5 mW by a half-waveplate and the polarising beam splitter PBS1. Two telescopes assembled by the lenses f1, f2 and f3, f4 provide a beam waist of 400 μm in the center of EOM1 and a beam waist of 360 μm in the middle of the cavity, respectively. The reflected light from the cavity is sensed by the locking photodetector, PD-lock, and demodulated in the mixer Mx. The output of Mx, after being appropriately filtered by the servo PID and amplified by HV-ampl, is applied to the PZT attached onto IM.

where J_i are the Bessel functions of the first kind. The power in the carrier can be expressed as $P_c = J_0^2(m)P_0$ and the power in the first order sidebands as $P_s = J_1^2(m)P_0$ where $P_0 = |E_0|^2$. When the modulation index m is much smaller than one, all the power is shared between the carrier and sidebands $P_0 \approx P_c + 2P_s$.

The locking photodetector PD-lock measures the power of the reflected beam from the cavity:

$$\begin{aligned} P_{ref} = |E_{ref}|^2 &= P_c|F(\omega)|^2 + P_s\{|F(\omega+\Omega)|^2 + |F(\omega-\Omega)|^2\} \\ &+ 2\sqrt{P_c P_s}\{\Re[F(\omega)F^*(\omega+\Omega) - F^*(\omega)F(\omega-\Omega)]\cos\Omega t\} \\ &+ 2\sqrt{P_c P_s}\{\Im[F(\omega)F^*(\omega+\Omega) - F^*(\omega)F(\omega-\Omega)]\sin\Omega t\} \\ &+ (2\Omega\,\text{terms}), \end{aligned} \tag{3.10}$$

where $F(\omega) = E_{ref}/E_{inc}$ is the reflection coefficient. The use of a mixer and a low-pass filter isolates only the Ω term generating the PDH error-signal used to control the cavity. Depending on the modulation frequency Ω the measured PDH error-signal can be either the $\cos\Omega t$ or $\sin\Omega t$ terms. When Ω is high ($\Omega \gg FSR/F$) only the $\sin\Omega t$ term survives and when Ω is low ($\Omega \ll FSR/F$) only the $\cos\Omega t$ term survives [Bla01]. The PDH signal for the DFI detuned cavity relies on the former case, since the modulation is applied at 12 MHz.

Fig. 3.11 shows the PDH error-signal (yellow curve) and the reflected power detected on PD-lock (blue curve) while a ramp (pink curve) is applied on the PZT attached onto the input cavity mirror IM, scanning the cavity length.

Recalling that the mixer output can be modelled as the product of its inputs, in

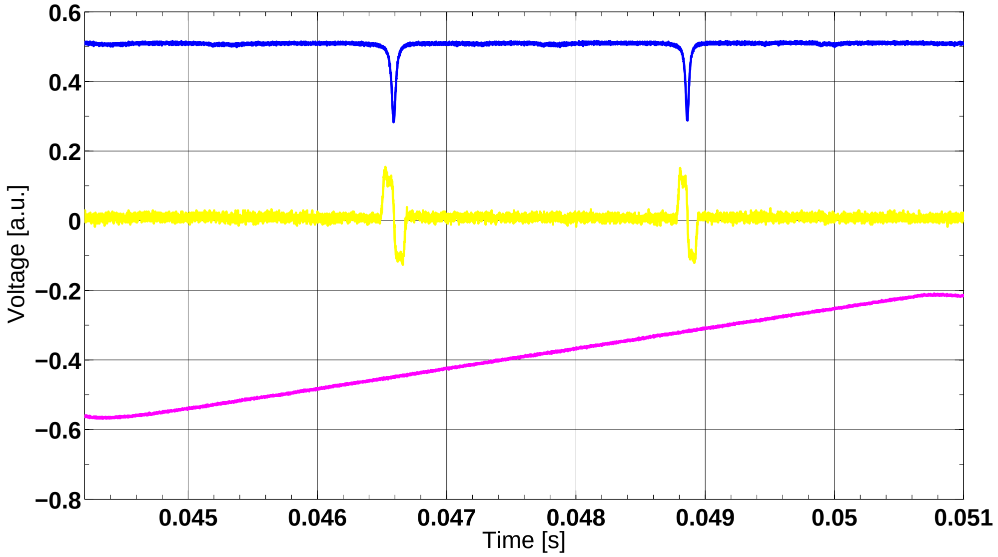

Figure 3.11.: Cavity signals. The PDH error-signal (yellow curve) and the reflected power detected on PD-lock (blue curve) while a ramp (pink curve) is applied on the PZT attached to the input cavity mirror IM, scanning the cavity length.

the general case, for a modulation signal at Ω this can be written:

$$\sin(\Omega t)\sin(\Omega^* t) = \frac{1}{2}\{\cos[(\Omega - \Omega^*)t] - \cos[(\Omega + \Omega^*)t]\}, \tag{3.11}$$

where Ω^* is the demodulation frequency. In particular if $\Omega = \Omega^*$ we can write:

$$\sin(\Omega t)\sin(\Omega t) = \frac{1}{2}\{1 - \cos(2\Omega t)\}. \tag{3.12}$$

When the 2Ω term is filtered with a low-pass filter only a DC term survives. In practice the low-pass filter and a phase delay are implemented in the mixer box, the latter used to match the modulation and demodulation phases. (Appendix D.4).

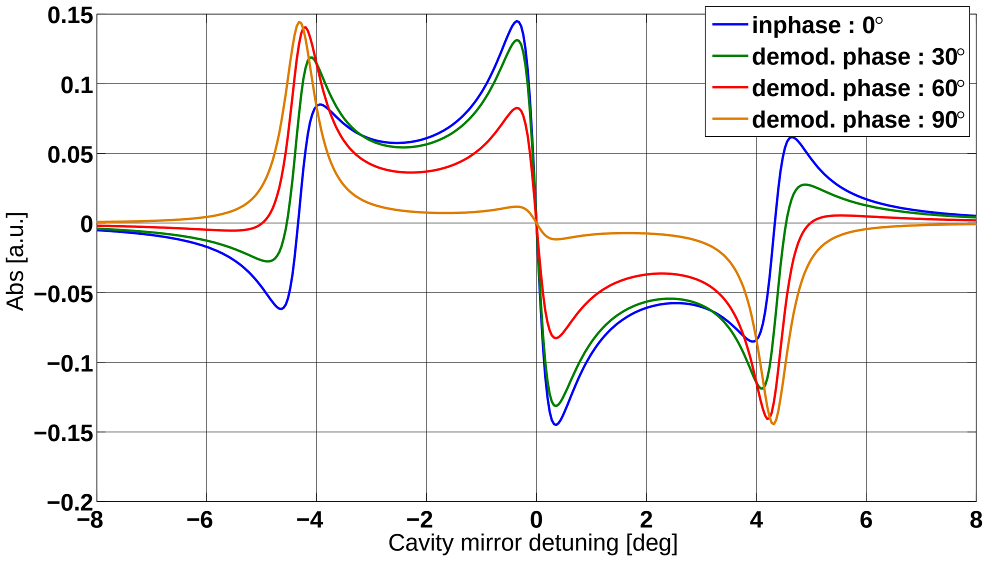

Figure 3.12.: Simulated PDH error-signals vs. cavity mirror detuning at different demodulation frequency values: Phase matched modulation and demodulation frequency (blue curve), demodulation frequency at 30° (green curve), 60° (red curve) and 90° (orange curve).

Fig. 3.12 shows simulated PDH error-signals vs. cavity mirror detuning at different demodulation frequency values: Phase matched modulation and demodulation frequency (blue curve), demodulation frequency at 30° (green curve), 60° (red curve) and 90° (orange curve).

Fig. 3.13 shows the experimental time trace of the PDH error signal obtained by scanning the cavity length with a ramp applied onto the PZT of the input cavity mirror at different phase delay settings.

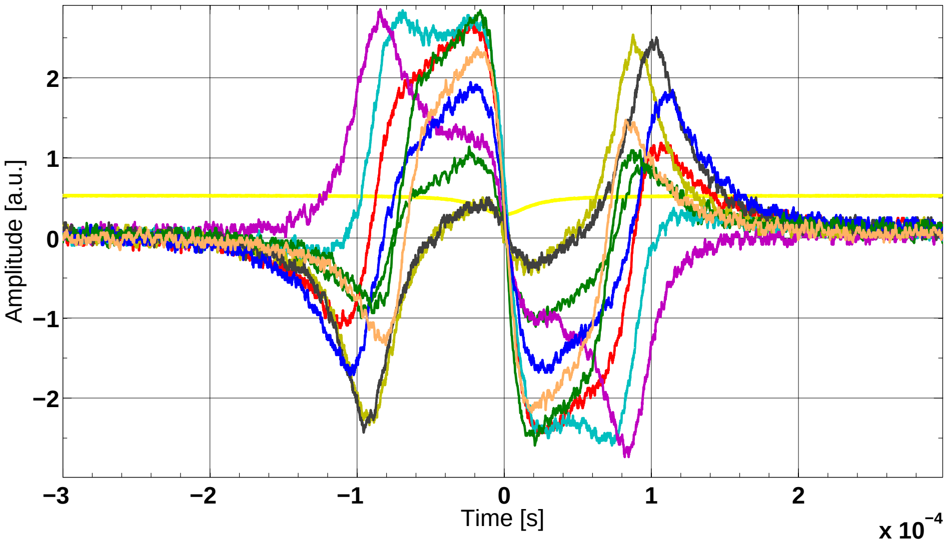

Figure 3.13.: Experimental time trace of the PDH error signal obtained by scanning the cavity length with a ramp applied onto the PZT of the input cavity mirror at different phase delay settings.

3.4. DFI detection

Since a direct detection scheme could measure only amplitude fluctuations and would be not able to distinguish between the quadratures of the field, the detection scheme proposed in [TV08] is provided by the two homodyne detectors. These are able to detect the phase modulated signal coming from the input cavity mirror (used to simulate the displacement noise signal) and from the EOM (used to simulate the GW signal). This can be obtained with the use of a reference beam, the local oscillator (LO), which gives a phase reference to detect both the amplitude and the phase modulation.

The Fig. 3.14 shows the setup of the DFI detection. The light originating from the laser is split into two beams, one to pump the FP-cavity and one to provide the two local oscillators (LO) for the homodyne detectors HD1 and HD2. The reflected and transmitted signals from the cavity individually interfere onto the homodyne beam splitters, BSH1 and BSH2, with the LO beam and sensed with the two homodyne detectors HD1 and HD2 respectively. The two half waveplates and two polarising beam splitters PBS2 and PBS3 are used to set the LO power in both the homodyne detectors at 20 mW. The transmitted light from PBS3, which is p-polarised, is then rotated again by an half waveplate to let the light interferes on BSH2 in s-polarised state.

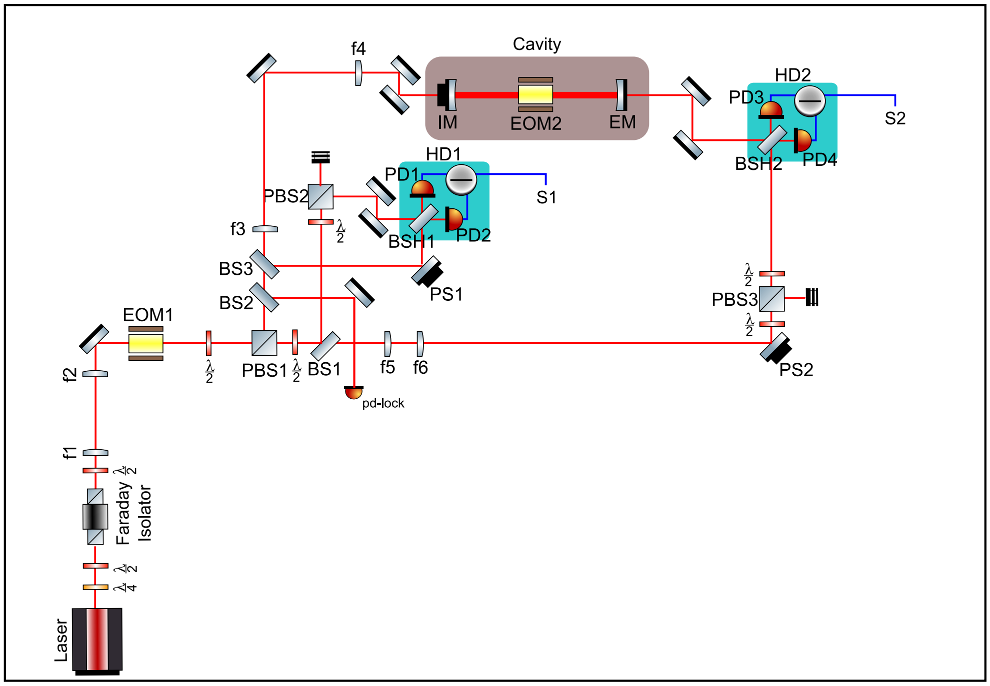

Figure 3.14.: DFI detection setup. The light originating from the laser is split into two beams, one to pump the FP-cavity and one to provide the two local oscillators (LO) for the homodyne detectors HD1 and HD2. The reflected and transmitted light are sensed with homodyne detectors HD1 and HD2 respectively. The two half-waveplates and two polarising beam splitters PBS2 and PBS3 are used to set the LO power in both the homodyne detectors at 20 mW.

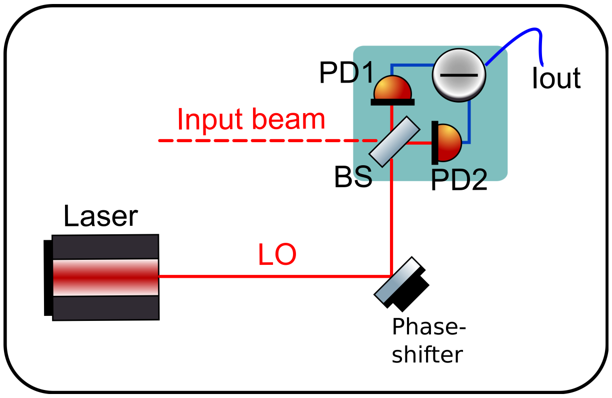

Figure 3.15.: The homodyne detector. It consists of a beam splitter and two photodetectors PD1 and PD2. The LO provided by the laser interferes onto the beam splitter with an input beam of which the contribution of the modulation one wants to evaluate. The interference signal is detected by PD1 and PD2. The subtraction of their photocurrents gives the output of the homodyne detector.

3.4.1. Homodyne detector

Fig. 3.15 shows the generic setup of a homodyne detector. In general homodyne detection can be done with the use of a beam splitter BS and two photodetectors PD1 and PD2. The LO provided by the laser interferes on the beam splitter with an input beam which contributes to the modulation one wants to evaluate. The interference signal is detected by PD1 and PD2. The subtraction of their photocurrents gives the output of the homodyne detector. In order to use the LO as a phase reference beam the input beam to the cavity has to be phase locked to LO. In the case of the DFI detuned FP-cavity the input beam for HD1 is the reflected light and the input beam in HD2 is the transmitted light.

A homodyne detector feature

Let's represent each of the two homodyne beams as the sum of two contribution: a sum of a strong field which approximates the light wave of amplitude $E_{in,lo}$ and a weak field $\delta E_{in,lo}(t)$ which describe the fluctuations of the the light field [Bac98]:

$$\begin{aligned} E_{in}(t) &= E_{in} + \delta E_{in}(t) \\ E_{lo}(t) &= (E_{lo} + \delta E_{lo}(t))e^{i\phi_{lo}} \end{aligned} \tag{3.13}$$

where $e^{i\phi_{lo}}$ represents the relative phase difference between the two beams. It is controlled with a PZT attached onto a mirror located in one of that path to change the length of one of the paths.

Fields on the two photodetectors PD1 and PD2 are described with following convention:

$$E_{\mathrm{PD1}} = \sqrt{\frac{1}{2}}\left(iE_{lo}(t) + E_{in}(t)\right) \tag{3.14}$$

$$E_{\mathrm{PD2}} = \sqrt{\frac{1}{2}}\left(E_{lo}(t) + iE_{in}(t)\right) \tag{3.15}$$

In the case where the LO intensity is much higher than input beam intensity, $E_{lo}^2 \gg E_{in}^2$, the intensity I_{PD1} onto the photodetector PD1 can be calculated as:

$$\begin{aligned} I_{\mathrm{PD1}} &= |E_{\mathrm{PD1}}|^2 = \frac{1}{2}\left(|E_{lo}(t)|^2 + iE_{lo}(t)E_{in}^*(t) - iE_{in}(t)E_{lo}^*(t) + |E_{in}(t)|^2\right) \\ &\approx \frac{1}{2}\left(|E_{lo}(t)|^2 + 2E_{lo}\delta E_{lo} + 2E_{lo}\delta E_{in}(t)\sin\phi_{lo}\right) \end{aligned} \tag{3.16}$$

In the same way the intensity I_{PD2} on the photodetector PD2 can be calculated as:

$$I_{\mathrm{PD2}} = |E_{\mathrm{PD2}}|^2 \approx \frac{1}{2}\left(|E_{lo}(t)|^2 + 2E_{lo}\delta E_{lo} - 2E_{lo}\delta E_{in}(t)\sin\phi_{lo}\right) \tag{3.17}$$

Now the homodyne detector output can be defined, represented by the intensity difference between the two photodetectors:

$$I_{12} = I_{\mathrm{PD1}} - I_{\mathrm{PD2}} \approx 2E_{lo}\delta E_{in}(t)\sin\phi_{lo}. \tag{3.18}$$

This equation shows an important feature of the homodyne detector: that the output scales with the amplitude of the local oscillator while the noise on the local oscillator itself is completely suppressed.

Decomposing the weak field into its quadratures as $\delta E_{in}(t) = E1_{in}(t) + iE2_{in}(t)$, the photocurrent fluctuations at the output of the homodyne detector can be expressed as:

$$\Delta I_{12} \approx 4E_{lo}^2\left(\Delta E1_{in}(t)\sin^2\phi_{lo} + \Delta E2_{in}(t)\cos^2\phi_{lo}\right) \tag{3.19}$$

where it can be noted that the variance of the output is a combination of the variance of the fluctuations in the two quadratures. The LO phase determines in which quadrature the fluctuations can be measured.

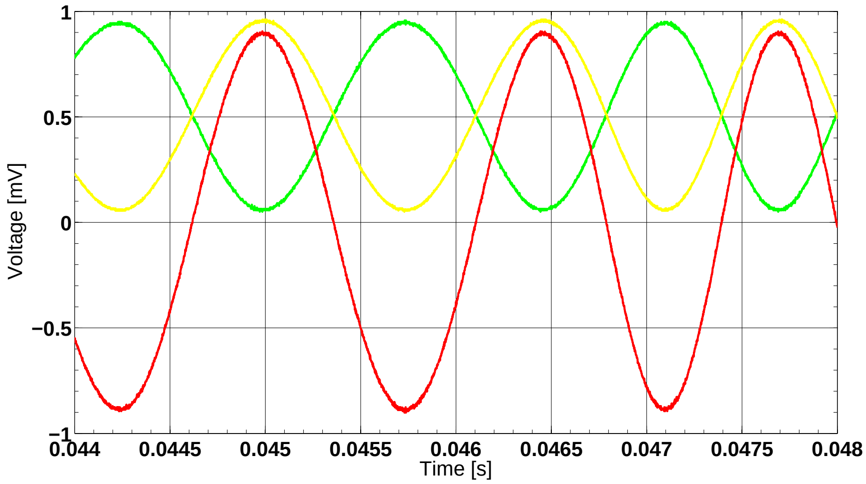

Figure 3.16.: The homodyne detectors HD1 outputs. Both the photodetectors PD1 (yellow curve) and PD2 (green curve) show an interference pattern with a visibility $(V_{max} - V_{min}/V_{max} + V_{min})$ of $\approx$ 93%. The error-signal is the difference photocurrent detected by the two photodetectors PD1 and PD2 represented in the red curve.

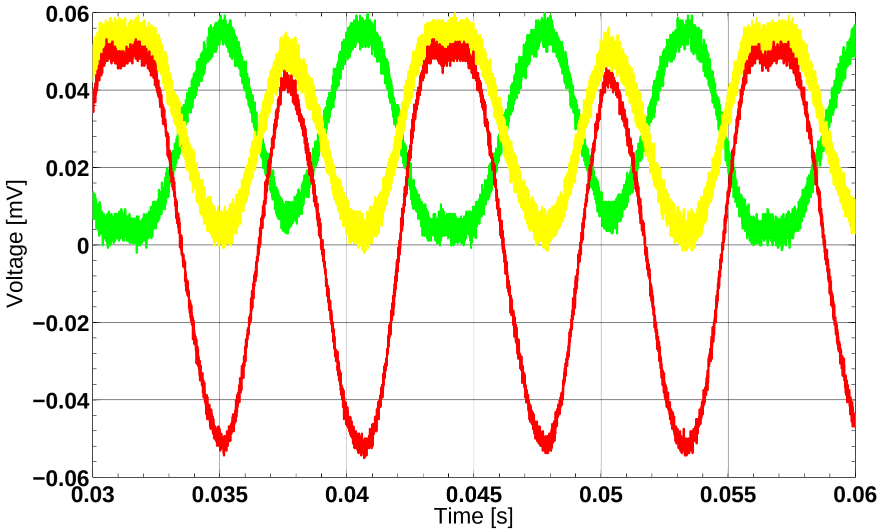

Figure 3.17.: The homodyne detectors HD2 outputs. Both the photodetectors PD3 (yellow curve) and PD4 (green curve) show an interference pattern with a visibility $(V_{max} - V_{min}/V_{max} + V_{min})$ of $\approx$ 99%. It is noticeable that the high frequency noise due to the 12 MHz sidebands. The error-signal is the difference photocurrent detected by the two photodetectors PD3 and PD4 represented in the red curve.

3.4.2. Homodyne detector stabilisation

The homodyne stabilisation can be achieved using either as an error-signal the low-frequency (DC) difference photocurrents detected by the two homodyne photodetectors or demodulating the phase modulated signal as described in the previous Section 3.4.1. The difference photocurrents of the homodyne detectors can be expressed in general as (see Appendix B):

$$\begin{aligned}
\mathbf{I_{21}} &= 2\sum_{i=0}^{N}\sum_{j=0}^{M}\Im\{a_i b_j^* e^{\mathrm{i}\omega_{ij}t}e^{\mathrm{i}\varphi_{ij}}\} = &(3.20)\\
&= 2\left(\sum_{i=0}^{N}\Im\{a_i b_i e^{\mathrm{i}\varphi_{ii}}\} + \sum_{j=i+1}^{N}\Im\{a_i b_j^* e^{\mathrm{i}\omega_{ij}t}e^{\mathrm{i}\varphi_{ij}} + b_i^* a_j e^{-\mathrm{i}\omega_{ij}t}e^{-\mathrm{i}\varphi_{ij}}\}\right) &(3.21)
\end{aligned}$$

that is, with an appropriate low-pass filter, the homodyne error-signal for the DFI setup, which provides a carrier a_0 and the two sidebands $a_{1,2}$ on one path and a carrier b_0 and two sidebands $b_{1,2}$ on the LO path. It can be expressed as:

$$\mathbf{I_{21}} = 2\sum_{i=0}^{N}\Im\{a_i b_i e^{\mathrm{i}\varphi_{ii}}\} = 2\Im\{(a_0 b_0 + a_1 b_1 + a_2 b_2)\, e^{-\mathrm{i}\varphi_H}. \qquad (3.22)$$

Fig. 3.16 shows the homodyne HD1 outputs when a ramp is applied on the phase shifter PS1 and the cavity is locked on its detuned state. Both the photodetectors PD1 (yellow curve) and PD2 (green curve) show an interference pattern with a visibility ($V_{max} - V_{min}/V_{max} + V_{min}$) of $\approx$ 93%. The error-signal is the difference photocurrent detected by the two photodetectors PD1 and PD2 represented in the red curve.

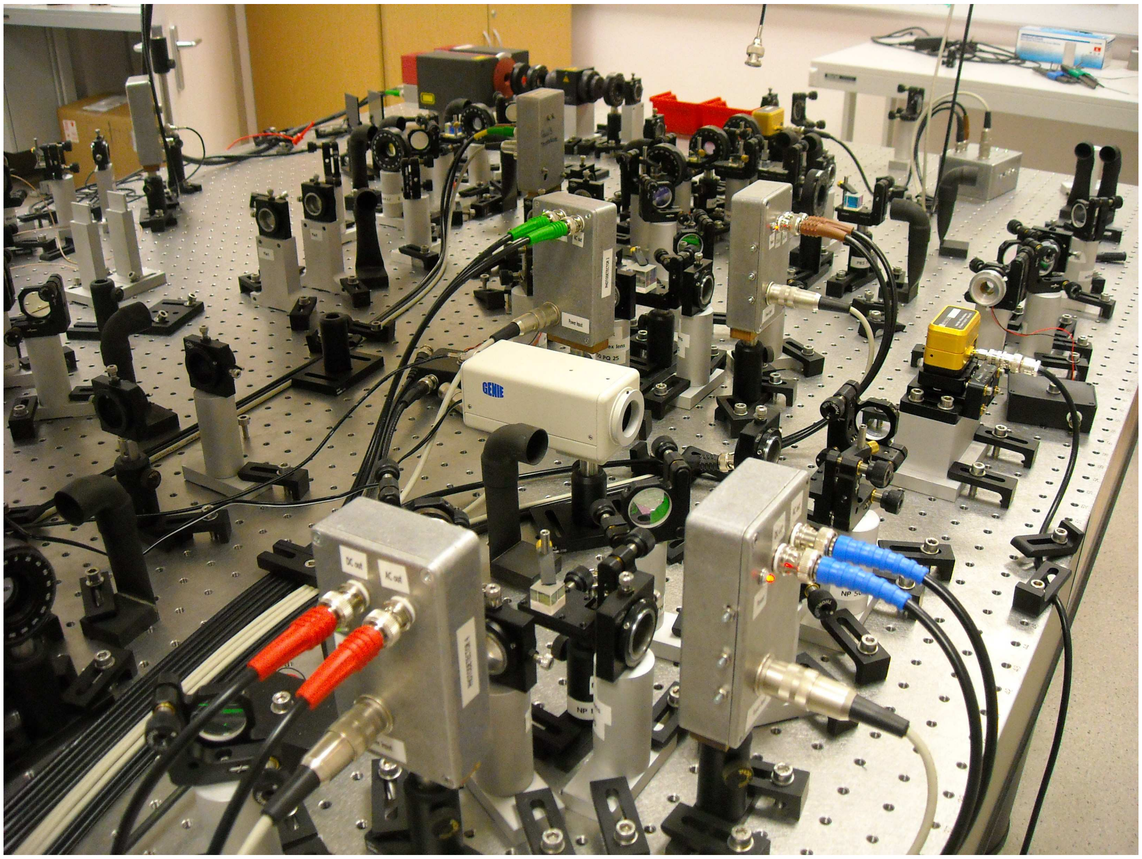

Figure 3.18.: This is a picture of the real experimental setup.

Fig. 3.17 shows the homodyne HD2 outputs when a ramp is applied on the phase shifter PS2 and the cavity is locked on its detuned state. Both the photodetectors PD3 (yellow curve) and PD4 (green curve) show an interference pattern with a visibility of ≈ 99%. The error-signal is the difference photocurrent detected by the two photodetectors PD3 and PD4 represented in the red curve.

3.5. Pictures of the experimental setup

In this Section pictures of the real experimental setup are shown.

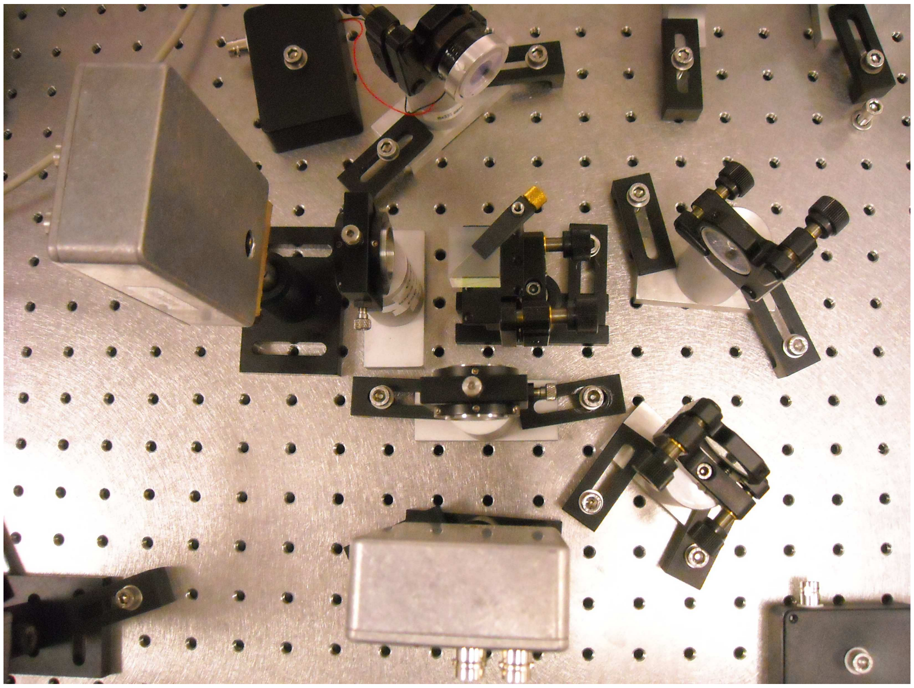

Figure 3.19.: This is a picture of the real homodyne detector setup.

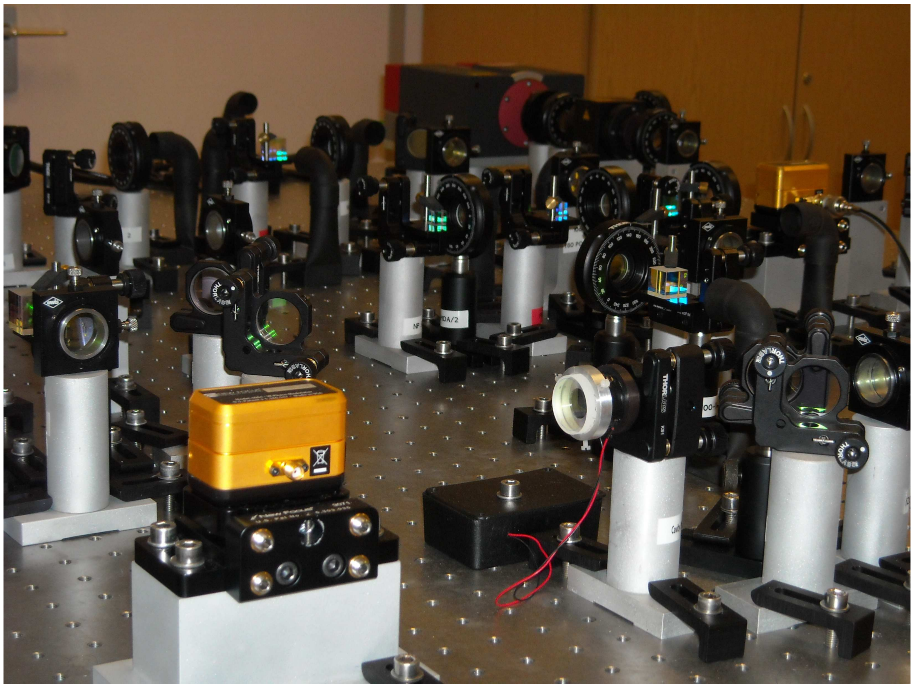

Figure 3.20.: This is a picture of the real PZT attached to the input cavity mirror.

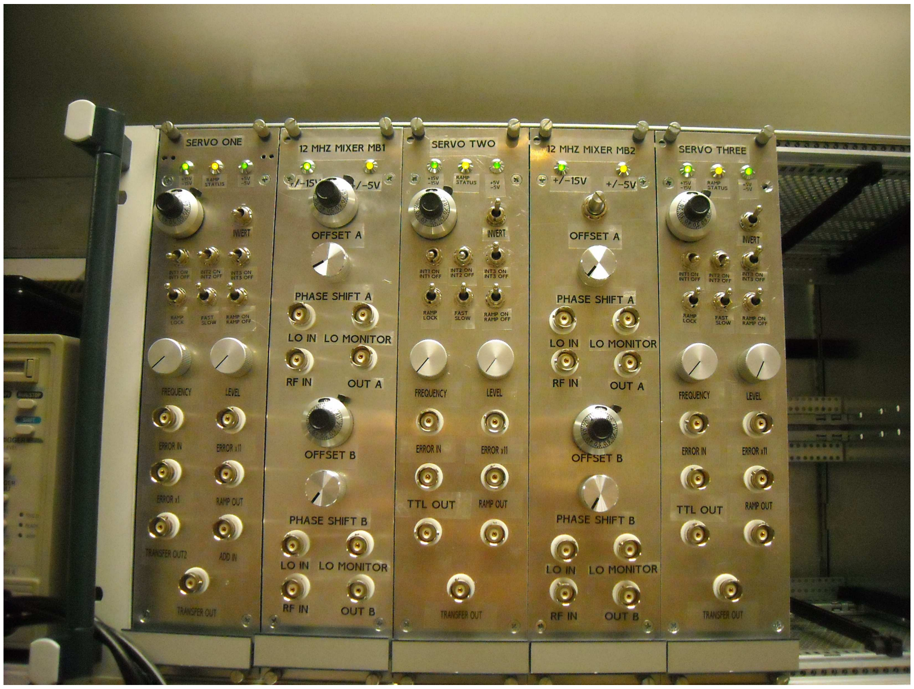

Figure 3.21.: This is a picture of mixers and servos used to control the cavity and the two homodyne detectors.

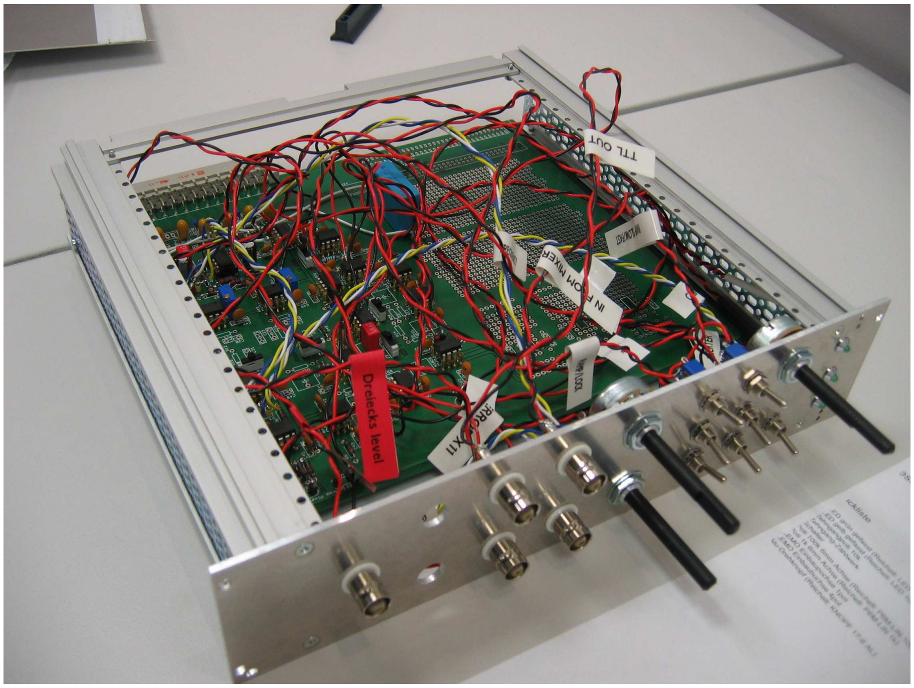

Figure 3.22.: This is a picture of a servo during its construction.

Fig. 3.18 shows a picture of the real setup, while Fig. 3.19 and Fig. 3.20 show the pictures of one of the homodyne detectors and the PZT attached to the input cavity mirror, respectively. Finally the last two pictures partially show the electronics used in this work. In particular Fig. 3.21 shows the crate with mixers and servos used to control the FP-cavity and the homodyne detectors, while Fig. 3.22 shows the servo used during the construction.

This Chapter showed the features of the experimental setup entirely realised in this work for the demonstration of DFI at low frequency applied to a FP-cavity. Electronic devices have been built for this experiment following the diagrams shown in Appendix D.

Chapter 4.

DFI Simulation

The experimental setup described in Chapter 3 has been based on the information obtained from the DFI simulation. This Chapter shows the demonstration of DFI for a detuned FP-cavity within the simulated environment using the Finesse software [FHL$^+$04]. It shows that the displacement noise injected on the input cavity mirror (IM) can be strongly suppressed while the GW is retained. The simulated setup was minimised to keep the basic features of the experimental setup.

4.1. Simulated setup

The simulated setup is shown in Fig. 4.1. The light originating from the laser is split into two beams, one to pump the FP-cavity and one to provide the two local oscillators (LO) for the homodyne detectors HD1 and HD2. The output of the two homodyne detectors is the difference signal given respectively by HD1=PDH1a-PDH1b and HD2=PDH2a-PDH2b. The FP-cavity used is formed by two identical mirrors which are separated by 30 cm. Each mirror has a power reflectivity of 98.5 % and a radius of curvature of 1 m which results in a cavity bandwidth of 2.4 MHz.

The reflected and transmitted signals from the cavity are individually sensed with the two homodyne detectors HD1 and HD2. These detectors allow to measure signals in an arbitrary quadrature in between amplitude and phase quadrature. Here the local oscillator power is much stronger than the signal beam for each homodyne detector, thus fulfilling the condition whereby the LO has to be much stronger than the signal power to ensure that the resulting signal is dominated by the signal on the signal beam and not by noise present on the LO [Bac98]. Since the DFI responses for a FP-cavity depends on which quadratures the homodyne detectors are set, an appropriate use of the homodyne beam splitters tuning can be used to define the quadratures of both the reflected and the transmitted fields.

4.2. Homodyne quadratures

The reflected and the transmitted light from the cavity interfere respectively on the beamsplitters BSH1 and BSH2 with the light reference beam coming from the laser (LO). The intensity is a sinusoidal function of the optical path $\Delta\phi = \frac{2\pi}{\lambda}\Delta x$, where λ is the wavelength of the laser and Δx is the path difference of the two waves. Path changes of λ provide a complete cycle of the intensity.

The interference pattern detected by each single photodetector in both homodyne detectors HD1 and HD2, are shown in Fig. 4.2 where the optical path is tuned with the homodyne beam splitters BSH1 and BSH2.

At a BSH1 tuning of $51.3°$ the homodyne HD1 measures the phase quadrature

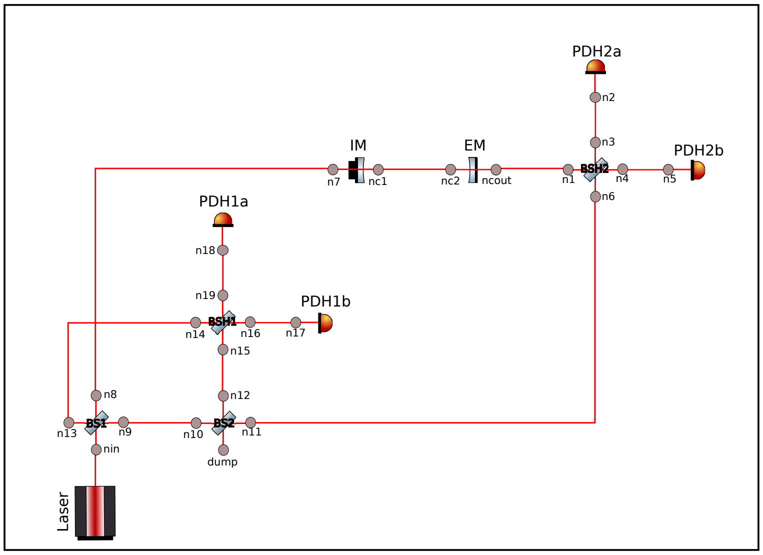

Figure 4.1.: Simulated setup. The setup is provided by a FP-cavity kept in its detuned state of 12 MHz and two homodyne detectors. One homodyne detector is used to sense the reflected light from the cavity and one is used to sense the transmitted light from the cavity. Both the homodyne detectors are provided with reference beam (LO) interfering on BSH1 and BSH2 respectively for the homodyne detectors HD1 and HD2, where HD1 = PDH1a − PdH1a and HD2 = PDH2a − PDH2a.

(PQ) of the reflected beam from the cavity where the two photodetectors intensities have the same amplitude. At a BSH1 tuning of 96.3° HD1 measures the amplitude quadrature (AQ) of the reflected beam from the cavity where the two photodetectors intensities have opposite amplitude.

Similarly, at a BSH2 tuning of 34.7° the homodyne HD2 measures the phase quadrature of the transmitted beam from the cavity where the two photodetectors intensities have the same amplitude. At a BSH2 tuning of 79.7° HD2 measures the amplitude quadrature of the transmitted beam from the cavity where the two photodetectors intensities have opposite amplitude.

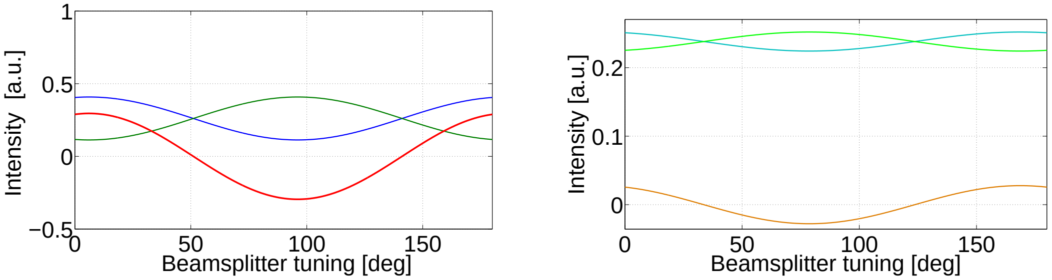

Figure 4.2.: Homodyne detectors signals output. On the left-hand side are shown the signals of HD1. The blue and the green line are the intensities detected in the photodetectors. The red curve represents the output signal of HD1. On the right-hand side are shown the signals of HD2. The cyan and the light-green line are the intensities detected in the photodetectors. The orange curve represents the output signal of HD2. Both plots show that phase and amplitude quadratures are 45° phase shifted.

4.3. DFI combination algorithm

The DFI has the requirement of a multiple channel experiment in which their combination creates a new channel which is free from displacement noise while the GW signal is still present.

To demonstrate the detuned FP-cavity based DFI scheme, the displacement noise and the GW responses have been simulated.

The two transfer functions from the cavity input mirror IM to the two homodyne detectors are the displacement noise responses $S1_{\mathrm{DN}}$ and $S2_{\mathrm{DN}}$ respectively in HD1 and HD2. On the other hand the two transfer functions from the cavity-length to the two homodyne detectors are the GW signal responses $S1_{\mathrm{GW}}$ and $S2_{\mathrm{GW}}$ respectively. Both the DN and GW responses allow the creation of two new channels with $S_{\mathrm{DN,DFI}}$ and $S_{\mathrm{GW,DFI}}$ being respectively the DN and GW responses of the DFI.

These new DFI data are given by:

$$\begin{aligned} S_{\mathrm{DN,DFI}\pm} &= S1_{\mathrm{DN}} \pm k \cdot S2_{\mathrm{DN}}, \\ S_{\mathrm{GW,DFI}\pm} &= S1_{\mathrm{GW}} \pm k \cdot S2_{\mathrm{GW}}. \end{aligned} \tag{4.1}$$

here k represents a fixed scaling factor which minimises the DN content in channel $S_{\mathrm{DN,DFI}}$. In the simulation an arbitrary k is chosen to be the ratio of the DN transfer function magnitude at 1 Hz ($k = S1_{\mathrm{DN_A}}[1\,\mathrm{Hz}]/S2_{\mathrm{DN_A}}[1\,\mathrm{Hz}]$), as changing the frequency for determining k does not change the results. Afterwards the DFI effect is evaluated by comparing the DFI SNR and the initial unprocessed data SNRs.

In this thesis the SNRs are defined as follow:

The signal-to-noise ratios (SNRs) σ of the initial unprocessed data channels of $S1$ and $S2$ are given by $\sigma_{\mathrm{S1}} = S1_{\mathrm{GW}}/S1_{\mathrm{DN}}$ and $\sigma_{\mathrm{S2}} = S2_{\mathrm{GW}}/S2_{\mathrm{DN}}$ and show how good a GW can be detected with respect to the present DN. For the processed data channels a similar SNR given by $\sigma_{\mathrm{DFI}\pm} = S_{\mathrm{GW,DFI}\pm}/S_{\mathrm{DN,DFI}\pm}$ can be calculated, where plus and minus correspond to the sum and difference combination DFI+, DFI- respectively used in equations 4.1. To see the enhancement effect of the DFI, the ratio ρ_i between the processed and unprocessed SNRs $\rho_{\mathrm{S1}\pm} = \sigma_{\mathrm{DFI}\pm}/\sigma_{\mathrm{S1}}$ and $\rho_{\mathrm{S2}\pm} = \sigma_{\mathrm{DFI}\pm}/\sigma_{\mathrm{S2}}$ are evaluated.

On the other hand, since the resulting transfer functions depend on which quadratures the homodyne detectors are able to detect, an analysis of the homodyne quadratures is provided in the following Section. In this case the analysis is done by simulating the DN and GW transfer functions at a fixed frequency and studying their behaviour against the homodyne quadratures. The DFI effect can be

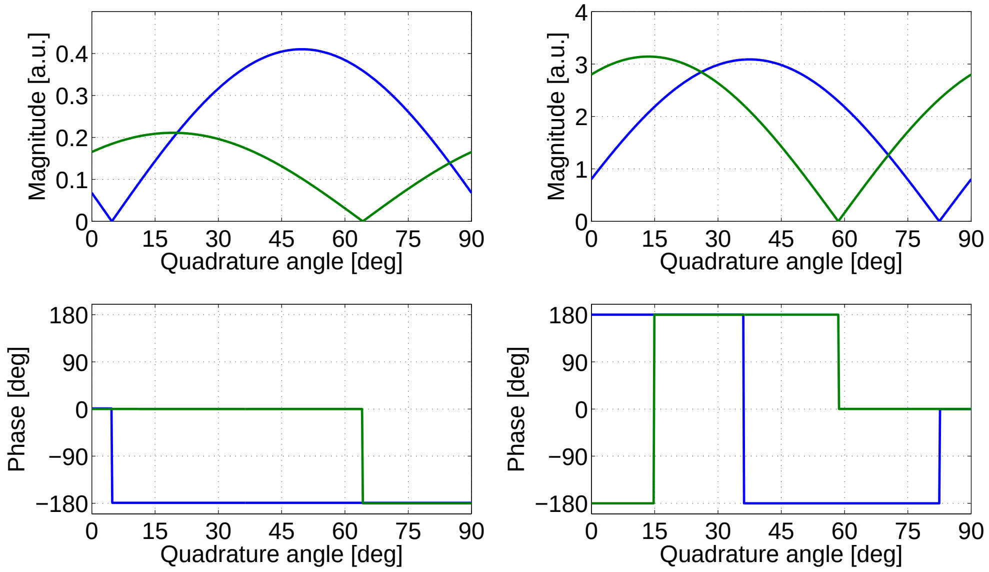

Figure 4.3.: DN and the GW transfer functions at fixed frequency vs quadrature angle. The scanning of the quadratures starts when both the homodyne detectors are in amplitude quadratures. The left-hand side of shows the DN transfer functions from the input cavity mirror to HD1 (blue curve) and HD2 (green curve). The right-hand side shows the GW transfer functions from the cavity-length to HD1 (blue curve) and HD2 (green curve).

evaluated equally as mentioned above in this Section.

4.4. Homodyne detectors quadratures analysis

4.4.1. Scanning the quadrature angles: HD1 and HD2 start in amplitude quadrature

In this subsection the homodyne quadratures analysis is done by calculating the DN and the GW transfer functions at fixed frequency against the quadrature angles, where the scanning of the quadratures starts when both the homodyne detectors

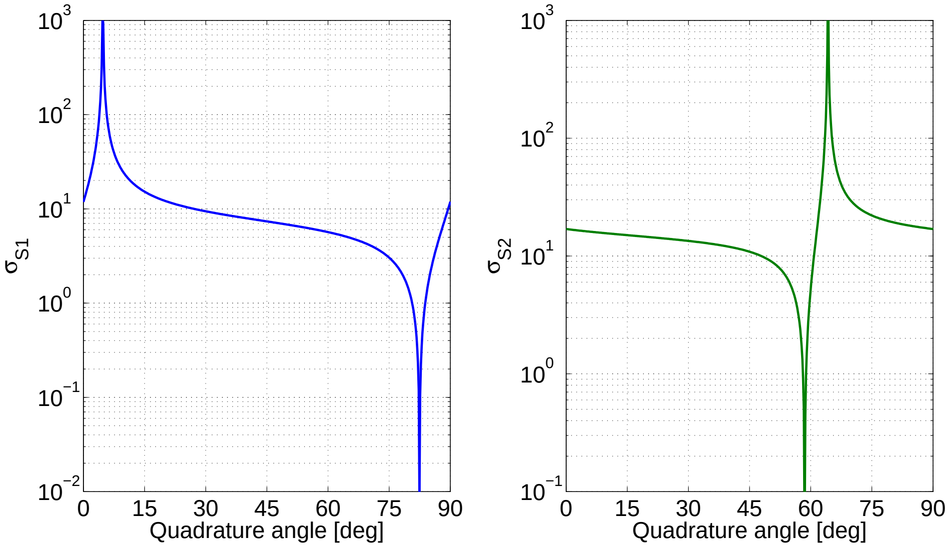

Figure 4.4.: SNRs of the unprocessed data vs quadrature angle. Tunings at 0° give both the homodynes detector in amplitude quadratures, while tunings at 45° give both the homodyne detectors in phase quadrature. On the left-hand side is plotted the SNR in HD1 (σ_{S1}). On the right-hand side is plotted the SNR in HD2 (σ_{S2}).

are in amplitude quadrature. The entire cycle of the quadratures goes for tunings of both BSH1 and BSH2 from 0° to 90°. Tunings at 0° give both the homodynes detectors in amplitude quadratures, while tunings at 45° give both the homodyne detectors in phase quadrature.

To this aim, the left-hand side of Fig. 4.3 shows the DN transfer functions from the input cavity mirror to HD1 (blue curve) and HD2 (green curve), respectively named $S1_{\mathrm{DN}}$ and $S2_{\mathrm{DN}}$, as functions of quadrature angles. $S1_{\mathrm{DN}}$ has a minimum of zero at 4.7° while $S2_{\mathrm{DN}}$ has a minimum of zero at 64.5°. In between these two points the respective phases are shifted of 180°. The right-hand side of Fig. 4.3 shows the GW transfer functions from the cavity-length to HD1 (blue curve) and HD2 (green curve), respectively named $S1_{\mathrm{GW}}$ and $S2_{\mathrm{GW}}$. $S1_{\mathrm{GW}}$ has a minimum of zero at 82.4° while $S2_{\mathrm{GW}}$ has a minimum of zero at 58.5°. In between these two points the respective phases are shifted by 180°.

Fig. 4.4 shows the initial SNRs, σ_{S1} and σ_{S2}, of the unprocessed data respectively in HD1 (left-hand side) and HD2 (right-hand side). σ_{S1} has a peak at 4.7° and a minimum at 82.4°, while σ_{S2} has a peak at 64.5° and a minimum at 58.5°.

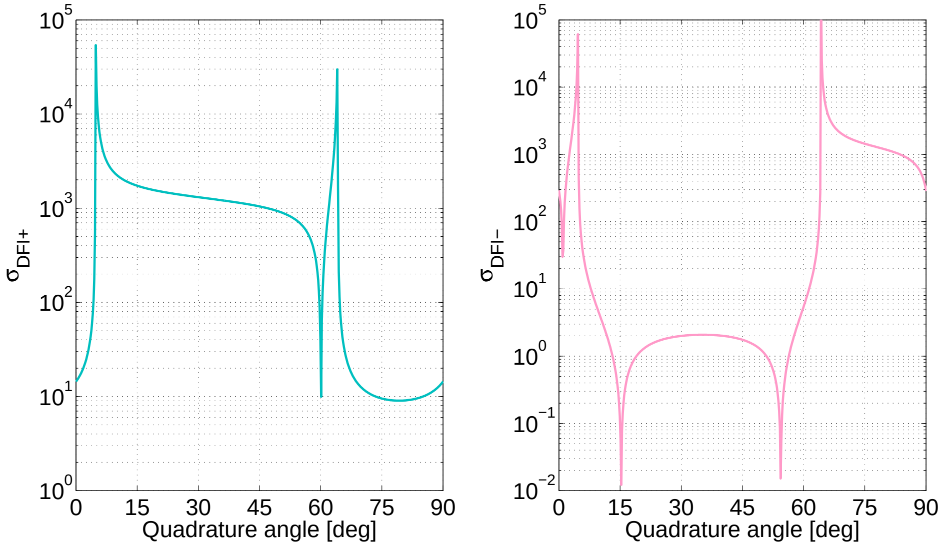

Figure 4.5.: SNRs of the DFI processed data vs quadrature angles. Tunings at 0° give both the homodynes detector in amplitude quadratures, while tunings at 45° give both the homodyne detectors in phase quadrature. On the left-hand side the SNR of the DFI+ channel ($\sigma_{\mathrm{DFI+}}$). On the right-hand side the SNR of the DFI- channel ($\sigma_{\mathrm{DFI-}}$).

To evaluate how the DFI channels are sensitive to a GW signal one can look at the SNRs of the DFI processed data in Fig. 4.5. From here can be seen which DFI channel is more sensitive to the GW signal in correspondence to any quadrature angles. On the left-hand side the SNR of the DFI+ channel, $\sigma_{\mathrm{DFI+}} = S2_{\mathrm{GW,DFI+}}/S2_{\mathrm{DN,DFI+}}$, where the latter is built taking into account the plus sign in the equations 4.1. On the right-hand side the SNR of the DFI- channel, $\sigma_{\mathrm{DFI-}} = S2_{\mathrm{GW,DFI-}}/S2_{\mathrm{DN,DFI-}}$, where the latter is built taking into account the plus sign in the equations 4.1. Both $\sigma_{\mathrm{DFI+}}$ and $\sigma_{\mathrm{DFI-}}$ show peaks at 4.7° and 64.5°. In between those two values $\sigma_{\mathrm{DFI+}}$

is relatively high varying from $\approx 10^2$ to $\approx 10^4$ with a minimum of ≈ 10 at 60°. In the complementary interval $\sigma_{\mathrm{DFI}-}$ shows relative high values varying from $\approx 10^2$ to $\approx 10^4$ as well.

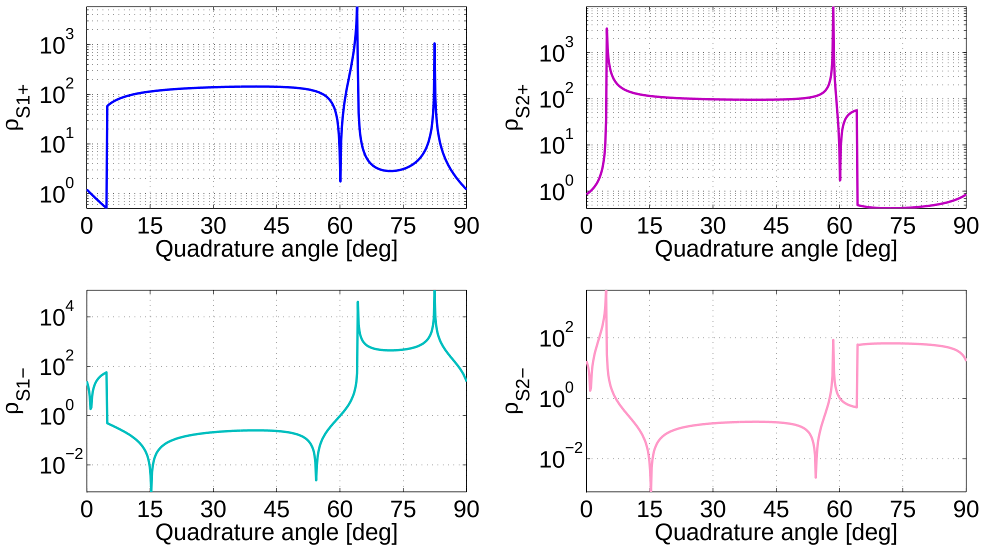

Figure 4.6.: Enhancement effect of the DFI. Tunings at 0° give both the homodyne detectors in amplitude quadratures, while tunings at 45° give both the homodyne detectors in phase quadrature. The ratio ρ_i between the processed and unprocessed SNRs against the quadrature angles are evaluated. The plots are organised as follows: On the top-left-hand side $\rho_{\mathrm{S1+}}$. On the top-right-hand side $\rho_{\mathrm{S2+}}$. On the bottom-left-hand side $\rho_{\mathrm{S1-}}$. On the bottom-right-hand side $\rho_{\mathrm{S2-}}$.

Finally one can evaluate the enhancement effect ρ_i of the DFI. In Fig. 4.6 the ratio ρ_i between the processed and unprocessed SNRs are evaluated. The plots are organised as follows: On the top-left-hand side $\rho_{\mathrm{S1+}} = \sigma_{\mathrm{DFI+}}/\sigma_{\mathrm{S1}}$. On the top-right-hand side $\rho_{\mathrm{S2+}} = \sigma_{\mathrm{DFI+}}/\sigma_{\mathrm{S2}}$. On the bottom-left-hand side $\rho_{\mathrm{S1-}} = \sigma_{\mathrm{DFI-}}/\sigma_{\mathrm{S2}}$. On the bottom-right-hand side $\rho_{\mathrm{S2-}} = \sigma_{\mathrm{DFI-}}/\sigma_{\mathrm{S2}}$.

$\rho_{\mathrm{S1+}}$ shows two peaks of $\approx 10^4$ and $\approx 10^3$ respectively at 64.5° and 82.4°. In the region between 10° and 55° a relative high enhancement effect $\rho_{\mathrm{S1+}}$ of ≈ 150

is shown. In the same region $\rho_{\mathrm{S2}+}$ shows approximately the same relative high enhancement effect of ≈ 100 and a peak of $\approx 10^4$ at 58.5°. On the other hand $\rho_{\mathrm{S1}-}$ shows an enhancement effect of $\approx 10^3$ in region in between two peaks of $\approx 10^4$ and $\approx 10^5$ respectively at 64.5° and 82.4°. In contrast in the same region $\rho_{\mathrm{S2}-}$ shows an enhancement effect of ≈ 80. $\rho_{\mathrm{S1}-}$ and $\rho_{\mathrm{S2}-}$ also show peaks at 4.7°.

4.5. DFI in phase quadrature

The quadrature analysis presented in Section 4.4 and Appendix C is crucial to the execution of the DFI experiment described in this thesis. This quadrature analysis shows several homodyne beam splitter settings for which the noise cancelation mechanism gives interesting results.

It must be mentioned that at certain quadrature angles the homodyne detector response to a DN at a fixed frequency is zero. The response to a similarly fixed-frequency GW signal is zero at different angles, as shown in Figures 4.3, C.1, C.5. At these points the scaling factor required for producing DFI signal is infinite and theoretically an infinite suppression of DN can be achieved. These settings may appear to be the best to use for the experimental measurement of DFI response, in fact this is not the case. The aim of this demonstration is to show the more general case where high DFI SNR can be achieved, without narrowing the discussion to a single readout quadrature specific to the setup described here. It is clear that the noise cancelation for a detuned FP-cavity relies on the readout quadrature chosen for each homodyne detector. Although the DFI response has not been constructed for each possible combination of readout quadratures, the aforementioned analysis points towards areas of interest where the DFI SNR is expected to be high. DN and GW transfer functions have been performed at fixed frequencies against the quadrature angles. The initial SNRs in each homodyne detector, the DFI channel SNR and the factor with which it improved have also been studied versus the quadrature angles. The scanning of these quadrature angles has been done in three different ways:

The noise cancelation for a detuned FP-cavity relies on which quadrature angles are set in each homodyne detectors. Although this has not being done for all possible cases, the quadrature analysis shown gives helpful information of which quadrature angles gives high DFI response. DN and GW transfer functions have been performed at fixed frequency and studied against the quadrature angles. The initial SNRs in each homodyne detectors, the DFI channel SNR and its improving factor have also been studied against the quadrature angles. The scanning of the quadrature angles has been done in three different way:

- HD1 and HD2 start in AQ;
- HD1 starts in AQ and HD2 in PQ;
- HD1 and HD2 start at maximum GW detection;

In the first case in the region between 10° and 55° a relatively high enhancement effect $\rho_{\mathrm{S1+}}$ and $\rho_{\mathrm{S2+}}$ of ≈ 150 and ≈ 100 respectively is shown. On the other hand in the region between 64.5° and 82.4°, an enhancement effect of $\approx 10^3$ and ≈ 80 is shown for $\rho_{\mathrm{S1-}}$ and $\rho_{\mathrm{S2-}}$ respectively.

In the second case in the region between 25° and 65° a relativly high enhancement effect $\rho_{\mathrm{S1+}}$ and $\rho_{\mathrm{S2+}}$ of ≈ 200 and ≈ 100 respectively is shown. On the other hand in a region in between 5° and 20°, an enhancement effect of ≈ 70 and ≈ 200 is shown for $\rho_{\mathrm{S1-}}$ and $\rho_{\mathrm{S2-}}$ respectively.

In the third case in the region in between 5° and 75° $\rho_{\mathrm{S1-}}$ and $\rho_{\mathrm{S2-}}$ show an enhancement effect of ≈ 300 and ≈ 150 respectively.

From this analysis it can be noticed that, the setting of the two homodyne angles in phase quadrature, which correspond essentially to the first case at 45° angle, is a good option that ensures a high DFI enhancement of the new created DFI+ channel in both the homodyne detectors. From the experimental point of view this is a more practical choice where the locking of the two homodyne detectors can be achieved using as an error signal the difference of the two homodyne photodetectors, without the use of any other electronic devices.

4.5.1. Example of DFI transfer functions

The previous quadrature analysis shows that a relative high improvement of SNR for DFI+ channel is given when both the homodyne detectors are in phase quadrature. In the following an example of DFI measurements for such quadrature angle is presented.

As already mentioned the two transfer functions from the cavity input mirror IM to the two homodyne detectors $S1_{\mathrm{DN}}$ and $S2_{\mathrm{DN}}$ are the displacement noise responses. On the other hand the two transfer functions from the cavity-length to the two homodyne detectors $S1_{\mathrm{GW}}$ and $S2_{\mathrm{GW}}$ are the GW signal responses respectively. The transfer functions are plotted in Fig. 4.7.

As one can see the two transfer functions for the displacement noise from the cavity input mirror IM to the two homodyne detectors $S1_{\mathrm{DN}}$ (blue curve) and $S2_{\mathrm{DN}}$ (green

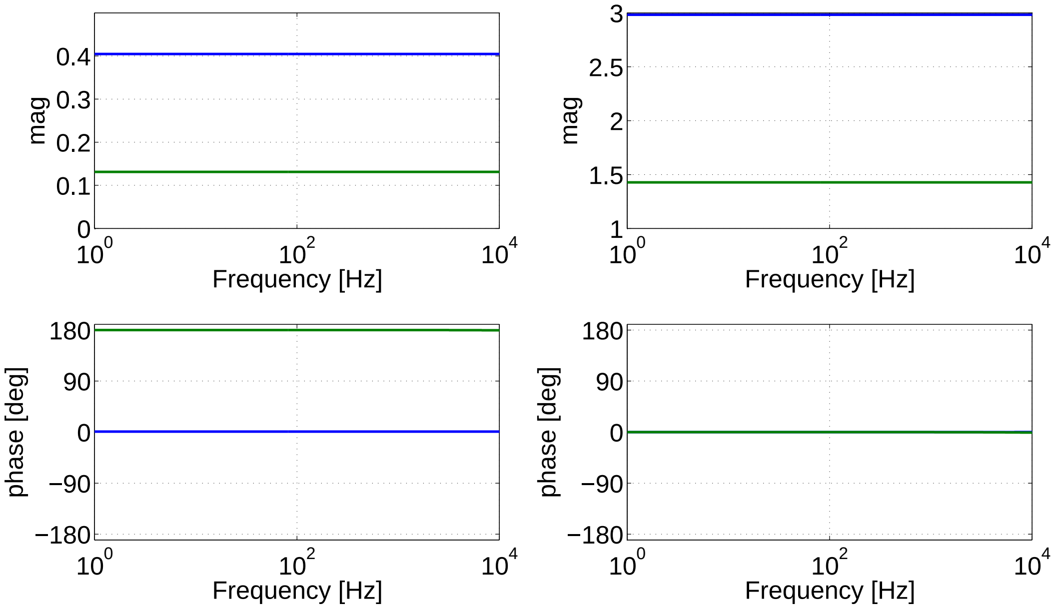

Figure 4.7.: Simulated transfer functions when both HD1 and HD2 are in phase quadrature. On the left-hand side there are plotted the DN transfer functions while on the right-hand side are plotted the GW transfer functions.

curve) are out of phase by 180° in the entire frequency range. On the other hand the two GW signal transfer functions $S1_{\mathrm{GW}}$ (blue curve) and $S2_{\mathrm{GW}}$ (green curve) are in phase. All transfer functions include phase shifts induced by the optical elements that the reflected and transmitted light from the cavity passes before the detection in the homodyne detectors $S1$ and $S2$ respectively.

4.5.2. DFI combined channels transfer functions

From both the displacement noise and GW responses one can create new channels with $S_{\mathrm{DN,DFI}}$ being the DFI displacement noise response and $S_{\mathrm{GW,DFI}}$ being the DFI GW response. These new DFI data are given in equations 4.1.

Fig. 4.8 shows the combined transfer functions of the new DFI channel. On the left-hand side the new DFI displacement noise and DFI gravitational wave transfer functions $S_{\mathrm{DN,DFI+}}$ (blue curve) and $S_{\mathrm{GW,DFI+}}$ (green curve) respectively are shown. These are obtained from equations 4.1 using the sum. On the right-hand side the new DFI displacement noise and DFI gravitational wave transfer functions $S_{\mathrm{DN,DFI-}}$ (blue curve) and $S_{\mathrm{GW,DFI-}}$ (green curve) respectively are shown. Those are obtained from equations 4.1 using the difference.

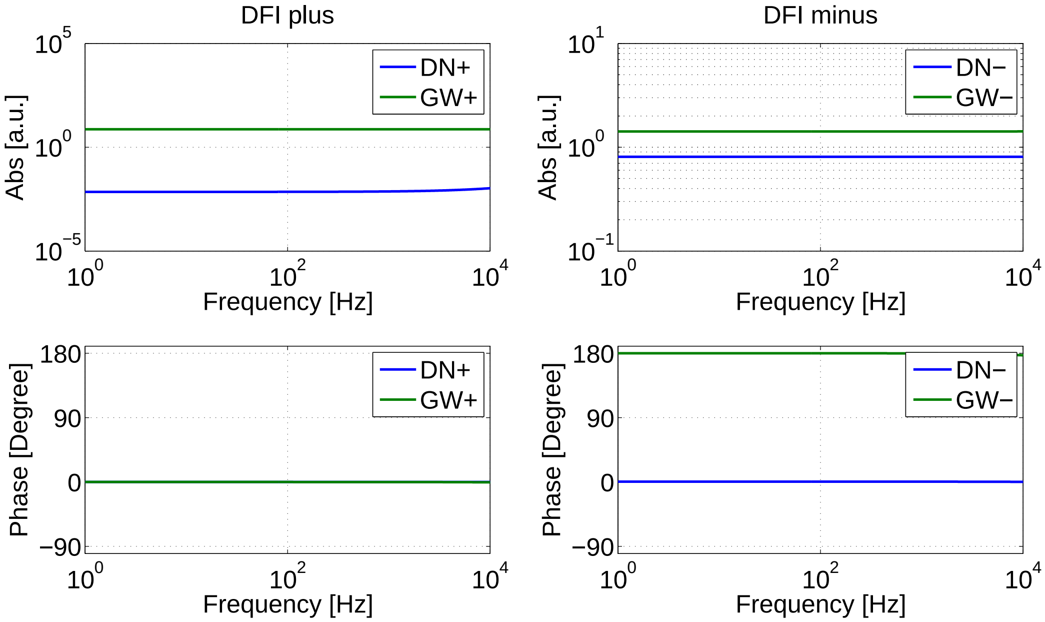

Figure 4.8.: The combined transfer functions of the new DFI channel. On the left-hand side the new DFI displacement noise and DFI gravitational wave transfer functions respectively, $S_{\mathrm{DN,DFI+}}$ (blue curve) and $S_{\mathrm{GW,DFI+}}$ (green curve). On the right-hand side the new DFI displacement noise and DFI gravitational wave transfer functions respectively, $S_{\mathrm{DN,DFI-}}$ (blue curve) and $S_{\mathrm{GW,DFI-}}$ (green curve).

Recalling that for the processed data channels the SNR is given by

$$\sigma_{\mathrm{DFI\pm}} = S2_{\mathrm{GW,DFI\pm}}/S2_{\mathrm{DN,DFI\pm}} \tag{4.2}$$

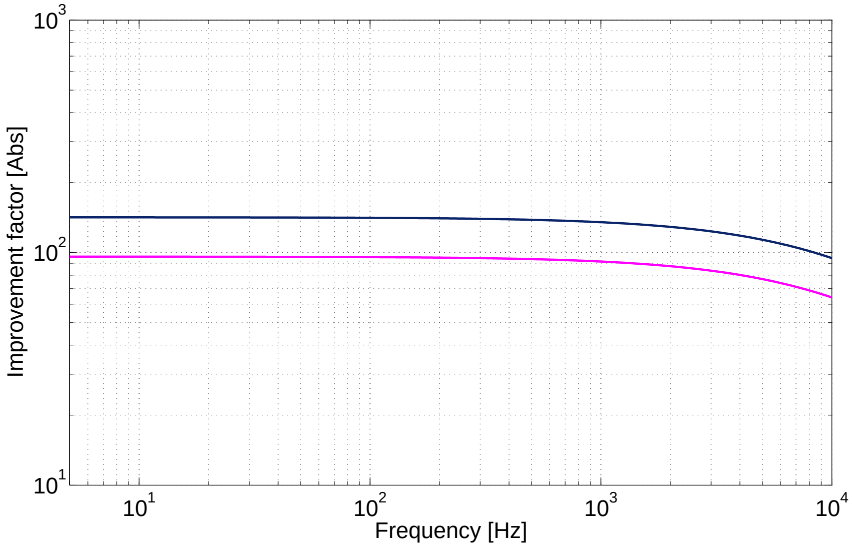

Figure 4.9.: Improvement in SNR of the DFI scheme. The improvement due to the DFI scheme is expressed by the ratio ρ_i between the processed SNR σ_{DFI} and unprocessed SNRs σ_{S1} and σ_{S2}.

one can see $\sigma_{\mathrm{DFI+}}$ has a relative high value since for the new DFI channel displacement noise has been suppressed and the GW signal has been retained.

4.5.3. DFI simulated results

The improvement due to the DFI scheme is expressed by the ratio ρ_i between the processed SNR, $\sigma_{\mathrm{DFI\pm}}$, and unprocessed SNRs, σ_{S1} and σ_{S2}. In particular here $\sigma_{\mathrm{DFI+}}$ has been evaluated. The two resulting ratios $\rho_{\mathrm{S1}} = \sigma_{\mathrm{DFI}}/\sigma_{\mathrm{S1}}$ (blue curve) and $\rho_{\mathrm{S2}} = \sigma_{\mathrm{DFI}}/\sigma_{\mathrm{S2}}$ (pink curve) show an improvement of ≈ 140 and of ≈ 95 respectively over the whole frequency range.

It is useful to mention that the analysis so far have been performed taking into account an expected feature of a realistic setup. In particular it has been seen that the noise cancelation mechanism relies on phase relations between the DN and GW

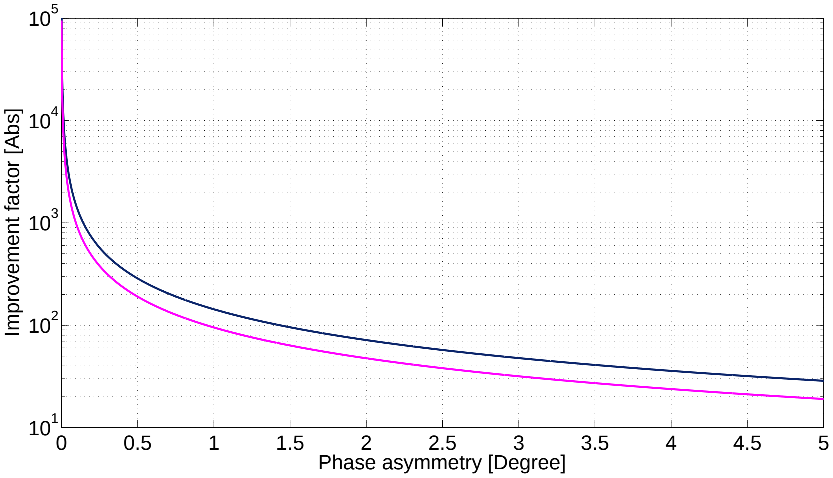

Figure 4.10.: Improvement factor as a function of the asymmetry ϕ. In the ideal case of $\phi = 0$ the improvement factor diverges. Increasing the asymmetry reduces the improvement factor. In particular when $\phi = 1$ the factors achieved are $\rho_1 = 140$ and $\rho_1 = 95$ respectively in HD1 and HD2.

responses. If one considers the DFI- channel, from the first term of equation 4.1 it may be noticed that if the phases of the two homodyne transfer functions $S1_{\mathrm{DN}}$ and $S2_{\mathrm{DN}}$ are the same a perfect noise cancelation occurs in the new DFI channel leading to the improvement factor ρ being infinite. However non-ideal components cannot ensure a perfect phase matching of the homodyne detector transfer functions. For this reason the simulation takes into account this effect, replacing the DN response in equation 4.1 with

$$S_{\mathrm{DN,DFI}\pm} = S1_{\mathrm{DN}} e^{i\phi} \pm k \cdot S2_{\mathrm{DN}}, \tag{4.3}$$

where $\phi = 1^\circ$ is the phase asymmetry considered in the simulations provided in this thesis and $k = |S1_{\mathrm{DN}}|/|S2_{\mathrm{DN}}|$ represents a fixed scaling factor. It is then straightforward express the improvement factor ρ as a function of the asymmetry angle ϕ as follows:

$$\rho(\phi) = \frac{\alpha}{e^{i\phi} - 1}, \tag{4.4}$$

where $\alpha = |S_{\mathrm{GW,DFI}}|/|S1_{\mathrm{GW}}|$ for HD1 and $\alpha = |S_{\mathrm{GW,DFI}}| \cdot k/|S2_{\mathrm{GW}}|$ for HD2. Fig. 4.10 shows the improvement factor as a function of the asymmetry ϕ, when the two homodyne detectors are set in phase quadrature.

In conclusion in this Chapter it has been shown, with a simulated setup, the feasibility of the proposed detuned FP-cavity based DFI model. The responses at different quadratures have been studied in order to localize at which quadrature point the enhancement of the SNR is higher. This simulation is the guideline for the real experiment which is described in the next Chapter.

Chapter 5.

Measurements and experimental results

Presented in this Chapter is the first experimental proof of principle demonstration of the new DFI scheme based on the detuned FP-cavity proposed in [TV08]. Thus the core concept of this new idea which is the basis for newly proposed interferometer schemes [RV08] has been verified. One laser in combination with two homodyne detectors is used to suppress strongly the displacement noise of the input mirror of a FP-cavity with respect to a simulated GW signal. As a result a gain in the GW signal to displacement noise ratio in the frequency band from 10 Hz to 10 kHz of ~ 60 is obtained. The results described here provides the basis for the previously accepted paper [PCHF10].

5.1. DFI measurement description

The experimental setup of the detuned FP-cavity DFI based scheme described in detail in Chapter 3 is shown in Fig. 5.1. The light originating from the laser is split into two beams, one to pump the FP-cavity and one to provide the two local oscillators (LO) for the homodyne detectors HD1 and HD2, where the output of the two homodyne detectors is the difference signal given respectively by S1=PD1-PD2 and S2=PD3-PD4. The reflected and transmitted signals from the cavity are individually sensed with the two homodyne detectors HD1 and HD2. The homodyne detectors allow the possibility to measure signals in an arbitrary quadrature in between amplitude and phase quadrature. The local oscillator power is 25 mW, whereas the signal beams for the homodyne detectors are one order of magnitude weaker. This condition ensures that the resulting signal is dominated by the signal present in reflected and transmitted light from the cavity and not by noise present on the LO [Bac98].

The difference photocurrents of each homodyne detector, S1 and S2 for HD1 and HD2 respectively, are used to generate individual error signals for the homodyne detectors. Each error signal is fed back to the PZT actuators PS1 and PS2 respectively. This provides the necessary control to lock both homodyne detectors to phase quadrature. The control bandwidth of the cavity and the homodyne detector control loops are kept as low as possible, around $\sim 70\,\mathrm{Hz}$, in order to avoid the control loop affecting the DFI response in the low frequency region.

The electro-optic-modulator EOM2 is used to imprint a phase modulation on the light resonating inside the cavity simulating the effect of GW. By injecting a swept-sine signal into EOM2, one can measure a simulated GW transfer function to both

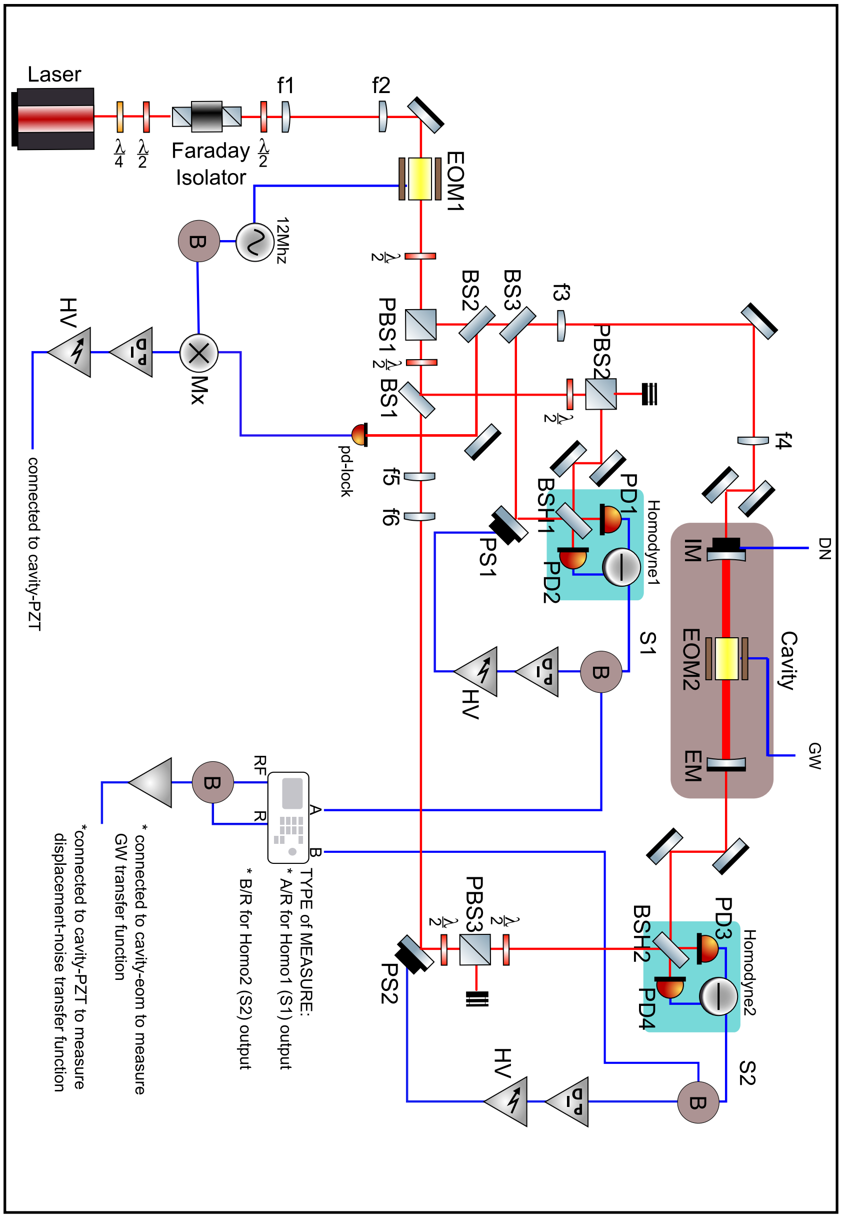

Figure 5.1.: DFI transfer functions setup. The laser pumps the cavity through the input cavity mirror (IM) and provides a local oscillator (LO) as reference beam to each homodyne detectors. The reflected and the transmitted light from the cavity contain the DN and GW signals, obtained one after the other. The signals are created respectively injecting a swept-sine signal onto the PZT attached on the IM and onto the EOM2. Both the DN and GW signals are sensed by the two homodyne detectors with outputs S1 and S2. These two signals are divided by an active buffer (B) to provide a feedback loop signal to control the homodyne detectors and to provide the signals to be measured by a network analyser.

homodyne detectors. The original scheme proposed in [TV08] includes the effects of the GW on the LO paths. This scheme however represents the case where the LO for HD2 can be provided by an independent laser.

The PZT attached to mirror IM is used to stabilise the cavity length by applying a feedback signal. Furthermore, the simulated displacement noise signal is imprinted on the light by applying swept-sine signal to this PZT which allows the possibility to measure a displacement noise transfer function to both homodyne detectors. Both transfer functions (DN and simulated GW) are measured using the homodyne outputs S1 and S2, thereby creating the basis for the demonstration of this DFI scheme.

5.2. Open loop transfer functions

In general the system loop performances can be seen by looking at the open loop transfer function. The unity gain frequency determines the frequency band within which the loop is able to suppress the disturbances acting on the system. The DFI experiment contains three loops as described in Chapter 3; the cavity loop and the two homodyne detector loops. Since the success of the DFI experiment is determined by the features of the control loops, the open loop transfer functions (OLTFs) of these systems are shown here.

The schematic measurement diagram of the OLTFs is shown in Fig. 5.2 and Fig. 5.3, for the cavity and HDs loops respectively. A swept-sine S, provided by a network analyser, is injected into the control loop, between the servo amplifier (PID) and the high voltage amplifier (HV), and the response to the signal S is measured.

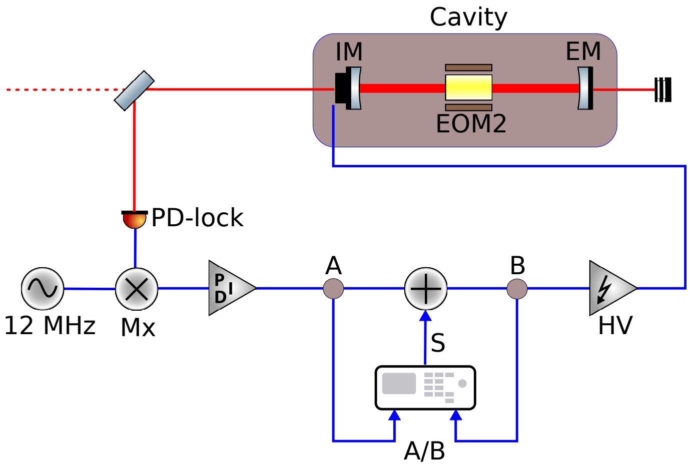

Figure 5.2.: The cavity open loop transfer function (OLTF) setup. A signal S, provided by a network analyser, is injected into the cavity control loop, in particular between the servo amplifier (PID) and the high voltage amplifier (HV). The response to the signal S is measured at the two points A and B and the OLTF is given by A/B.

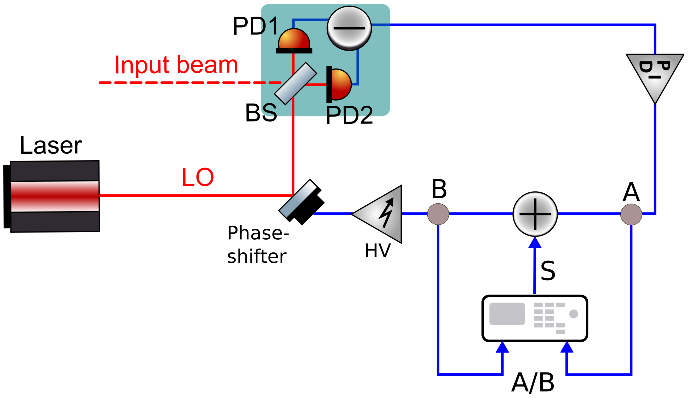

Figure 5.3.: The homodyne detectors (HDs) open loop transfer functions (OLTF) setup. A signal S, provided by a network analyser, is injected into the HDs control loop, between the servo amplifier (PID) and the high voltage amplifier (HV). The response to the signal S is measured at the two points A and B and the OLTF is given by A/B.

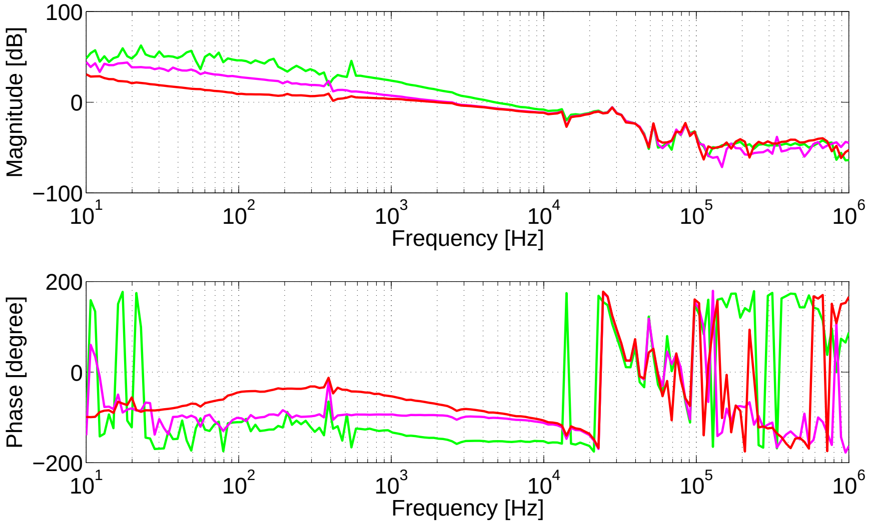

Figure 5.4.: The cavity open loop transfer function (OLTF) measured with the use of three servo integrators. The green curve represents the cavity OLTF when the 10 kHz integrator has been enabled; the pink curve represents the cavity OLTF when the 1 kHz integrator has been enabled and the red curve represents the cavity OLTF when the 100 Hz integrator has been enabled.

Fig. 5.4, Fig. 5.5, Fig. 5.6 show the cavity OLTFs for the cavity and HDs, measured with the use of three servo integrators, with the green curve representing the OLTF when the 10 kHz integrator has been enabled, the pink curve representing the OLTF when the 1 kHz integrator has been enabled and the red curve representing the OLTF when the 100 Hz integrator has been enabled in each.

The unity gain frequency of the system loops can be set up to a maximum of 10 kHz. The control loops can therefore suppress unwanted disturbances up to this frequency. The challenge, however, is to set the unity gain frequencies of all the systems as low as possible, in order to avoid affecting the DN and GW transfer functions in the measurement bandwidth.

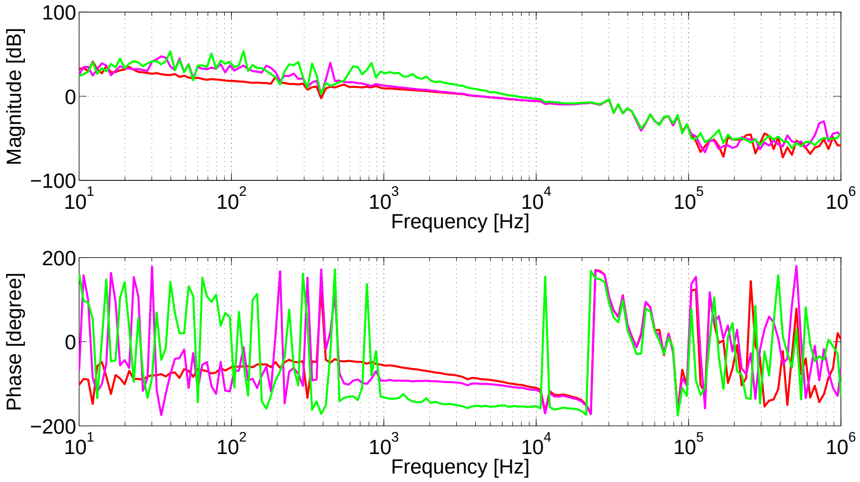

Figure 5.5.: The HD1 open loop transfer function (OLTF) measured with the use of three servo integrators. The green curve represents the HD1-OLTF when the 10 kHz integrator has been enabled; the pink curve represents the HD1-OLTF when the 1 kHz integrator has been enabled and the red curve represents the HD1-OLTF when the 100 Hz integrator has been enabled.

5.2.1. Cavity loop unity gain for DFI

Fig. 5.7 shows the cavity loop unity gain setting for the DFI measurements while the cavity is on its locking point of 12 MHz. The stability of the loop is described by the unity gain at around 90 Hz with a phase margin of $\approx 50°$. It has to be noticed that a phase margin of 60° is highly desirable in feedback system design. Typically, the minimum acceptable phase margin is 45°.

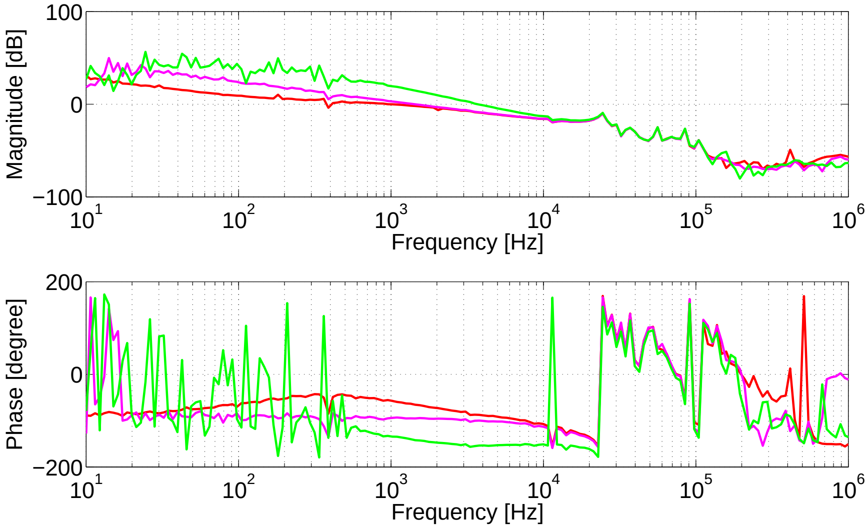

Figure 5.6.: The HD2 open loop transfer function (OLTF) measured with the use of three servo integrators. The green curve represents the HD2-OLTF when the 10 kHz integrator has been enabled; the pink curve represents the HD2-OLTF when the 1 kHz integrator has been enabled and the red curve represents the HD2-OLTF when the 100 Hz integrator has been enabled.

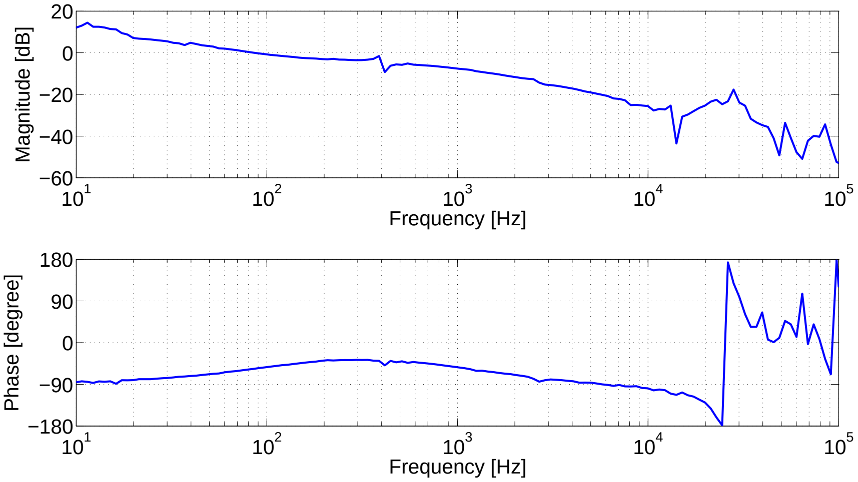

Figure 5.7.: Cavity loop unity gain for DFI. The stability of the loop is described by the unity gain at around 90 Hz with a phase margin of ≈ 50°.

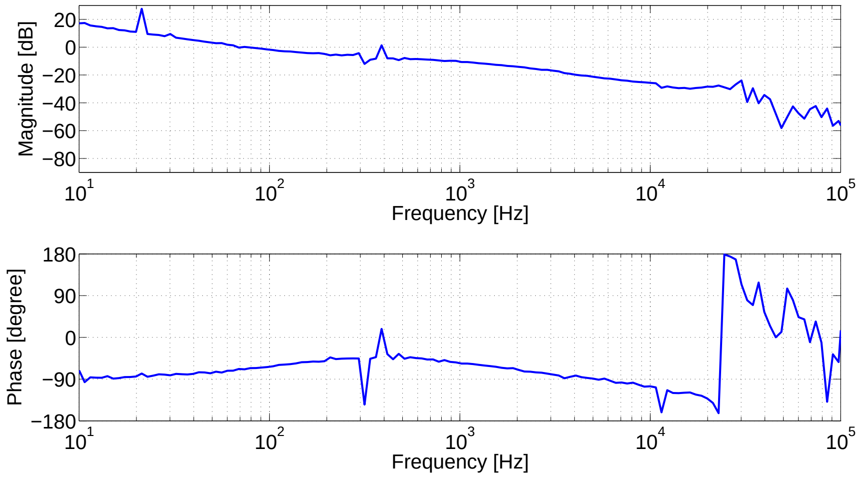

Figure 5.8.: Homodyne detector HD1 loop unity gain for DFI. The stability of the loop is described by the unity gain at around 70 Hz with a phase margin of ≈ 60°.

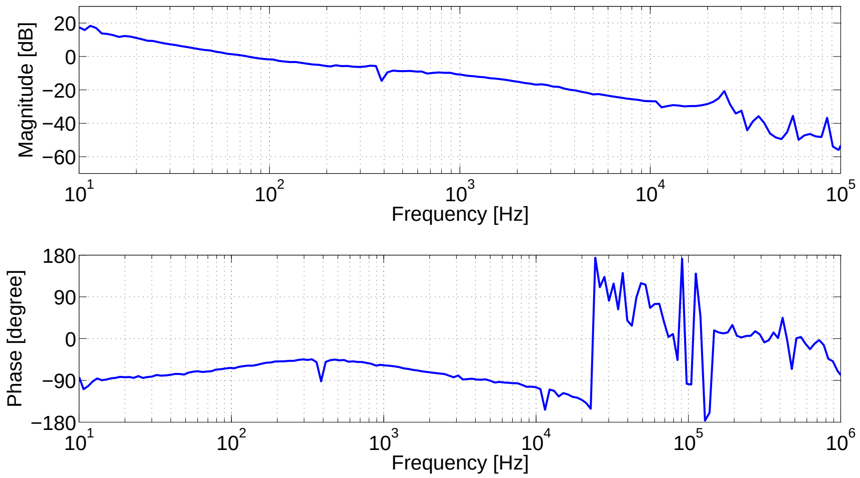

Figure 5.9.: Homodyne detector HD2 loop unity gain for DFI. The stability of the loop is described by the unity gain at around 70 Hz with a phase margin of ≈ 60°.

5.2.2. Homodyne detectors HD1 and HD2 loop unity gain for DFI

Fig. 5.8 and Fig. 5.9 show the homodyne detector HDs loop unity gain set for the DFI measurements. The cavity is still on its locking point of 12 MHz. The stability of the loop is described by the unity gain at around 70 Hz with a phase margin of $\approx 60^\circ$.

5.3. Preparation for the DFI measurement: Relaxation oscillation suppression

The homodyne detection described in Section 3.4.1 is a balanced homodyne detector provided by a 50/50 beam splitter and two equal photodetectors. In reality the beam splitter is not perfectly 50/50 and the two photodetectors are not perfectly equal. Subsequently for the homodyne detector shown in Fig. 3.15, if one of the two beams is dumped and the other contains a generic signal, the latter will be not cancelled at the output of the subtractor, which is the output of the homodyne detector.

This problem is solved by implementing an attenuator in one of the subtractor inputs, which allows the suppression of the highest photocurrent in the two homodyne photodectors by on amount that makes the two photocurrents perfectly equal and gives a zero signal at the homodyne output. The described procedure is a fundamental step to be followed for preparing the experiment for the DFI measurements, which can be affected by the unbalanced homodyne outputs.

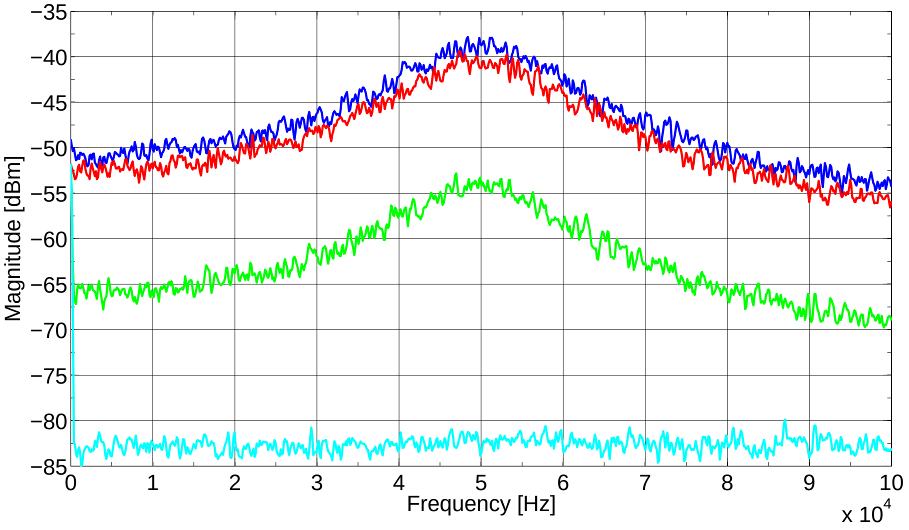

Figure 5.10.: The relaxation oscillation (RO) suppression on HD1 in the frequency domain. The blue curve is the output of the homodyne when only the photodetector PD1 is connected to the subtractor; The red curve is the output of the homodyne when only the photodetector PD2 is connected to the subtractor; the green curve is the output of the homodyne when both the photodetectors are connected to the subtractor with no use of the attenuator at the input of the subtractor; the cyan curve shows that the RO signal is completely suppressed when the attenuator at the subtractor input where the photodetector PD1 is connected, is enabled and appropriately tuned. (The same plots apply for the RO suppression on HD2 since the LO beam is the same in both homodyne detectors)

In particular for the homodyne HD1 the reflected light by the cavity is dumped and for the homodyne HD2 the transmitted light by the cavity is dumped, leaving only the LO in the two photodector outputs. The evaluation of a perfectly balanced homodyne is done in the current work by looking at the relaxation oscillation (RO) signal provided by the laser (introduced in Section 3.1.1). A perfectly balanced homodyne detector will suppress totally the RO signal present in each photodetector.

Fig. 5.10 shows the RO suppression on HD1 in the frequency domain (the same plots apply for the RO suppression on HD2 since the LO beam is the same in both homodyne detectors). The output of the homodyne detector shows a peak at around 50 kHz, measured by both photodetectors at different amplitudes. A subtraction of the two photodetector signals does not give a perfect cancelation of this peak, due to the difference in amplitudes of the two signals. With the use of an appropriately tuned attenuator on one of the subtractor inputs, however, a much more effective suppression of the 50 kHz peak is achieved. These measurements have been made using a spectrum analyser, manufactured by Agilent, which can measure only signals from 0 Hz to 100 kHz. Thus a mixer is used to display such measurements where the output of the subtractors is connected to the RF input of the mixer, a 20 kHz signal is connected to the other LO input of the mixer, and the IF output of the mixer is connected to the spectrum analyser. The displayed RO signal at 50 kHz corresponds to the real RO signal at 470 kHz.

5.4. DFI quadratures analysis at high frequency

The performances of the detuned FP-cavity DFI based scheme described in Section 5.5, show that suppression of the input cavity mirror has been achieved when both the homodyne detectors are in phase quadrature. On the other hand Section 4.4 showed how the simulated performances vary with the quadrature angle changes. Since the DN and GW responses depend on which quadratures the homodyne detectors are set, an analysis of the homodyne quadratures as it is shown in Section 4.4 is described here in order to provide qualitative information of the experimental performance at high frequency. The homodyne quadratures analysis provided in this Section is done by measuring the DN and the GW transfer functions at fixed frequency against the homodyne quadrature angles. The scanning of the quadratures starts when both the homodyne detectors are in phase quadrature. The entire cycle of the quadratures goes for tunings of both LOs from 0° to 180°. Tunings at 0° give both the homodyne detectors in phase quadratures, while tunings at 90° give both the homodyne detectors in amplitude quadrature.

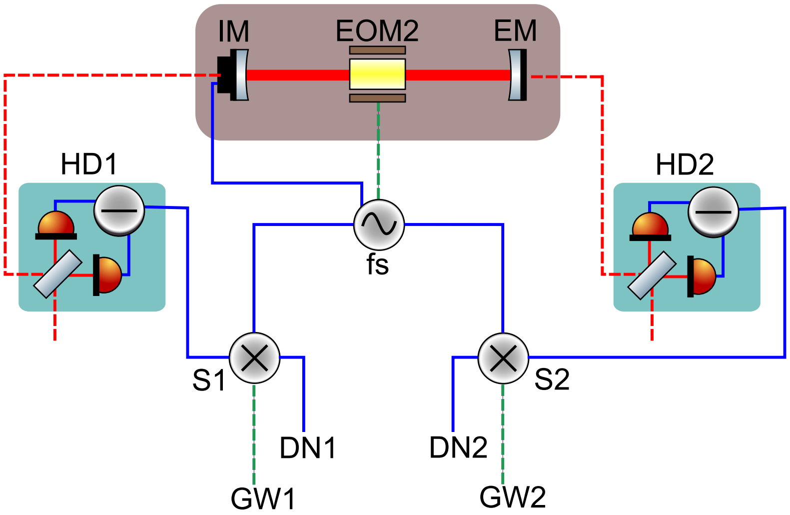

Figure 5.11.: DN and GW transfer functions measurement setup. The DN and GW transfer functions are obtained one after the other by injecting a sinusoidal signal at $f_s = 99.6\,\text{kHz}$ respectively in the PZT attached on the input cavity mirror and into the EOM2, while the cavity is locked in its 12 MHz detuned state. Successively the homodyne detector outputs are demodulated at f_s and then the time traces of DN (DN1, DN2) and GW (GW1, GW2) transfer functions at fixed frequency are evaluated.

The DN and GW transfer functions are obtained separately using a modulation-demodulation technique. A sinusoidal signal is injected at $f_s = 99.6\,\text{kHz}$ into the PZT attached to the cavity input mirror for the DN transfer function, and subsequently into EOM2 for the GW transfer function, all while the cavity is locked in the 12 MHz detuned state. In this way the time traces of DN (DN1, DN2) and GW (GW1, GW2) transfer functions at fixed frequency to HD1 and HD2 are

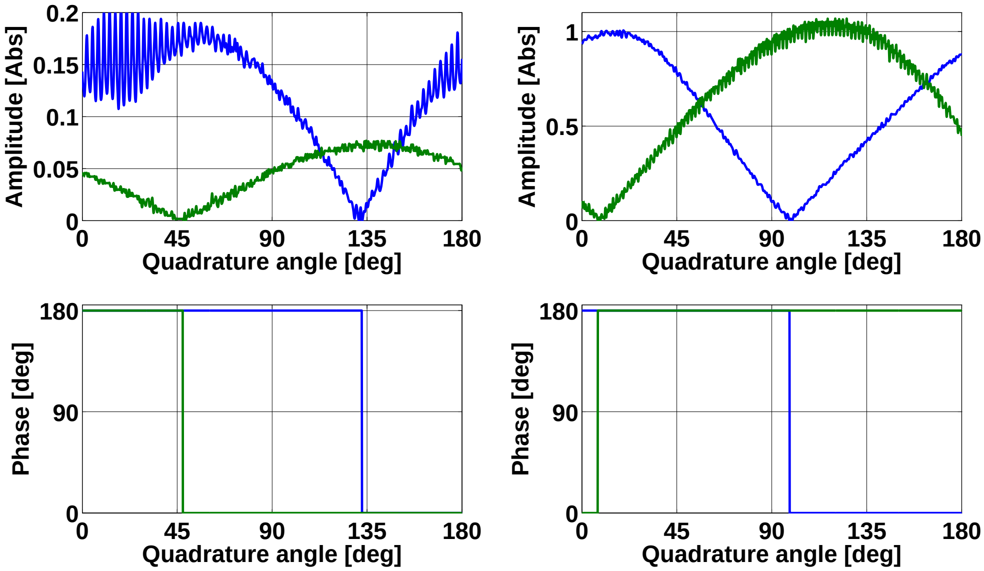

Figure 5.12.: DN and the GW transfer functions at fixed frequencies vs quadrature angle. The scanning of the quadratures starts when both the homodyne detectors are in phase quadrature. The left-hand side of shows the DN transfer functions from the input cavity mirror to HD1 (blue curve) and HD2 (green curve), ($S1_{\mathrm{DN}}$ and $S2_{\mathrm{DN}}$). The right-hand side shows the GW transfer functions from the cavity-length to HD1 (blue curve) and HD2 (green curve), ($S1_{\mathrm{GW}}$ and $S2_{\mathrm{GW}}$).

recorded. The DFI performances are evaluated from these measurements using the algorithm described in Section 4.3.

The modulation frequency f_s is chosen as the lowest possible as the cavity loses its locking state below this frequency.

The schematic diagram of such measurement is shown in Fig. 5.11.

Fig. 5.12 shows on the top the traces of DN and GW transfer functions after being calibrated against quadrature angles. Since the phases of DN and GW traces are not provided, in order to perform a qualitative analysis of the homodyne quadratures the phases of the transfer functions are simulated. Fig. 5.16 and Fig.5.17 show the phases of the DN transfer functions are the same while the GW transfer functions are 180° phase shifted, when both HD1 and HD2 are in phase quadrature. This relationship is used in Fig. 5.12 when the homodyne angles are at 0°. Successively a phase shift of 180° is imposed to the phases at each zero point of their relative amplitude transfer function.

The left-hand side of Fig. 5.12 shows the DN transfer functions from the input cavity mirror to HD1 (blue curve) and HD2 (green curve), respectively named $S1_{\mathrm{DN}}$ and $S2_{\mathrm{DN}}$. $S1_{\mathrm{DN}}$ has a minimum of zero at 130° while $S2_{\mathrm{DN}}$ has a minimum of zero at 46°. In between these two points the respective simulated phases are shifted by 180°. The right-hand side of Fig. 5.12 shows the GW transfer functions from the cavity-length to HD1 (blue curve) and HD2 (green curve), respectively named $S1_{\mathrm{GW}}$ and $S2_{\mathrm{GW}}$. $S1_{\mathrm{GW}}$ has a minimum of zero at 99° while $S2_{\mathrm{GW}}$ has a minimum of zero at 10°. In between these two points the respective simulated phases are the same. This quadrature analysis aims to identify quadrature angles at which DFI results show a relatively high improvement factor. For simplicity here the definitions of SNRs relative to both the processed and unprocessed data will be recalled and plotted in order to give more clarifications of some features of the improvement factor.

Fig. 5.13 shows the initial SNRs, σ_{S1} and σ_{S2}, of the unprocessed data in HD1 (left-hand side) and HD2 (right-hand side) respectively, defined as follows:

$$\begin{aligned}\sigma_{\mathrm{S1}} &= |S1_{\mathrm{GW}}|/|S1_{\mathrm{DN}}|,\\ \sigma_{\mathrm{S2}} &= |S2_{\mathrm{GW}}|/|S2_{\mathrm{DN}}|.\end{aligned} \tag{5.1}$$

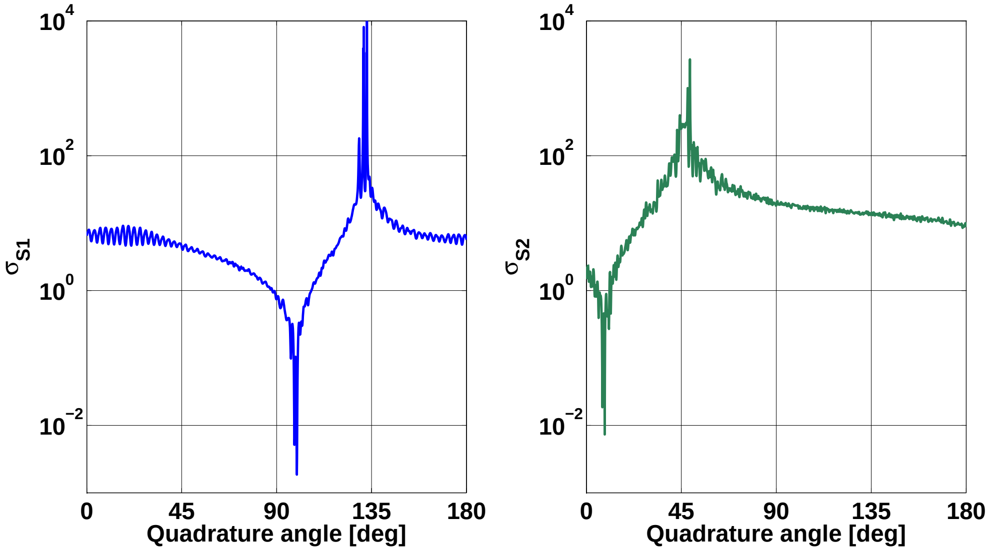

Figure 5.13.: SNRs of the unprocessed data vs quadrature angle. Tunings at 90° give both the homodynes detector in amplitude quadratures, while tunings at 0° give both the homodyne detectors in phase quadrature. On the left-hand side is plotted the SNR in HD1 (σ_{S1}). On the right-hand side is plotted the SNR in HD2 (σ_{S2}).

σ_{S1} has a peak at $\sim 130°$ and a minimum at $\sim 99°$, while σ_{S2} has a peak at $\sim 46°$ and a minimum at $\sim 10°$. The peaks are caused by the zero points of the absolute values of $S1_{\mathrm{DN}}$ and $S2_{\mathrm{DN}}$ whereas the dips are caused by the zero points of the absolute values of $S1_{\mathrm{GW}}$ and $S2_{\mathrm{GW}}$, as can be seen from Fig. 5.12 and from equations 5.1.

The detuned FP-cavity described in this work allows the construction of two new DFI data channels, as shown in Section 4.3. One is named DFI- with DN $S_{\mathrm{DN,DFI-}}$ and GW signal $S_{\mathrm{GW,DFI-}}$ as responses respectively to DN and GW signal, and one is named DFI+ with DN $S_{\mathrm{DN,DFI+}}$ and GW signal $S_{\mathrm{DN,DFI+}}$ as responses as well. The quadrature angles will determine the choice of the right DFI channel to be used for the achievement of an high DFI improvement factor. The two channels are defined as following:

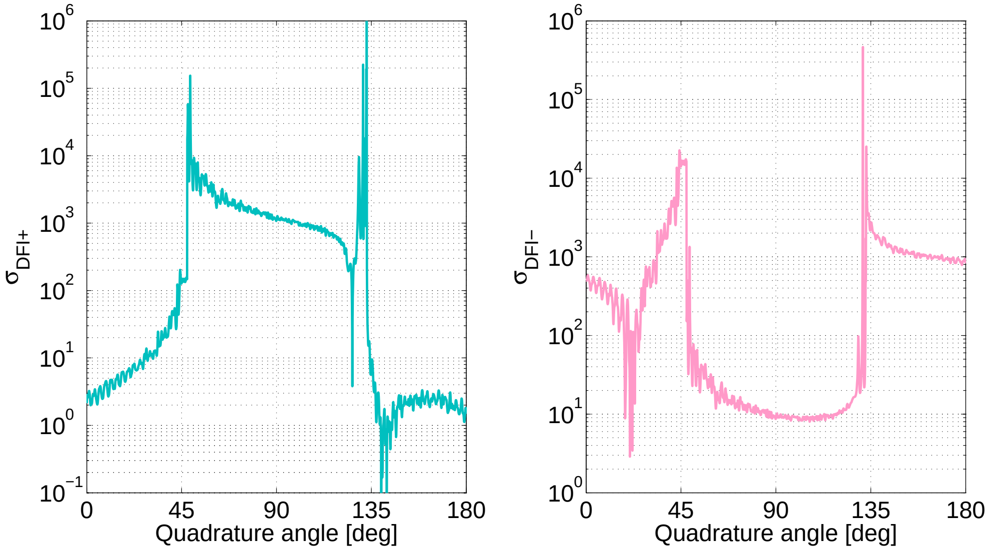

Figure 5.14.: SNRs of the DFI processed data. On the left-hand side the SNR of the DFI+ channel $\sigma_{\mathrm{DFI+}} = |S2_{\mathrm{GW,DFI+}}/S2_{\mathrm{DN,DFI+}}|$. On the right-hand side the SNR of the DFI- channel $\sigma_{\mathrm{DFI-}} = |S2_{\mathrm{GW,DFI-}}/S2_{\mathrm{DN,DFI-}}|$.

$$S_{\mathrm{DN,DFI-}} = S1_{\mathrm{DN}} - k \cdot S2_{\mathrm{DN}} \qquad S_{\mathrm{DN,DFI+}} = S1_{\mathrm{DN}} + k \cdot S2_{\mathrm{DN}} \tag{5.2}$$

$$S_{\mathrm{GW,DFI-}} = S1_{\mathrm{GW}} - k \cdot S2_{\mathrm{GW}} \qquad S_{\mathrm{GW,DFI+}} = S1_{\mathrm{GW}} + k \cdot S2_{\mathrm{GW}} \tag{5.3}$$

where k represents a scaling factor which minimises the DN content in channel $S_{\mathrm{DN,DFI-}}$ and $S_{\mathrm{DN,DFI+}}$ defined in any quadrature as $k = S1_{\mathrm{DN}}/S2_{\mathrm{DN}}$.

The Fig. 5.14 shows the SNRs of the DFI processed data. On the left-hand side the SNR of the DFI+ channel ($\sigma_{\mathrm{DFI+}}$). On the right-hand side the SNR of the DFI- channel, ($\sigma_{\mathrm{DFI-}}$) defined as

$$\sigma_{\mathrm{DFI-}} = |S_{\mathrm{GW,DFI-}}|/|S_{\mathrm{DN,DFI-}}| \tag{5.4}$$

$$\sigma_{\mathrm{DFI+}} = |S_{\mathrm{GW,DFI+}}|/|S_{\mathrm{DN,DFI+}}| \tag{5.5}$$

In between 46° and 130° $\sigma_{\mathrm{DFI+}}$ is relatively high varying from $\approx 10^2$ to $\approx 10^3$. In the complementary interval $\sigma_{\mathrm{DFI-}}$ shows relative high values varying from $\approx 10^2$ to $\approx 10^3$. Two peaks are shown in both plots at $\sim 46°$ and $\sim 130°$ caused by high values of k in points of zero of $S2_{\mathrm{DN}}$ and $S1_{\mathrm{DN}}$ respectively. In particular high values of k strongly enhance $|S_{\mathrm{GW,DFI-}}|$ and $|S_{\mathrm{GW,DFI+}}|$.

Shown in Fig. 5.15 is the enhancement effect ρ_i of the DFI defined as the ratio ρ_i between the processed and unprocessed SNRs:

$$\begin{aligned} &\rho_{\mathrm{S1+}} = \sigma_{\mathrm{DFI+}}/\sigma_{\mathrm{S1}} \qquad \rho_{\mathrm{S2+}} = \sigma_{\mathrm{DFI+}}/\sigma_{\mathrm{S2}} \\ &\rho_{\mathrm{S1-}} = \sigma_{\mathrm{DFI-}}/\sigma_{\mathrm{S1}} \qquad \rho_{\mathrm{S2-}} = \sigma_{\mathrm{DFI-}}/\sigma_{\mathrm{S2}} \end{aligned} \tag{5.6}$$

Present in Fig. 5.15 are peaks of $\rho_{\mathrm{S1+}}$ and $\rho_{\mathrm{S1-}}$ at $\sim 99°$. Looking at equation 5.6 and Fig. 5.13 it is possible to identify the dip of σ_{S1} as the reason of such peaks; in the same way the dip of σ_{S2} causes peaks of $\rho_{\mathrm{S2+}}$ and $\rho_{\mathrm{S2-}}$ at $\sim 10°$. Other peaks of $\rho_{\mathrm{S1+}}$ and $\rho_{\mathrm{S1-}}$ are at $\sim 46°$. Recalling that at this point k is extremely high and causes an high enhancement of $|S_{\mathrm{GW,DFI-}}|$ and $|S_{\mathrm{GW,DFI+}}|$, $\rho_{\mathrm{S1+}}$ and $\rho_{\mathrm{S1-}}$ are enhanced as consequence as well. It can be noticed that such peaks are not found in $\rho_{\mathrm{S2+}}$ and $\rho_{\mathrm{S2-}}$ since the high value of σ_{S2} at $\sim 46°$ limits the enhancement to HD2, as can be seen from Fig. 5.14 and equations 5.4 and 5.6. Conversely $\rho_{\mathrm{S2+}}$ and $\rho_{\mathrm{S2-}}$ have peaks at 130°, caused by high value of $|S_{\mathrm{GW,DFI-}}|$ and $|S_{\mathrm{GW,DFI+}}|$, that

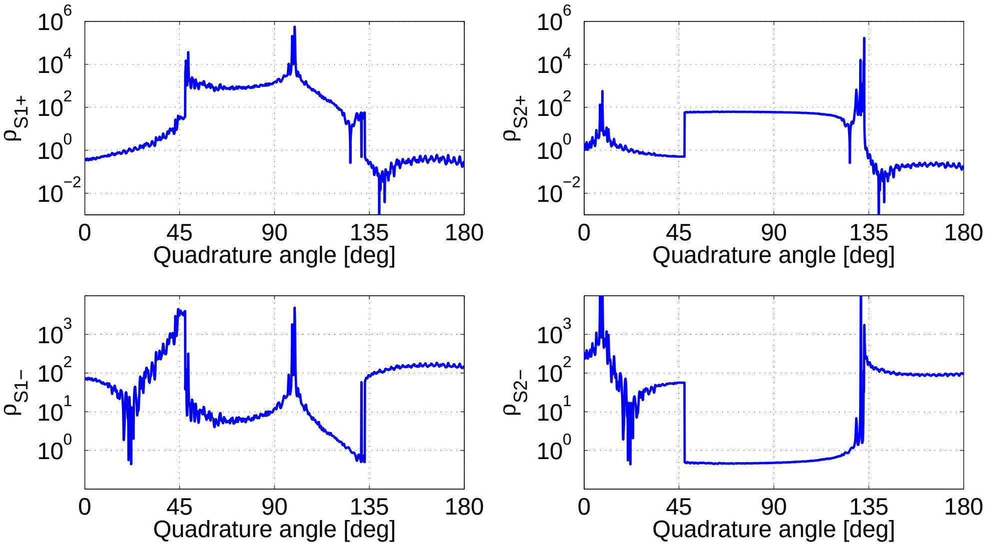

Figure 5.15.: Enhancement effect of the DFI. The ratio ρ_i between the processed and unprocessed SNRs against the quadrature angles are evaluated. The plots are organised as follows: On the top-left-hand side $\rho_{\mathrm{S1+}} = \sigma_{\mathrm{DFI+}}/\sigma_{\mathrm{S1}}$. On the top-right-hand side $\rho_{\mathrm{S2+}} = \sigma_{\mathrm{DFI+}}/\sigma_{\mathrm{S2}}$. On the bottom-left-hand side $\rho_{\mathrm{S1-}} = \sigma_{\mathrm{DFI-}}/\sigma_{\mathrm{S1}}$. On the bottom-right-hand side $\rho_{\mathrm{S2-}} = \sigma_{\mathrm{DFI-}}/\sigma_{\mathrm{S2}}$.

cannot be seen in the enhancement to HD1 since, in this case, σ_{S1} has an extremely high value in such point. The peak features described so far will be not taken into account for a qualitative analysis of homodyne quadratures (see Section 4.4). It is mostly interesting to localise on area where obtained an appreciable SNR can be, where locking the two homodynes detectors could be experimentally possible.

In Fig. 5.15 a relatively high enhancement effect of $\rho_{\mathrm{S1+}}$ varying from $\approx 10^2$ to $\approx 10^3$ can be seen in the region between 46° and 130°. In the same region $\rho_{\mathrm{S2+}}$ shows a relatively high enhancement effect of ≈ 90. On the other hand in the complementary region $\rho_{\mathrm{S1-}}$ and $\rho_{\mathrm{S2-}}$ show an enhancement effect of ≈ 100.

Thus the quadrature analysis at high frequency shows an appreciable improvement factor can be achieved in DFI+ channel for quadrature angles of both HD1 and

HD2 in between 46° and 130°, i.e. when both the homodyne detectors are in amplitude quadratures. On the other hand, in the complementary angles interval, high improvement factor can be achieved in the DFI- channel, i.e when both the homodyne detectors are in phase quadrature as it is done for the DFI measurement shown in Section 5.5.

5.5. DFI responses and results

The aim of the DFI measurements, described in Section 5.1, is to obtain DN of the input cavity mirror and the GW responses to both the homodyne detectors, which represent two channels of the detuned FP-cavity based DFI scheme. As previously described these two channels can be used to create a new channel which is free from displacement noise. The new channel can be created as described in Section 4.3. The challenge is to prove the principle of the idea proposed in [TV08], giving a demonstration of DFI at low frequency. Thus the DN and simulated-GW responses are measured in the frequency range [10 Hz-100 kHz] as shown respectively in Fig. 5.16 and Fig. 5.17.

Since the DFI responses, and then the experimental proof, of the detuned FP-cavity setup shown in this thesis depend on the particular quadrature, the two homodyne detectors are provided with two control loops to ensure that their locking point is in the so called phase quadrature. These responses are measured one after the other while the cavity is in its locking point at 12 MHz. The cavity and homodyne detectors loop unity gain is shown in sections 5.2.1 and 5.2.2.

As one can see in Fig. 5.16 the two transfer functions for the displacement noise from

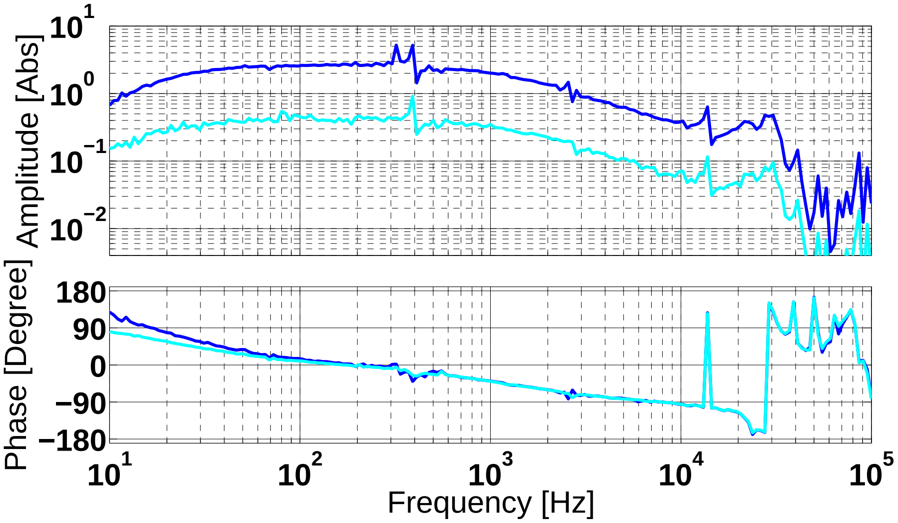

Figure 5.16.: Comparison of the measured transfer functions with the two homodyne detectors HD1 and HD2. The two displacement noise transfer functions are represented by the blue and cyan curves measured respectively in HD1 and HD2. One can see that the two displacement noise transfer functions are in phase almost in the whole frequency range.

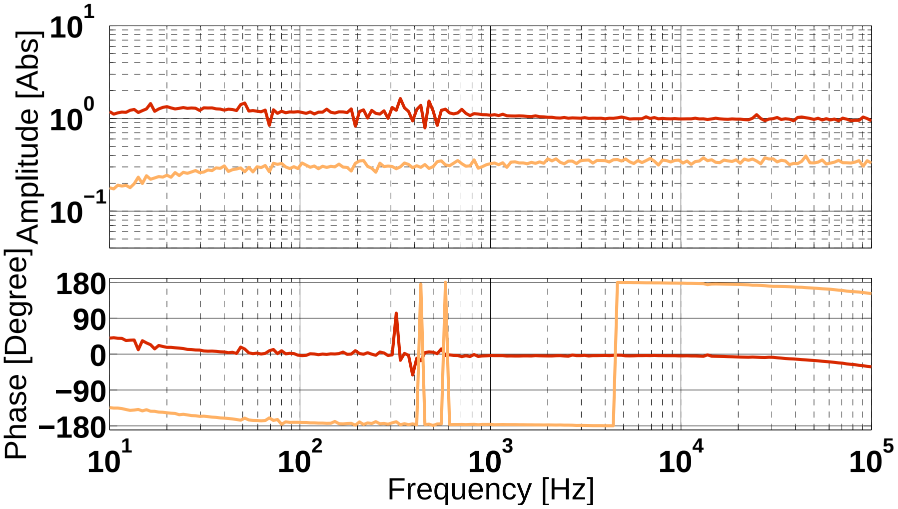

Figure 5.17.: Comparison of the measured transfer functions with the two homodyne detectors HD1 and HD2. The two simulated gravitational wave transfer functions are represented by the red and orange curves respectively measured in HD1 and HD2. One can see that the two simulated GW signal transfer functions have a relative phase shift of 180° to each other in the whole frequency range.

the cavity input mirror IM to the two homodyne detectors $S1_{\mathrm{DN}}$ (blue curve) and $S2_{\mathrm{DN}}$ (cyan curve) are in phase in almost the entire frequency range. On the other hand the two GW signal transfer functions shown in Fig. 5.17, $S1_{\mathrm{GW}}$ (red curve) and $S2_{\mathrm{GW}}$ (orange curve), are out of phase by 180°. All of these transfer functions include phase shifts induced by the optical elements ($\phi_{\mathrm{S1}}, \phi_{\mathrm{S2}}$) that the reflected and transmitted light from the cavity passes before the detection in the homodyne detectors $S1$ and $S2$ respectively. The decreasing magnitude of all transfer functions towards low frequencies is a result of the cavity servo loop gain which increases at low frequencies thereby suppressing the injected signals more strongly.

The fact that the GW and DN transfer functions have different phase relations can be used to create a new DFI data channel where the GW content is maintained while the DN content will be strongly suppressed. This new data channel, as shown in Section 4.3, is given by:

$$
\begin{aligned}
S_{\mathrm{DN,DFI}} &= S1_{\mathrm{DN}} - k \cdot S2_{\mathrm{DN}}, && (5.7)\\
S_{\mathrm{GW,DFI}} &= S1_{\mathrm{GW}} - k \cdot S2_{\mathrm{GW}}. && (5.8)
\end{aligned}
$$

here k represents a fixed scaling factor which minimises the DN content in channel $S_{\mathrm{DN,DFI}}$. In this case k was arbitrarily chosen to be the ratio of the DN transfer function magnitude at 50 Hz ($k = S1_{\mathrm{DN_A}}[50\,\mathrm{Hz}]/S2_{\mathrm{DN_A}}[50\,\mathrm{Hz}]$), as changing the frequency for determining k does not dramatically change the results.

The signal-to-noise ratios (SNRs) σ of the initial unprocessed data channels of $S1$ and $S2$ are given by

$$\begin{aligned} \sigma_{\mathrm{S1}} &= S1_{\mathrm{GW}}/S1_{\mathrm{DN}}, \qquad (5.9) \\ \sigma_{\mathrm{S2}} &= S2_{\mathrm{GW}}/S2_{\mathrm{DN}} \qquad (5.10) \end{aligned}$$

and show how well a GW can be detected with respect to the present DN. For the processed data channels a similar SNR can be calculated as:

$$\sigma_{\mathrm{DFI}} = S_{\mathrm{GW,DFI}}/S_{\mathrm{DN,DFI}} \qquad (5.11)$$

To see the enhancement effect of the DFI in this experiment Figure 5.18 shows the ratios ρ_i between the processed and unprocessed SNRs as follows:

$$\begin{aligned} \rho_{\mathrm{S1}} &= \sigma_{\mathrm{DFI}}/\sigma_{\mathrm{S1}}, \qquad (5.12) \\ \rho_{\mathrm{S2}} &= \sigma_{\mathrm{DFI}}/\sigma_{\mathrm{S2}} \qquad (5.13) \end{aligned}$$

respectively as the blue and red curves.

The improvement in the ratios ρ_i of the processed and unprocessed SNRs is significant in the frequency range of interest. Overall ρ_{S1} performs a little bit better than ρ_{S2}. At 10 Hz one can see an improvement in ρ_i of approximately two. This value increases almost linearly up to 250 Hz where it reaches a factor of about a hundred. In the whole frequency range of interest the typical gain is ~ 60 [PCHF10].

The DFI toy model described in [TV08] provides a perfect cancelation of displacement noise from the input cavity mirror, which corresponds to an infinite

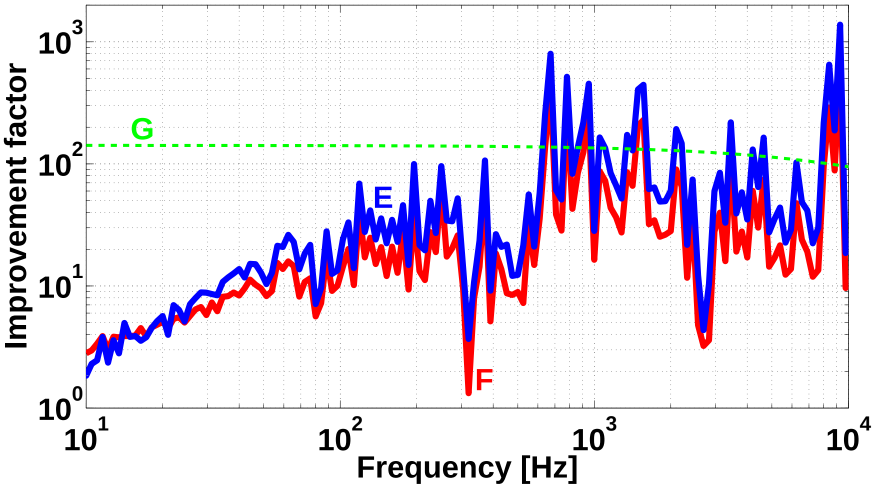

Figure 5.18.: The improvement due to the DFI scheme is expressed by the ratio ρ_i between the processed SNR σ_{DFI} and unprocessed SNRs σ_{S1} and σ_{S2}. The two resulting ratios $\rho_{\mathrm{S1}} = \sigma_{\mathrm{DFI}}/\sigma_{\mathrm{S1}}$ (blue curve) and $\rho_{\mathrm{S2}} = \sigma_{\mathrm{DFI}}/\sigma_{\mathrm{S2}}$ (red curve) show an improvement in the whole frequency range with a slight advantage for ρ_{S1} compared to ρ_{S2}. Trace G shows the expected result for a phase difference between the transfer functions of the two homodyne detectors of $\phi = 1°$, which reduces the maximally achievable DN reduction factor to ~ 140.

SNR. Although a theoretical description of this experiment using ideal components predicts perfect cancelation a more realistic improvement factors must be computed including inevitable asymmetries in the experimental setup. If the transfer functions in Fig. 5.16 show a phase difference ϕ the expected improvement factor can be expressed as $|\alpha/(e^{i\phi} - 1)|$ where $\alpha = |S_{\mathrm{GW,DFI}}|/|S1_{\mathrm{GW}}|$ for HD1 and $\alpha = |S_{\mathrm{GW,DFI}}| \cdot k/|S2_{\mathrm{GW}}|$ for HD2. In particular when $\phi = 0.1°$ the expected improvement factor is ~ 1500 (see Section 4.5.3), whereas a phase difference of $\phi = 1°$ reduces the improvement factor to ~ 140 resulting in trace G shown in Fig. 5.18. As one can see the overall DN reduction level of trace G corresponds quite well with the experimental result at high frequencies.

In addition to this frequency independent phase difference, which was expected from an imperfect setup of the homodyne detectors, one could also identify a frequency dependent asymmetry. This originates from slight differences in the feedback control electronics which lead to different slopes in the phase behaviour at low frequencies. In more detail, the traces in Fig. 5.16 have relatively high phase difference at low frequencies which decreases up to $\sim 100\,\text{Hz}$ while the corresponding amplitudes have flat shapes starting from $\sim 70\,\text{Hz}$. Less dominant but still present, this effect is visible in the traces of Fig. 5.17. Due to this frequency dependent phase difference the resulting DN rejection factor decreases towards low frequencies and does not follow the expected behaviour shown by trace G.

Furthermore, this type of table-top experiment is subject to mechanical vibrations of optics mounts which create sharp dispersion-like structures in the DN and GW transfer functions at frequencies between 200 Hz and 4 kHz. The phase asymmetries mentioned above convert such dispersion structures in peaks or dips in the improvement factor.

Chapter 6.

Conclusions

This thesis presents the first experimental proof of principle of the detuned Fabry-Perot (FP)-cavity based Displacement noise-Free Interferometry (DFI) scheme showing a large enhancement of a mimicked gravitational wave (GW) signal compared to the displacement noise (DN) in the gravitational frequency band from 10 Hz-10 kHz. Here the suppression of DN from the input cavity mirror is considered. The success of the experiment is represented by an improvement in the GW signal to DN ratio by a factor of 60 over the whole frequency range of interest. The experiment uses a laser to pump the FP-cavity from the input cavity mirror and uses the reflected and the transmitted light from the cavity as multiple channels, with each channel sensed by one of two homodyne detectors. The linear combination of the two homodyne detectors is used to form a DFI channel which is free from any kind of displacement noise. The experiment was simulated before its physical construction in order to support the validity of the setup by providing an expected improvement factor, which was close to the one obtained from the real experiment. Furthermore the simulation gives the possibility to optimise and analyse several possible options for the homodyne settings. In particular two DFI channels are evaluated against the quadrature angles, giving useful information for future experiments that might use this scheme. A similar description is provided in the last part of this thesis for an analysis at high frequency of the quadrature angles which gives general information on the behaviour of real experiments. This analysis shows for any angle which DFI channel one has to choose to obtain the DN suppression, confirming the success of the experiment presented.

This thesis strictly enters in the challenging (and strongly debated) contest aiming to improve the sensitivity of GW detectors. Indeed, the surprising DFI technique this thesis is dealing with was proposed a few years ago by Y. Chen and S. Kawamura, and it was straightforward to see how important this method could have been for the third generation of GW detectors. In particular this technique uses multiple readouts from the experiment, which allows the construction of an observable (here called DFI channel), which is free from any kind of DN whilst retaining the GW signal.

In order to reach the first GW detection, ground based detectors need to improve their sensitivity, especially in the low frequency band. Recalling that the noise-sources limiting the sensitivity of GW detectors at low frequency are DNs, with all the efforts that scientists are making to attenuate each of these DNs individually, it can clearly be seen how enchanting a single technique capable of completely removing all kinds of DNs at once appeared.

Unfortunately the DFI based on the Chen-Kawamura concept is only able to suppress noises at high frequencies, which are not the GW frequency band of interest. They initially proposed a 2-dimensional experiment, later extended to a 3-dimensional one, using a Mach-Zender configured interferometer where DNs were suppressed from both mirrors and beam-splitters, again at frequencies above 1 MHz. Although the frequency range was not of direct interest, the technique was demonstrated with very encouraging results which stimulated researchers to study new DFI configurations able to improve the DFI performances at low frequency.

Thus a further step was proposed by S. P. Tarabrin and S. P. Vyatchanin in 2008 with a new DFI scheme. Although it does not include the frequency noise aspect of DFI, it is an interesting toy-model using the features of a FP-cavity to suppress DN from both the cavity mirrors in the low frequency regime. Here the mechanism of noise cancelation gives better results than Chen-Kawamura's responses. In the long wave approximation $\lambda_{gw} \gg L$, where λ_{gw} is the GW wavelength and L is the cavity length, the leading order of the DFI signal for the FP-cavity is $h(L/\lambda_{gw})^0$ while $h(L/\lambda_{gw})^2$ is the response obtained from the Chen-Kawamura DFI scheme. As a drawback the FP-cavity scheme loses the optical resonant gain from the cavity. Consequently, the sensitivity of this scheme concerning GWs is reduced compared to conventional interferometers and the noise performance of auxiliary optics becomes more important. Currently this is the limit for the implementation in GW detectors. Reducing the noise of the auxiliary optics, for example by using very heavy cooled platforms where some fraction of them can be mounted, will attenuate this limit somewhat.

As part of the work for this thesis a new interesting interferometer topology formed by three coplanar Michelsons in a triangular geometry. This has been introduced and studied as a possible option to be considered for the third generation of GW detectors. This configuration, provided with resonant arm cavities, power recycling and tunable signal recycling cavities, can be seen as one of the possible starting point for implementing the FP-cavity DFI based scheme where the arm cavities can be pumped from both sides in order to remove DN from the cavity mirrors. This is an almost completely unexplored configuration deserving of further study. Future research based on the promising results of this thesis could investigate the feasibility of such platforms.

A further DFI technique has been already proposed for a two aligned FP-cavity configuration by A. A. Rakhubovsky and S. P. Vyatchanin where they have shown suppression from all the cavity mirrors, with a DN response better than the one obtained by Y. Chen and S. Kawamura.

This thesis was designed to prove the underlying idea of many new schemes represented by the toy-model originally proposed by S. P. Tarabrin and S. P. Vyatchanin. It represents the first experimental demonstration of the new proposed detuned FP-cavity DFI scheme showing improvement of GW-signal to DN ratio of a typical factor of 60 in the GW detector band and opening up the possibility for future work aimed at implementations in up-coming laser interferometers.

Appendix A.

Advanced Virgo: Length sensing and control system

A.1. Introduction

The development of the design of advanced detectors requires further investigation for an optimal choice of their parameters. In particular here an area of a work done for Advanced Virgo is presented. This is an extract from a document delivered to the Virgo community [HMPF09], aimed to design the length sensing and control system (LSCS). This work has been done following the Advanced LIGO approach described in [AAB$^+$08].

The design of Advanced Virgo, which is still under study, will affect the LSCS. Currently, since many parameters for the design have not been decided yet, the LSCS cannot be properly optimised. This can be done only after the design is provided. On the other hand LSCS sets constraints for other systems, i.e. the recycling cavity, which in turn affect the detector performances. Thus the idea is to create an automatised tool able to provide an optimal LSCS under any given constraints rather than the usual calculations and simulations, allowing the LSCS to be checked and optimised during any changes of the detector design. This means that for any change in the detector design the LSCS is able to provide new constraints for other systems giving the possibility to evaluate the optimal detector configuration, i.e. finding the optimal modulation frequencies, as well as the detector performances.

This goal is achieved with a set of tools called OSD_Tools, a set of Matlab functions making use of Finesse software, described in more detail in [HMPF09]. Here a qualitative procedure using such tools to create the optimal detector configuration for a given set of input parameters and constraints is presented.

A.2. Definition of lengths

Before giving a description of the use of tools it is worth defining the length and tunings. The former represents the distance between two optical elements measured to an accuracy of $\sim 1\,\mathrm{mm}$, here indicated by $\mathrm{L_i}$, the latter represents a microscopic distance. Therefore distances between optical elements can be represented by lengths and tunings. Fig. A.1 shows a simplified optical layout of the Advanced Virgo interferometer, where the main lengths are shown. Details of the definition of lengths are shown in A.1.

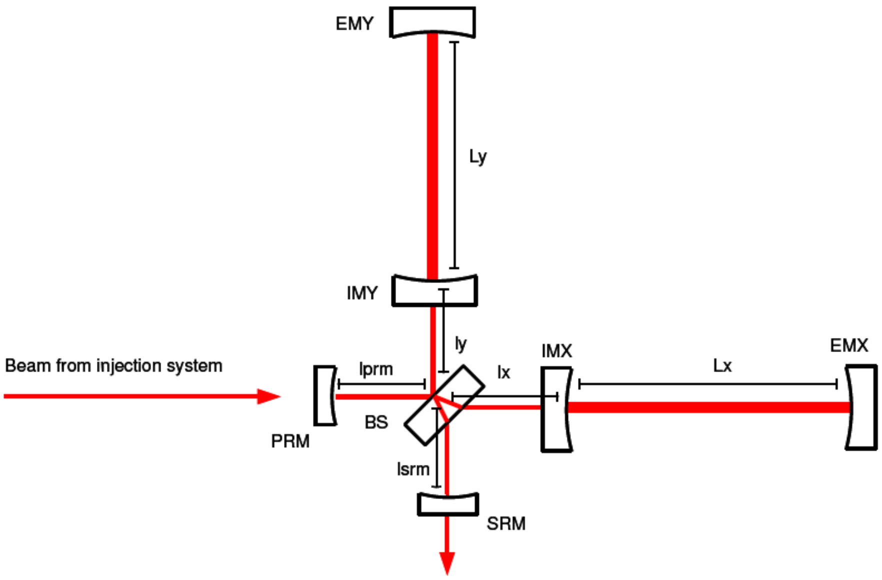

Figure A.1.: Advanced Virgo optical layout. It is a Michelson interferometer with arm cavities and recycling cavities [HMPF09].

Name	Description
lprm	length between PRM HR coating and BS HR coating
lx	length between BS HR coating and IMX HR coating (includes BS and IMX substrates)
ly	length between BS HR coating and IMY HR coating (includes IMY substrate)
Lx	length between IMX HR coating and EMX HR coating
Ly	length between IMY HR coating and EMY HR coating
lsrm	length between BS HR coating and SRM HR coating (includes BS substrate)

Table A.1.: Definition of the lengths inside the Advanced Virgo interferometer [HMPF09]. The defined distances take into account the high reflectivity (HR) coating of the optical elements.

Schnupp length

In order to detect the radio frequency modulation sidebands at the output port of the interferometer lx and ly must have a macroscopic length difference. This is then defined as Schnupp asymmetry (or Schnupp length) in the following form:

$$L_{\text{Sch}} = \frac{\text{lx} - \text{ly}}{2} \tag{A.1}$$

Length of the Power-Recycling cavity

The length of the Power-Recycling cavity (PRC) is defined as:

$$L_{\text{PRC}} = \text{lprm} + \frac{\text{lx} + \text{ly}}{2} \tag{A.2}$$

Length of the Signal-Recycling cavity

The length of the Signal-Recycling cavity (SRC) is:

$$L_{\text{SRC}} = \text{lsrm} + \frac{\text{lx} + \text{ly}}{2} \tag{A.3}$$

Definition of Degrees of Freedom (DOF)

The following five degrees of freedom are used to describe the full core of the interferometer:

$$\begin{aligned}
\phi_{\mathrm{DARM}} &= \frac{\mathrm{Lx}-\mathrm{Ly}}{2} && \text{(A.4)}\\
\phi_{\mathrm{CARM}} &= \frac{\mathrm{Lx}+\mathrm{Ly}}{2} && \text{(A.5)}\\
\phi_{\mathrm{MICH}} &= \frac{\mathrm{lx}-\mathrm{ly}}{2} && \text{(A.6)}\\
\phi_{\mathrm{PRCL}} &= \mathrm{lprm}+\frac{\mathrm{lx}+\mathrm{ly}}{2} && \text{(A.7)}\\
\phi_{\mathrm{SRCL}} &= \mathrm{lsrm}+\frac{\mathrm{lx}+\mathrm{ly}}{2} && \text{(A.8)}\\
& && \text{(A.9)}
\end{aligned}$$

It should be mentioned that the degrees of freedom concern microscopic lengths.

A.3. Optimisation of detector configuration

The optimisation of the detector configuration is based on the work presented in [AAB^{+}08], with a set of Matlab functions, OSD_Tools, used to interface and automate the calculation of the simulated interferometer parameters encoded in Finesse software. The optimisation is performed in the following order:

1. Radii of curvature of the mirrors (ROC)
2. RF-modulation frequencies
3. Length of Power-Recycling cavity (PRC)

4. Schnupp Asymmetry
5. Length of Signal-Recycling cavity (SRC)

A.3.1. Calculating the radius of curvature for a given beam size

Matlab function which uses OSD_tools (OSD_ROC.m) has been created in order to calculate the ROC of the main arm cavity mirrors IMx, EMx, IMy, EMy and the two recycling mirrors PRM and SRM. This function takes the desired beam radius as an input, and as additional input a Finesse file is used to simulate the whole interferometer. As the first step the function runs Finesse to calculate the ROCs of the main cavity mirrors at a given beam radius. Afterwards it scans the length L of ROC from $L+1$ to $L-1$ and then extracts the closest value to the desired radius of curvature. Then a second simulation is performed for calculating the ROCs of the two recycling mirrors PRM and SRM.

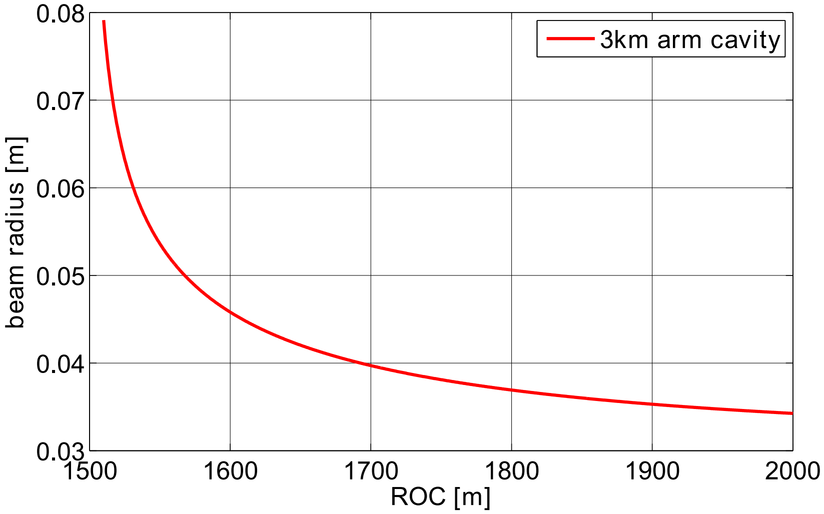

Figure A.2.: Beam radius versus radius of curvature (ROC). [HMPF09].

In particular the curvature of the wavefront at the position of the recycling mirror,

i, has been calculated using the distance from the waist, z, and the Rayleigh range, z_r as follows:

$$R_{c,i} = z_i + \frac{z_{r,i}^2}{z_i} \tag{A.10}$$

The optimised values for the ROCs are finally saved into a Finesse output file. Fig. A.2 shows the beam radius of the test masses as a function of ROCs.

A.3.2. Calculating the RF modulation frequencies

Following the Advanced LIGO approach, Advanced Virgo uses two radio frequency (RF) modulations which have to be detected at the output of the detector. The design strategy is to keep both RFs, f_1 and f_2, simultaneously resonant in the PRC in order to be enhanced, and not resonant in the arm cavities, together with the first six higher order modes (TEM$_{lm}$ with $l + m \leq 6$), to avoid decoupling effects with the various length degrees of freedom. The first item can be realized choosing f_1 to be at the first FSR and f_2 to be a multiple of the first modulation frequency:

$$f_2 = M \cdot f_1 \qquad \text{with} \quad M \in \mathbb{N} \tag{A.11}$$

Note that a large M is required from one side for a better decoupling of f_1 and f_2, and a small M is required from the other side for a simpler feasibility of RF electronics.

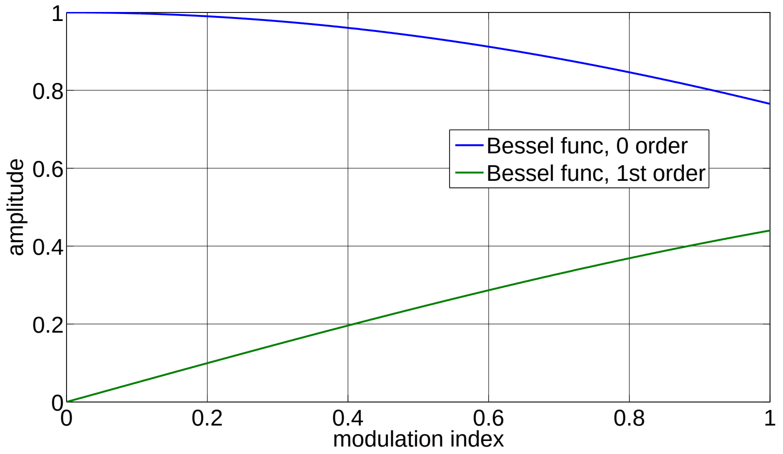

Figure A.3.: Fundamental and 1st order Bessel functions. The first order Bessel function contains a fraction of the modulation which become more significant at higher modulation index [HMPF09].

It should also be observed that for a certain modulation index the first order Bessel function has a significant contribution. For example, Fig. A.3 shows the amplitude of the fundamental and first order Bessel functions versus modulation index. Here for a modulation index of 0.3 the first order Bessel function contains more than 10 % of the modulation. For this reason, concerning the second item, it is required that the first harmonic of the modulation frequencies ($2 \cdot f_1$ and $2 \cdot f_2$) together with their first six higher order optical modes have to be off resonant in the arm cavities. In other words, the two modulation frequencies must not be at the anti-resonance of the arm cavity.

To achieve this a Matlab function (OSD_modfreq.m) was created. 28 frequencies, consisting of the modulation sidebands $+f_1$, $-f_1$, $+f_2$ and $-f_2$, their first order harmonics and their first six higher order modes, are computed. The frequency

$f_{i,l+m}$ of the TEM$_{lm}$ of the modulation sideband f_i is expressed as follows:

$$f_{i,l+m} = f_i + f_{\text{sep},l+m}, \tag{A.12}$$

where $f_{\text{sep},l+m}$ is the transversal mode spacing of the optical mode of the order $l+m$, which is computed as:

$$f_{\text{sep},l+m} = (l+m) \times \frac{c}{2\pi L} \arccos \sqrt{(1 - \frac{L}{\text{ROC}_\text{I}})(1 - \frac{L}{\text{ROC}_\text{E}})}, \tag{A.13}$$

with L being the length of the arm cavity and ROC_I and ROC_E being the radius of curvature of the input cavity mirrors and the end cavity mirrors respectively.

Afterwards the frequency distances $\Delta_{i,l+m}$ and $\Delta_{i,l+m}$ from the resonance and from the anti-resonance of the arm cavities respectively, are calculated as follow:

$$\begin{aligned}\Delta_{i,l+m}(f) &= k \cdot \text{FSR} - f_{i,l,m}(f), && \text{(A.14)}\\ \Gamma_{i,l+m}(f) &= (k + \frac{1}{2}) \cdot \text{FSR} - f_{i,l+m}(f) && \text{(A.15)}\end{aligned}$$

where $FSR = c/(2 \cdot L)$ is the free spectral range of the arm cavities and k is an integer number describing the free spectral range closest to $f_{i,l+m}$.

Fig. A.4 shows a qualitative resonance condition of the modulation sidebands inside the arm cavity. The blue curve is the power enhancement of the fundamental order of the carrier inside the cavity, where the two peaks represent the resonances separated by one FSR, whereas the middle represents the anti-resonance frequency. The vertical dashed lines represent one modulation sideband and its higher order modes equally separated. An example of the distance from resonance and anti-resonance is indicated for the 4th higher order mode (yellow line).

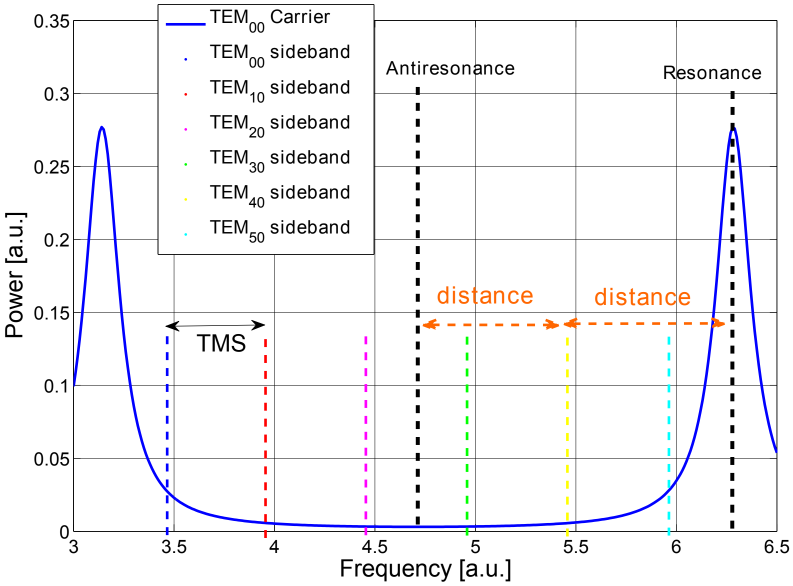

Figure A.4.: Resonance condition of the modulation sidebands inside the arm cavity [HMPF09].

Finally the minimal distance ($\Lambda(f)$) out of the 56 distance values are calculated for each of the modulation frequencies scanned over a given frequency range. The latter is given as an input to the function together with a Finesse file used to simulate the detector and the integer number M introduced in equation A.11 is given as well. The optimised modulation frequency is given by the one providing the largest value of $\Lambda(f)$.

A.4. Calculating the length of the Power-Recycling cavity (PRC)

The calculation of the length of the PRC has to be done taking into account that the RFs f_1 and f_2 have to be resonant inside the cavity. Given that f_2 is chosen as an integer multiple of f_1, once f_1 is resonant into the cavity, f_2 will be resonant as well. Thus the resonance condition is expressed as:

$$L_{\mathrm{PRC}} = (N + 0.5)\frac{c}{2f_1} \tag{A.16}$$

where N represents the unknown to be determined. The length of the PRC is calculated by the OSD-Tool function (OSD_PRC_length.m), which takes the input to be the desired rough length of the PRC. The function determines the optimal value for N following equation A.16 and writes this new value into a Finesse file in order to run a new simulation of the optical detector with the new optimised value of the length of the PRC. Using the new simulation, the optimal ROC of the PRM for the new length of the PRC is performed.

A.4.1. Calculating the Schnupp asymmetry and the length of the Signal-Recycling cavity

The last step for a new detector configuration obtained with an automated process is to optimise the Schnupp asymmetry L_{Sch} and the length L_{SRC} of the Signal-Recycling cavity (SRC) already defined in Section A.2. To this purpose it is re-

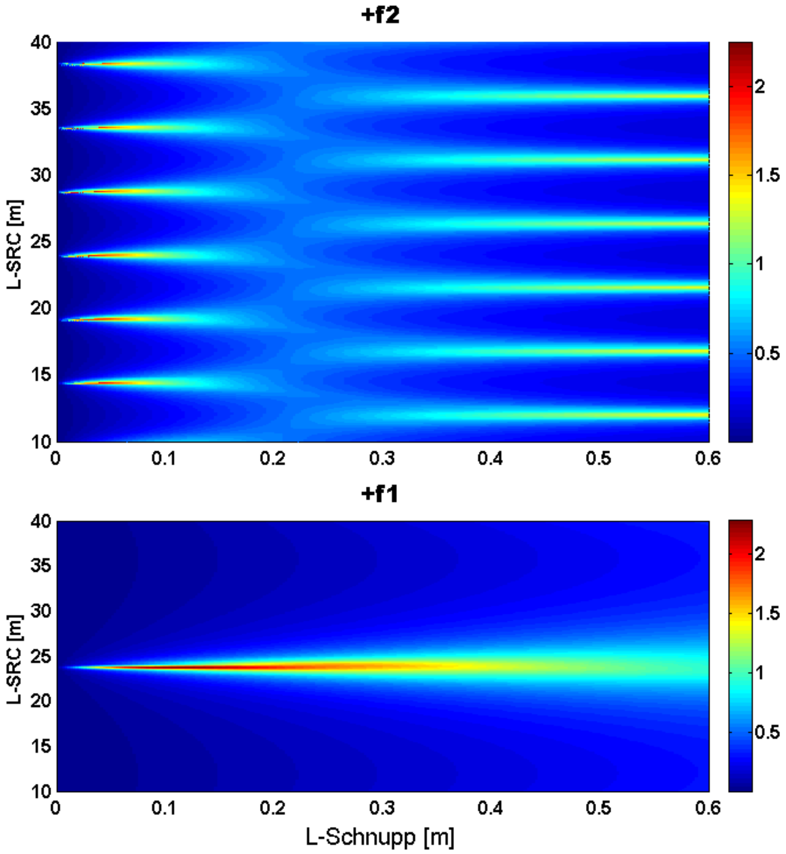

Figure A.5.: Power of the two RF modulation sidebands inside SRC for a simultaneous scan of SRC and Schnupp lengths. [HMPF09].

quired that only the modulation sideband f_2 is resonant in the SRC while f_1 has to be at the anti-resonance point in order to maximise the decoupling of the length of SRC from the other degrees of freedom. Both the lengths L_{Sch} and L_{SRC} are calculated by the OSD-Tool function (OSD_SR_Schnupp.m). This function requires as inputs the modulation frequencies sidebands and a rough length of the desired SRC length. In particular the function calculates the two lengths L_{Sch} and L_{SRC} so as to maximise the power of f_2 inside the SRC. Once the lengths are changed the function recalculates the ROC of the SRM.

Fig. A.5 shows an example of the power of the RF modulation sidebands inside the

SRC. The plot has been obtained for a simultaneous scan of L_{Sch} and L_{SRC}. The lower plot shows the power of f_1 to be maximum at $L_{\mathrm{SRC}} = 24\,\mathrm{m}$ whereas the upper plot shows the power of f_2 to be maximum for several different values of L_{Sch} and L_{SRC}. The desired SRC length is given as an input. An additional input, which selects a short or long Schnupp length, define univocally the choice of couple lengths L_{Sch} and L_{SRC}. It should be mentioned that the choice has to take into account the points where f_1 is resonant in SRC. Thus in this case, $L_{\mathrm{SRC}} \approx 24\,\mathrm{m}$ has to be excluded.

Appendix B.

Homodyne detection

In this Section is derived the mathematical output of the homodyne detectors in a general case when, on the homodyne beam splitter (BSH), interference occurs between N fields a_i of the signal beam and M fields b_i of the LO beam.

B.1. Homodyne

Fields on the two photodetectors PD1 and PD2 are described with following convention:

$$\mathrm{E}_{\mathrm{PD1}} = \sqrt{\frac{1}{2}} \sum_{i=0}^{N} a_i e^{\mathrm{i}(\omega_i t + \alpha_i)} + \sqrt{\frac{1}{2}} \mathrm{i} \sum_{j=0}^{M} b_j e^{\mathrm{i}(\omega_j t + \beta_j)} \tag{B.1}$$

$$\mathrm{E}_{\mathrm{PD2}} = \sqrt{\frac{1}{2}} \mathrm{i} \sum_{i=0}^{N} a_i e^{\mathrm{i}(\omega_i t + \alpha_i)} + \sqrt{\frac{1}{2}} \sum_{j=0}^{M} b_j e^{\mathrm{i}(\omega_j t + \beta_j)} \tag{B.2}$$

The intensity $\mathrm{I}_{\mathrm{PD1}}$ onto the photodetector PD1 can be calculated as:

$$\mathrm{I}_{\mathrm{PD1}} = \frac{1}{2}\left(\sum_{i=0}^{N} a_i e^{\mathrm{i}(\omega_i t+\alpha_i)} + \mathrm{i}\sum_{j=0}^{M} b_j e^{\mathrm{i}(\omega_j t+\beta_j)}\right)\left(\sum_{k=0}^{N} a_k^* e^{-\mathrm{i}(\omega_k t+\alpha_k)} - \mathrm{i}\sum_{l=0}^{M} b_l^* e^{-\mathrm{i}(\omega_l t+\beta_l)}\right) =$$

$$\begin{aligned}
= \quad & \frac{1}{2}\sum_{i=0}^{N} a_i e^{\mathrm{i}(\omega_i t+\alpha_i)} \sum_{k=0}^{N} a_k^* e^{-\mathrm{i}(\omega_k t+\alpha_k)} - \frac{1}{2}\mathrm{i}\sum_{i=0}^{N} a_i e^{\mathrm{i}(\omega_i t+\alpha_i)} \sum_{l=0}^{M} b_l^* e^{-\mathrm{i}(\omega_l t+\beta_l)} + \\
+ \quad & \frac{1}{2}\mathrm{i}\sum_{j=0}^{M} b_j e^{\mathrm{i}(\omega_j t+\beta_j)} \sum_{k=0}^{N} a_k^* e^{-\mathrm{i}(\omega_k t+\alpha_k)} + \frac{1}{2}\sum_{j=0}^{M} b_j e^{\mathrm{i}(\omega_j t+\beta_j)} \sum_{l=0}^{M} b_l^* e^{-\mathrm{i}(\omega_l t+\beta_l)} =
\end{aligned}$$

$$\begin{aligned}
= \quad & \frac{1}{2}\sum_{i=0}^{N}\sum_{k=0}^{N} a_i a_k^* e^{\mathrm{i}(\omega_i t+\alpha_i)} e^{-\mathrm{i}(\omega_k t+\alpha_k)} + \frac{1}{2}\sum_{j=0}^{M}\sum_{l=0}^{M} b_j b_l^* e^{\mathrm{i}(\omega_j t+\beta_j)} e^{-\mathrm{i}(\omega_l t+\beta_l)} + \\
- \quad & \frac{1}{2}\mathrm{i}\sum_{i=0}^{N}\sum_{l=0}^{M} a_i b_l^* e^{\mathrm{i}(\omega_i t+\alpha_i)} e^{-\mathrm{i}(\omega_l t+\beta_l)} + \frac{1}{2}\mathrm{i}\sum_{k=0}^{N}\sum_{j=0}^{M} a_k^* b_j e^{-\mathrm{i}(\omega_k t+\alpha_k)} e^{\mathrm{i}(\omega_j t+\beta_j)} =
\end{aligned}$$

$$\begin{aligned}
= \quad & \frac{1}{2}\sum_{i=0}^{N}\sum_{k=0}^{N} a_i a_k^* e^{\mathrm{i}(\omega_i-\omega_k)t} e^{\mathrm{i}(\alpha_i-\alpha_k)} + \frac{1}{2}\sum_{j=0}^{M}\sum_{l=0}^{M} b_j b_l^* e^{\mathrm{i}(\omega_j-\omega_l)t} e^{\mathrm{i}(\beta_j-\beta_l)} + \\
- \quad & \frac{1}{2}\mathrm{i}\sum_{i=0}^{N}\sum_{l=0}^{M} a_i b_l^* e^{\mathrm{i}(\omega_i-\omega_l)t} e^{\mathrm{i}(\alpha_i-\beta_l)} + \frac{1}{2}\mathrm{i}\sum_{k=0}^{N}\sum_{j=0}^{M} a_k^* b_j e^{-\mathrm{i}(\omega_k-\omega_j)t} e^{\mathrm{i}(\alpha_k-\beta_j)} =
\end{aligned}$$

$$\begin{aligned}
= \quad & \frac{1}{2}\sum_{i=0}^{N}(\mid a_i \mid^2 + \sum_{k=i+1}^{N}(a_i a_k^* e^{\mathrm{i}(\omega_i-\omega_k)t} e^{\mathrm{i}(\alpha_i-\alpha_k)} + a_i^* a_k e^{-\mathrm{i}(\omega_i-\omega_k)t} e^{-\mathrm{i}(\alpha_i-\alpha_k)})) + \\
+ \quad & \frac{1}{2}\sum_{j=0}^{M}(\mid b_j \mid^2 + \sum_{l=j+1}^{M}(b_j b_l^* e^{\mathrm{i}(\omega_j-\omega_l)t} e^{\mathrm{i}(\beta_j-\beta_l)} + b_j^* b_l e^{-\mathrm{i}(\omega_j-\omega_l)t} e^{-\mathrm{i}(\beta_j-\beta_l)})) + \\
+ \quad & \sum_{i=0}^{N}\sum_{l=0}^{M} \Im\{a_i b_l^* e^{\mathrm{i}(\omega_i-\omega_l)t} e^{\mathrm{i}(\alpha_i-\beta_l)}\}
\end{aligned}$$

In a very compact form then

$$\begin{aligned}
\mathbf{I_{PD1}} &= \frac{1}{2}\sum_{i=0}^{N}(\mid a_i \mid^2 + \sum_{k=i+1}^{N} \mathrm{Re}\{a_i a_k^* e^{\mathrm{i}(\omega_i-\omega_k)t} e^{\mathrm{i}(\alpha_i-\alpha_k)}\}) + \\
&+ \frac{1}{2}\sum_{j=0}^{M}(\mid b_j \mid^2 + \sum_{l=j+1}^{M} \mathrm{Re}\{b_j b_l^* e^{\mathrm{i}(\omega_j-\omega_l)t} e^{\mathrm{i}(\beta_j-\beta_l)}\}) + \\
&+ \sum_{i=0}^{N}\sum_{j=0}^{M} \Im\{a_i b_j^* e^{\mathrm{i}(\omega_i-\omega_j)t} e^{\mathrm{i}(\alpha_i-\beta_j)}\} \qquad \text{(B.3)}
\end{aligned}$$

$$\begin{aligned}
\mathbf{I_{PD2}} &= \frac{1}{2}\sum_{i=0}^{N}(\mid a_i \mid^2 + \sum_{k=i+1}^{N} \mathrm{Re}\{a_i a_k^* e^{\mathrm{i}(\omega_i-\omega_k)t} e^{\mathrm{i}(\alpha_i-\alpha_k)}\}) + \\
&+ \frac{1}{2}\sum_{j=0}^{M}(\mid b_j \mid^2 + \sum_{l=j+1}^{M} \mathrm{Re}\{b_j b_l^* e^{\mathrm{i}(\omega_j-\omega_l)t} e^{\mathrm{i}(\beta_j-\beta_l)}\}) + \\
&- \sum_{i=0}^{N}\sum_{j=0}^{M} \Im\{a_i b_j^* e^{\mathrm{i}(\omega_i-\omega_j)t} e^{\mathrm{i}(\alpha_i-\beta_j)}\} \qquad \text{(B.4)}
\end{aligned}$$

Using $\omega_{ij} = \omega_i - \omega_j$, $\alpha = \beta$, $\varphi_{ij} = \alpha_i - \alpha_j$ the two photocurrents can be rewritten as:

$$\begin{aligned}
\mathbf{I_{PD1}} &= \frac{1}{2}\sum_{i=0}^{N}(\mid a_i \mid^2 + \sum_{k=i+1}^{N} \mathrm{Re}\{a_i a_k^* e^{\mathrm{i}\omega_{ik}t} e^{\mathrm{i}\varphi_{ik}}\}) + \\
&+ \frac{1}{2}\sum_{j=0}^{M}(\mid b_j \mid^2 + \sum_{l=j+1}^{M} \mathrm{Re}\{b_j b_l^* e^{\mathrm{i}\omega_{jl}t} e^{\mathrm{i}\varphi_{jl}}\}) + \\
&+ \sum_{i=0}^{N}\sum_{j=0}^{M} \Im\{a_i b_j^* e^{\mathrm{i}\omega_{ij}t} e^{\mathrm{i}\varphi_{ij}}\} \qquad \text{(B.5)}
\end{aligned}$$

$$\begin{aligned}\mathbf{I_{PD2}} &= \frac{1}{2}\sum_{i=0}^{N}(\mid a_i\mid^2 + \sum_{k=i+1}^{N}\mathrm{Re}\{a_i a_k^* e^{\mathrm{i}\omega_{ik}t}e^{\mathrm{i}\varphi_{ik}}\}) + \\ &+ \frac{1}{2}\sum_{j}(\mid b_j\mid^2 + \sum_{l=j+1}^{M}\mathrm{Re}\{b_j b_l^* e^{\mathrm{i}\omega_{jl}t}e^{\mathrm{i}\varphi_{jl}}\}) + \\ &- \sum_{i=0}^{N}\sum_{j=0}^{M}\Im\{a_i b_j^* e^{\mathrm{i}\omega_{ij}t}e^{\mathrm{i}\varphi_{ij}}\}\end{aligned} \tag{B.6}$$

The difference is:

$$\mathbf{I_{21}} = 2\sum_{i=0}^{N}\sum_{j=0}^{M}\Im\{a_i b_j^* e^{\mathrm{i}\omega_{ij}t}e^{\mathrm{i}\varphi_{ij}}\} = \tag{B.7}$$

$$= 2\left(\sum_{i=0}^{N}\Im\{a_i b_i e^{\mathrm{i}\varphi_{ii}}\} + \sum_{j=i+1}^{N}\Im\{a_i b_j^* e^{\mathrm{i}\omega_{ij}t}e^{\mathrm{i}\varphi_{ij}} + b_i^* a_j e^{-\mathrm{i}\omega_{ij}t}e^{-\mathrm{i}\varphi_{ij}}\}\right) \tag{B.8}$$

When looking for DC components

$$\mathbf{I_{21}} = 2\sum_{i=0}^{N}\Im\{a_i b_i e^{\mathrm{i}\varphi_{ii}}\} \tag{B.9}$$

B.1.1. Example 1: One field in each beam

From the equation (B.9) setting $N = M = 0$ and using $\varphi_{00} = \varphi_0 - \varphi_0 + \beta = \varphi_H$ it can be written

$$\begin{aligned}\mathbf{I_{21}} &= 2\Im\{a_0 b_0^* e^{\mathrm{i}\varphi_{00}}\} = 2\Im\{a_0 b_0^* e^{\mathrm{i}\varphi_H}\} = 2\left(\frac{a_0 b_0^* e^{\mathrm{i}\varphi_H} - a_0^* b_0 e^{-\mathrm{i}\varphi_H}}{2\mathrm{i}}\right) = \\ &= 2a_0 b_0 \sin\varphi_H \qquad \text{(B.10)}\end{aligned}$$

where a_0 and b_0 have been considered real numbers and φ_H is the LO phase shifter.

B.1.2. Example 2: Three fields on both beams

From the equation (B.9) setting $N = M = 2$ and using $\varphi_{ii} = \varphi_i - \varphi_i + \beta = \varphi_H$ it can be written

$$\mathbf{I_{21}} = 2\sum_{i=0}^{2} \Im\{a_i b_i e^{\mathrm{i}\varphi_{ii}}\} = 2\Im\{(a_0 b_0 + a_1 b_1 + a_2 b_2)\, e^{-\mathrm{i}\varphi_H}\} \qquad \text{(B.11)}$$

where a_i and b_i have been considered real numbers and φ_H is the LO phase shifter.

Appendix C.

Simulated quadrature analysis

C.0.3. Scanning the quadrature angles: HD1 starts in AQ and HD2 in PQ

In this subsection the homodyne quadrature analysis is done by performing the DN and the GW transfer functions at fixed frequencies against the quadrature angles where the scanning of the quadratures starts when HD1 is in amplitude quadrature and HD2 is in phase quadrature. The entire cycle of the quadratures is for tunings of both BSH1 and BSH2 from 0° to 90°. Tunings at 0° give HD1 in amplitude quadratures, and HD2 in phase quadrature. In this case at 45° HD1 is in phase quadrature and HD2 is in amplitude quadrature.

The left-hand side of Fig. C.1 shows the DN transfer functions from the input cavity mirror to HD1 (blue curve) and HD2 (green curve), respectively named $S1_{\mathrm{DN}}$ and $S2_{\mathrm{DN}}$. $S1_{\mathrm{DN}}$ has a minimum of zero at 4.7° while $S2_{\mathrm{DN}}$ has a minimum of zero at 19.3°. In between these two points the respective phases are the same while

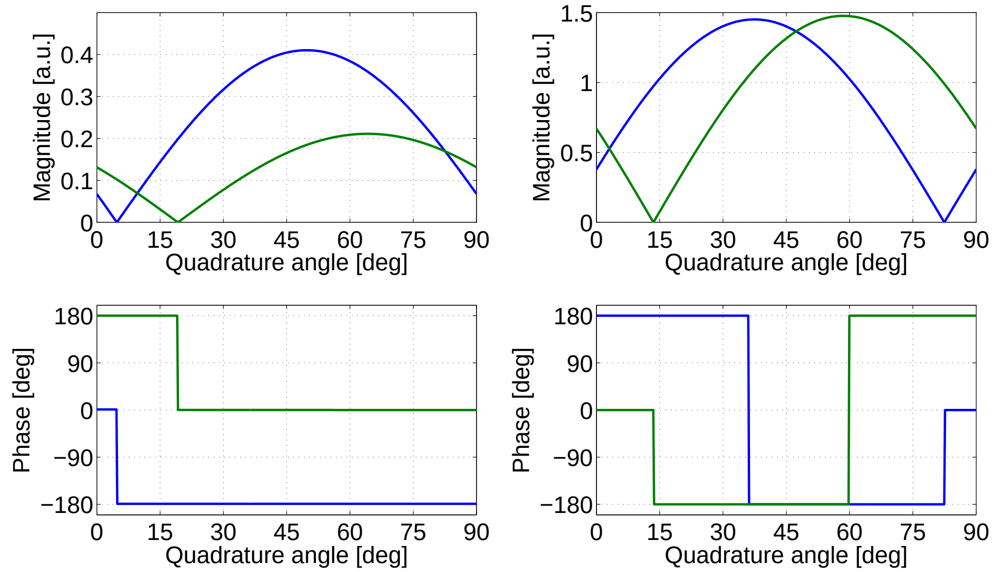

Figure C.1.: DN and the GW transfer functions at fixed frequency vs quadrature angle. The scanning of the quadratures starts when HD1 is in amplitude quadrature and HD2 is in phase quadrature. The left-hand side of shows the DN transfer functions from the input cavity mirror to HD1 (blue curve) and HD2 (green curve). The right-hand side shows the GW transfer functions from the cavity-length to HD1 (blue curve) and HD2 (green curve).

everywhere else they are shifted by 180°. The right-hand side of Fig. C.1 shows the GW transfer functions from the cavity-length to HD1 (blue curve) and HD2 (green curve), respectively named $S1_{\mathrm{GW}}$ and $S2_{\mathrm{GW}}$. $S1_{\mathrm{GW}}$ has a minimum of zero at 82.4° while $S2_{\mathrm{GW}}$ has a minimum of zero at 13.5°. In between these two points the respective phases are the same while everywhere else are shifted by 180°.

Fig. C.2 shows the initial SNRs, σ_{S1} and σ_{S2}, of the unprocessed data respectively in HD1 (left-hand side) and HD2 (right-hand side). σ_{S1} has a peak of ≈ 500 at 4.7° and a minimum of $\approx 10^{-3}$ at 82.4°, while σ_{S2} has a peak of $\approx 10^{3}$ at 19.3° and a minimum of $\approx 10^{-2}$ at 13.5°.

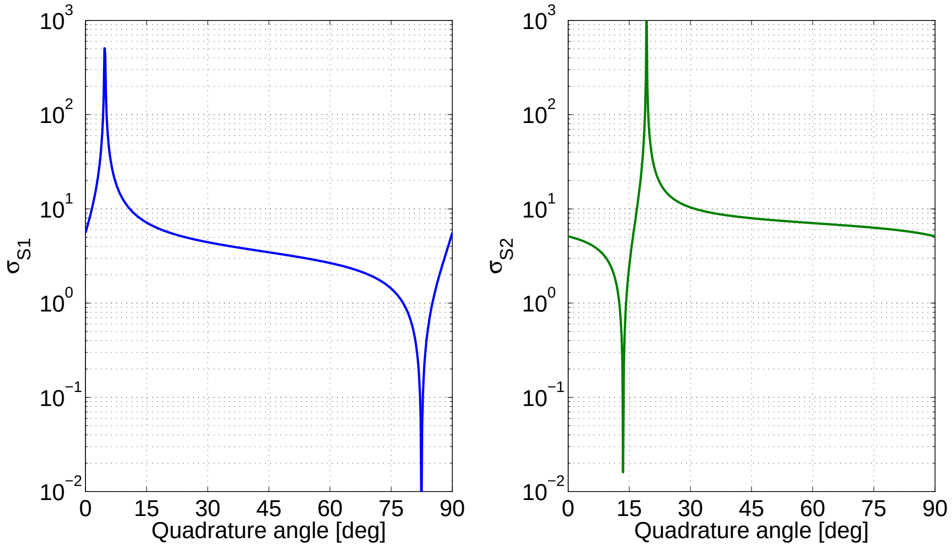

Figure C.2.: SNRs of the unprocessed data vs quadrature angle. Tunings at 0° give HD1 in amplitude quadratures and HD2 in phase quadrature. At 45° HD1 is in phase quadrature and HD2 is in amplitude quadrature. On the left-hand side is plotted the SNR in HD1 σ_{S1}. On the right-hand side is plotted the SNR in HD2 σ_{S2}.

Fig. C.3 shows the SNRs of the DFI processed data. On the left-hand side the SNR of the DFI+ channel, $\sigma_{\mathrm{DFI+}} = S2_{\mathrm{GW,DFI+}}/S2_{\mathrm{DN,DFI+}}$, when the latter is built taking into account the plus sign in the equations 4.1. On the right-hand side the SNR of the DFI- channel, $\sigma_{\mathrm{DFI-}} = S2_{\mathrm{GW,DFI-}}/S2_{\mathrm{DN,DFI-}}$, when the latter is built taking into account the plus sign in the equations 4.1. Both $\sigma_{\mathrm{DFI+}}$ and $\sigma_{\mathrm{DFI-}}$ show peaks at 4.7° and 19.3°.

In between those two values $\sigma_{\mathrm{DFI-}}$ is relatively high varying from $\approx 10^2$ to $\approx 10^3$ with a minimum of ≈ 20 at 16.4°. In the complementary interval $\sigma_{\mathrm{DFI+}}$ shows relative high values varying from ≈ 300 to ≈ 800.

In Fig. C.4 is shown the enhancement effect ρ_i of the DFI. The ratio ρ_i between the processed and unprocessed SNRs are evaluated. The plots are organised as

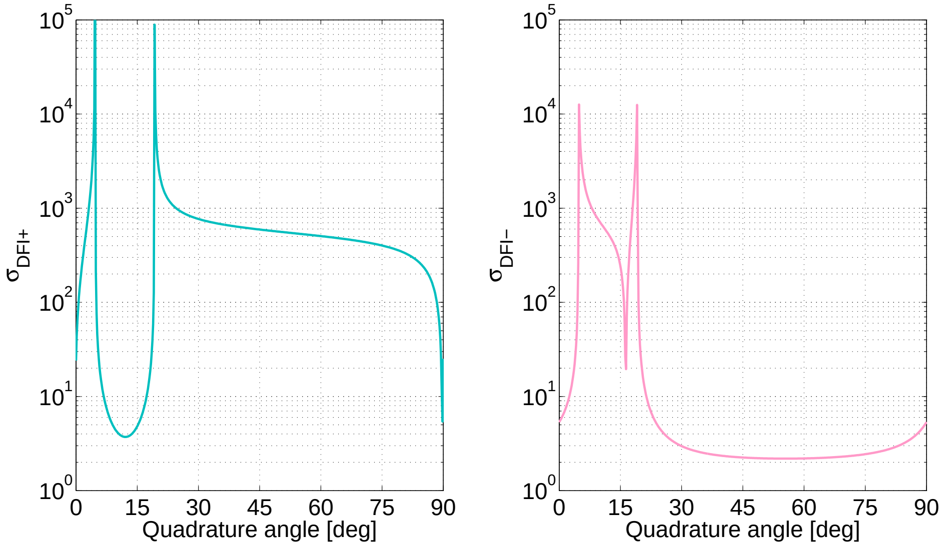

Figure C.3.: SNRs of the DFI processed data. Tunings at 0° give HD1 in amplitude quadratures and HD2 in phase quadrature. At 45° HD1 is in phase quadrature and HD2 is in amplitude quadrature. On the left-hand side the SNR of the DFI+ channel $\sigma_{\mathrm{DFI+}} = S2_{\mathrm{GW,DFI+}}/S2_{\mathrm{DN,DFI+}}$. On the right-hand side the SNR of the DFI- channel $\sigma_{\mathrm{DFI-}} = S2_{\mathrm{GW,DFI-}}/S2_{\mathrm{DN,DFI-}}$.

follows: On the top-left-hand side $\rho_{\mathrm{S1+}} = \sigma_{\mathrm{DFI+}}/\sigma_{\mathrm{S1}}$. On the top-right-hand side $\rho_{\mathrm{S2+}} = \sigma_{\mathrm{DFI+}}/\sigma_{\mathrm{S2}}$. On the bottom-left-hand side $\rho_{\mathrm{S1-}} = \sigma_{\mathrm{DFI-}}/\sigma_{\mathrm{S2}}$. On the bottom-right-hand side $\rho_{\mathrm{S2-}} = \sigma_{\mathrm{DFI-}}/\sigma_{\mathrm{S2}}$.

$\rho_{\mathrm{S1+}}$ shows three peaks of $\approx 5 \cdot 10^3$, $\approx 10^4$ and $\approx 10^4$ respectively at 4°, 19.3° and 82.4°. In the region between 25° and 65° a relative high enhancement effect $\rho_{\mathrm{S1+}}$ of ≈ 200 is seen. In the same region $\rho_{\mathrm{S2+}}$ shows a relative high enhancement effect of ≈ 100 and a peak of $\approx 10^4$ at 4°. On the other hand $\rho_{\mathrm{S1-}}$ shows an enhancement effect of ≈ 70 in the region in between 5° and 20°. In contrast in the same region $\rho_{\mathrm{S2-}}$ shows an enhancement effect of ≈ 200. with a peak of $\approx 10^4$ at 13.5°.

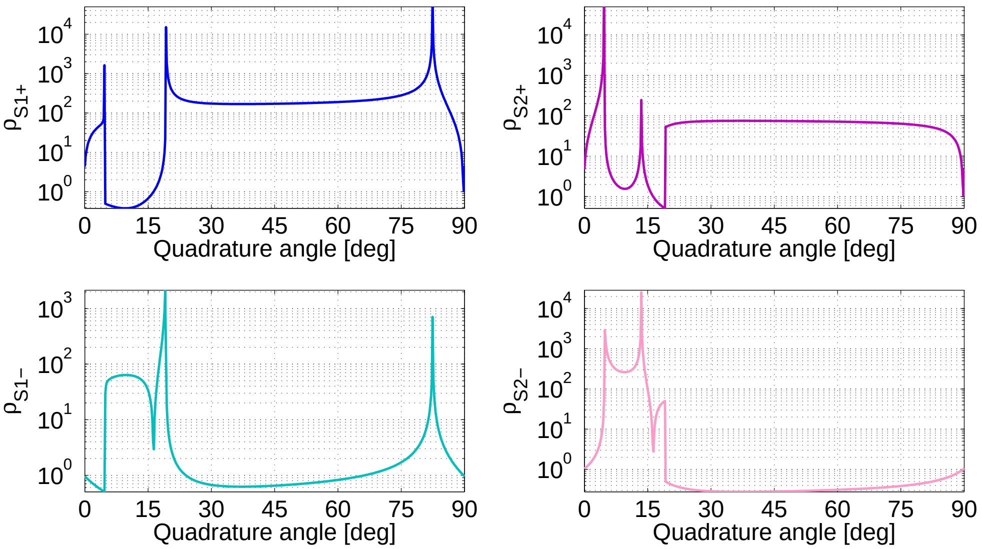

Figure C.4.: Enhancement effect of the DFI. Tunings at 0° give HD1 in amplitude quadratures and HD2 in phase quadrature. At 45° HD1 is in phase quadrature and HD2 is in amplitude quadrature. The ratio ρ_i between the processed and unprocessed SNRs against the quadrature angles are evaluated. The plots are organised as follows: On the top-left-hand side $\rho_{\mathrm{S1+}} = \sigma_{\mathrm{DFI+}}/\sigma_{\mathrm{S1}}$. On the top-right-hand side $\rho_{\mathrm{S2+}} = \sigma_{\mathrm{DFI+}}/\sigma_{\mathrm{S2}}$. On the bottom-left-hand side $\rho_{\mathrm{S1-}} = \sigma_{\mathrm{DFI-}}/\sigma_{\mathrm{S2}}$. On the bottom-right-hand side $\rho_{\mathrm{S2-}} = \sigma_{\mathrm{DFI-}}/\sigma_{\mathrm{S2}}$.

C.0.4. Scanning the quadrature angles: HD1 and HD2 start at maximum GW detection

In this subsection the homodyne quadratures analysis is done by performing the DN and the GW transfer functions at a fixed frequency against the quadrature angles where the scanning of the quadratures starts when HD1 and HD2 are able to detect the maximum GW signal. The entire cycle of the quadratures goes for tunings of both BSH1 and BSH2 from 0° to 90°. Tunings at 0° give the maximum detectable GW signal in HD1 and HD2.

The left-hand side of Fig. C.5 shows the DN transfer functions from the input cavity

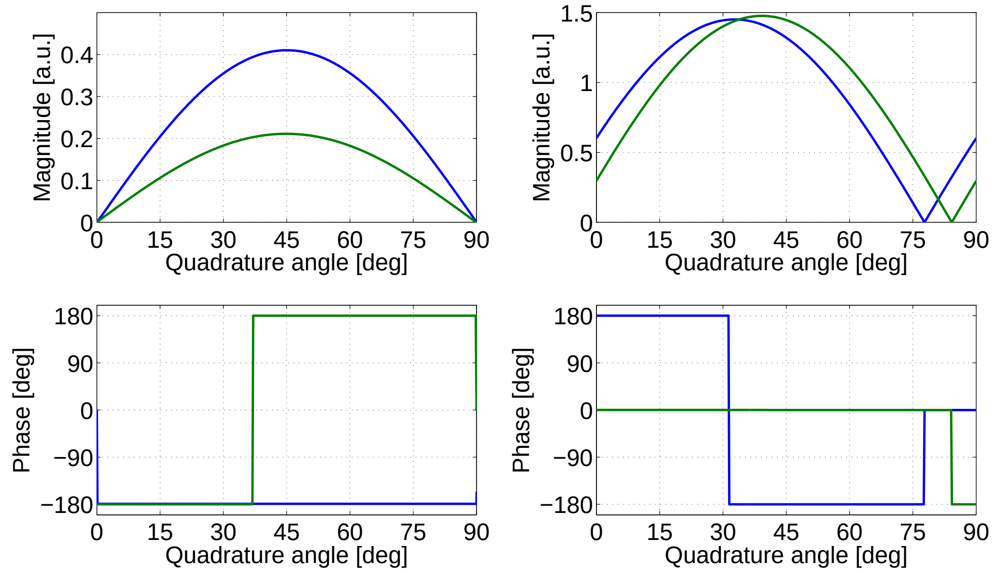

Figure C.5.: DN and the GW transfer functions at fixed frequency vs quadrature angle. The scanning of the quadratures starts when both the homodyne detectors are able to detect the maximum GW signal. The left-hand side of shows the DN transfer functions from the input cavity mirror to HD1 (blue curve) and HD2 (green curve). The right-hand side shows the GW transfer functions from the cavity-length to HD1 (blue curve) and HD2 (green curve).

mirror to HD1 and HD2, respectively named $S1_{\mathrm{DN}}$ and $S2_{\mathrm{DN}}$.

Both $S1_{\mathrm{DN}}$ (blue curve) and $S2_{\mathrm{DN}}$ (green curve) have a minimum at 0° and 90° which represents the same point. The phases are the same in all the range of the quadratures angle. The right-hand side of Fig. C.5 shows the GW transfer functions from the cavity-length to HD1 (blue curve) and HD2 (green curve), respectively named $S1_{\mathrm{GW}}$ and $S2_{\mathrm{GW}}$. $S1_{\mathrm{GW}}$ has a minimum of zero at 77.8° while $S2_{\mathrm{GW}}$ has a minimum of zero at 84.4°. In between these two points the respective phases are the same while everywhere else they are shifted by 180°.

Fig. C.6 shows the initial SNRs, σ_{S1} and σ_{S2}, of the unprocessed data respectively

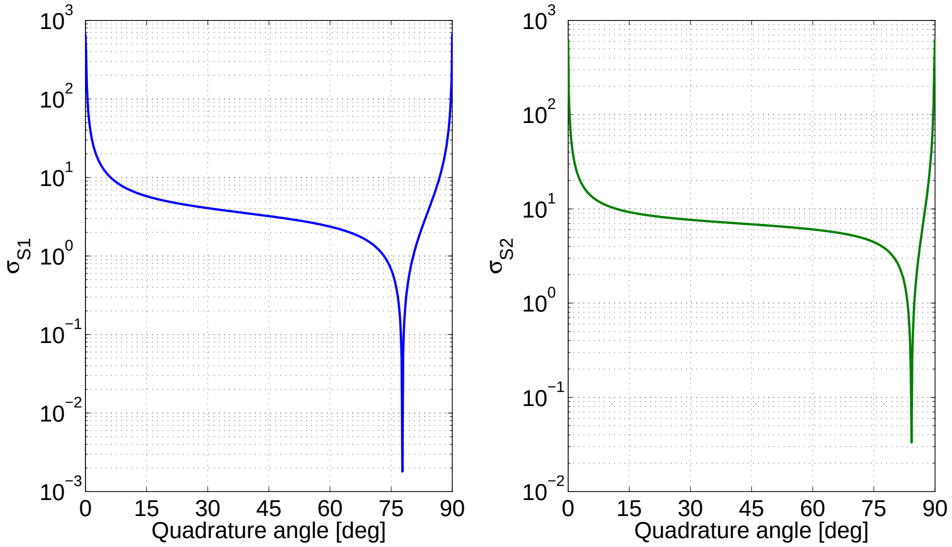

Figure C.6.: SNRs of the unprocessed data vs quadrature angle. The scanning of the quadratures starts when HD1 and HD2 are able to detect the maximum GW signal. On the left-hand side is plotted the SNR in HD1 σ_{S1}. On the right-hand side is plotted the SNR in HD2 σ_{S2}.

in HD1 (left-hand side) and HD2 (right-hand side). σ_{S1} has a peak of ≈ 600 at 0° and a minimum of $\approx 10^{-3}$ at 77.8°, while σ_{S2} has a peak of ≈ 600 at 0° and a minimum of $\approx 10^{-1}$ at 84.2°.

Fig. C.7 shows the SNRs of the DFI processed data. On the left-hand side the SNR of the DFI+ channel, $\sigma_{\mathrm{DFI+}} = S2_{\mathrm{GW,DFI+}}/S2_{\mathrm{DN,DFI+}}$. On the right-hand side the SNR of the DFI- channel, $\sigma_{\mathrm{DFI-}} = S2_{\mathrm{GW,DFI-}}/S2_{\mathrm{DN,DFI-}}$. Both $\sigma_{\mathrm{DFI+}}$ and $\sigma_{\mathrm{DFI-}}$ show peaks at 0° and 90°. In the whole range of the quadratures angle $\sigma_{\mathrm{DFI+}}$ is constantly equal to 2 with a minimum of $\approx 10^{-1}$ at 89°, while $\sigma_{\mathrm{DFI-}}$ is relatively high varying from $\approx 3 \cdot 10^4$ to $\approx 10^2$ with a minimum of ≈ 10 at 82°.

In Fig. C.8 the enhancement effect ρ_i of the DFI is shown. The ratio ρ_i between the processed and unprocessed SNRs are evaluated. The plots are organised as follows: On the top-left-hand side $\rho_{\mathrm{S1+}} = \sigma_{\mathrm{DFI+}}/\sigma_{\mathrm{S1}}$. On the top-right-hand side

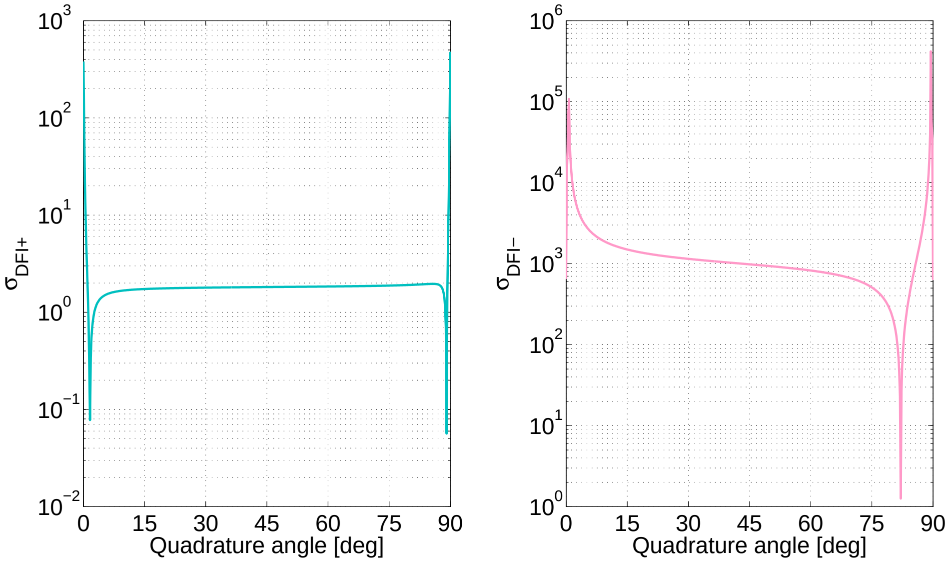

Figure C.7.: SNRs of the DFI processed data. The scanning of the quadratures starts when HD1 and HD2 are able to detect the maximum GW signal. On the left-hand side the SNR of the DFI+ channel $\sigma_{\mathrm{DFI+}} = S2_{\mathrm{GW,DFI+}}/S2_{\mathrm{DN,DFI+}}$. On the right-hand side the SNR of the DFI- channel $\sigma_{\mathrm{DFI-}} = S2_{\mathrm{GW,DFI-}}/S2_{\mathrm{DN,DFI-}}$.

$\rho_{\mathrm{S2+}} = \sigma_{\mathrm{DFI+}}/\sigma_{\mathrm{S2}}$. On the bottom-left-hand side $\rho_{\mathrm{S1-}} = \sigma_{\mathrm{DFI-}}/\sigma_{\mathrm{S2}}$. On the bottom-right-hand side $\rho_{\mathrm{S2-}} = \sigma_{\mathrm{DFI-}}/\sigma_{\mathrm{S2}}$.

$\rho_{\mathrm{S1+}}$ and $\rho_{\mathrm{S2+}}$ are below 1 except at 77.8° and 84.2°. On the other hand $\rho_{\mathrm{S1-}}$ shows an enhancement effect almost constantly at ≈ 300 in the region in between 5° and 75° with a peak of $\approx 10^5$ at 75°, while in the same region $\rho_{\mathrm{S2-}}$ shows an enhancement effect of ≈ 150 and a peak of $\approx 10^4$ at 84.2°.

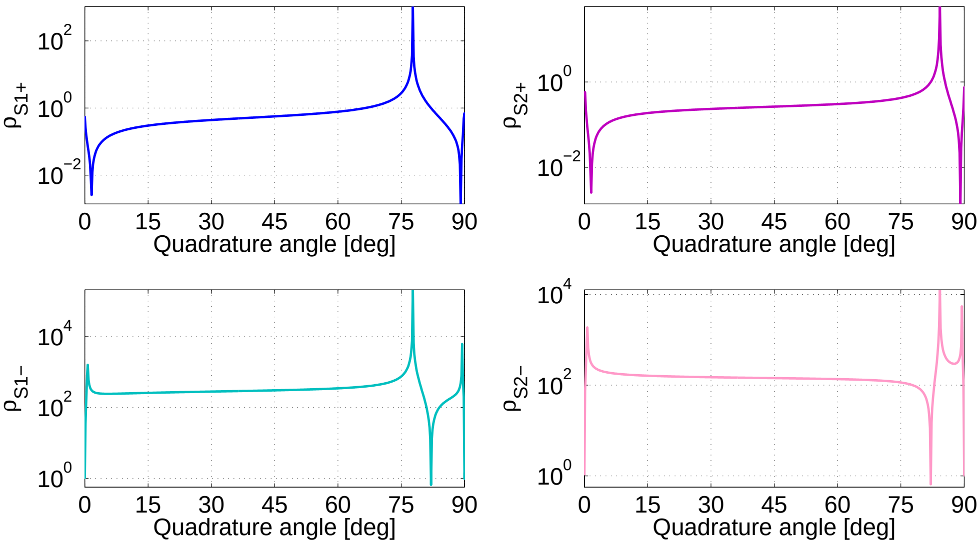

Figure C.8.: Enhancement effect of the DFI. The scanning of the quadratures starts when HD1 and HD2 are able to detect the maximum GW signal. The ratio ρ_i between the processed and unprocessed SNRs against the quadrature angles. The plots are organised as follows: On the top-left-hand side $\rho_{\mathrm{S1+}} = \sigma_{\mathrm{DFI+}}/\sigma_{\mathrm{S1}}$. On the top-right-hand side $\rho_{\mathrm{S2+}} = \sigma_{\mathrm{DFI+}}/\sigma_{\mathrm{S2}}$. On the bottom-left-hand side $\rho_{\mathrm{S1-}} = \sigma_{\mathrm{DFI-}}/\sigma_{\mathrm{S2}}$. On the bottom-right-hand side $\rho_{\mathrm{S2-}} = \sigma_{\mathrm{DFI-}}/\sigma_{\mathrm{S2}}$.

Appendix D.

Electronics circuits

In this Appendix are collected the circuit diagrams of the electronic devices used in the DFI experiment described in this thesis. The diagrams have been designed by H. Vahlbruch and B. Hage and consequently used to build with appropriate modifications the described electronic devices to realize the demonstration of the DFI experiment.

D.1. Photodetectors

The circuit diagrams of photodetectors used to detect the reflected signal by the cavity and into the homodyne detectors are displayed in Figures D.1 and D.2.

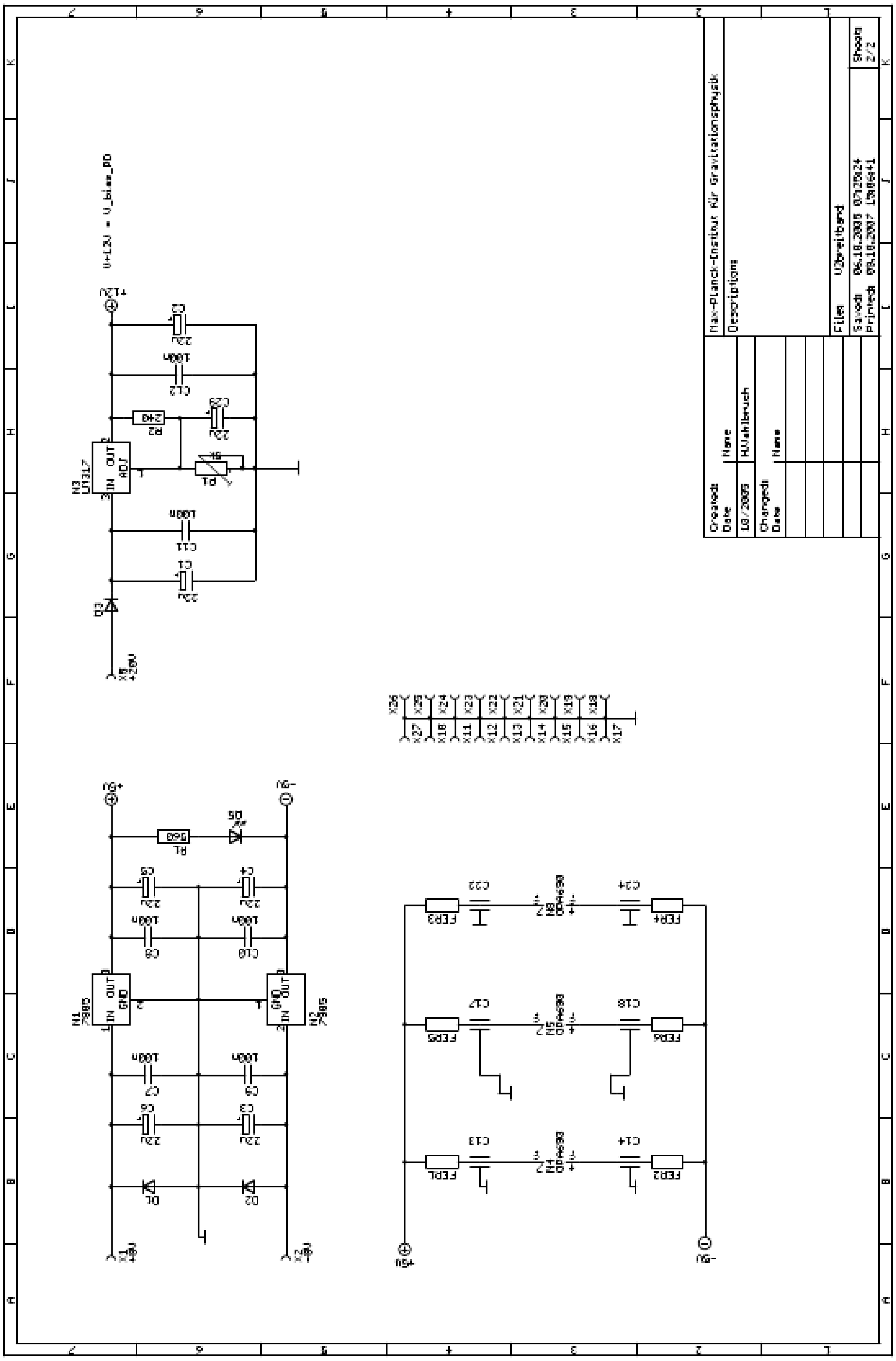

Figure D.1.: Photodetector. Part 1/2

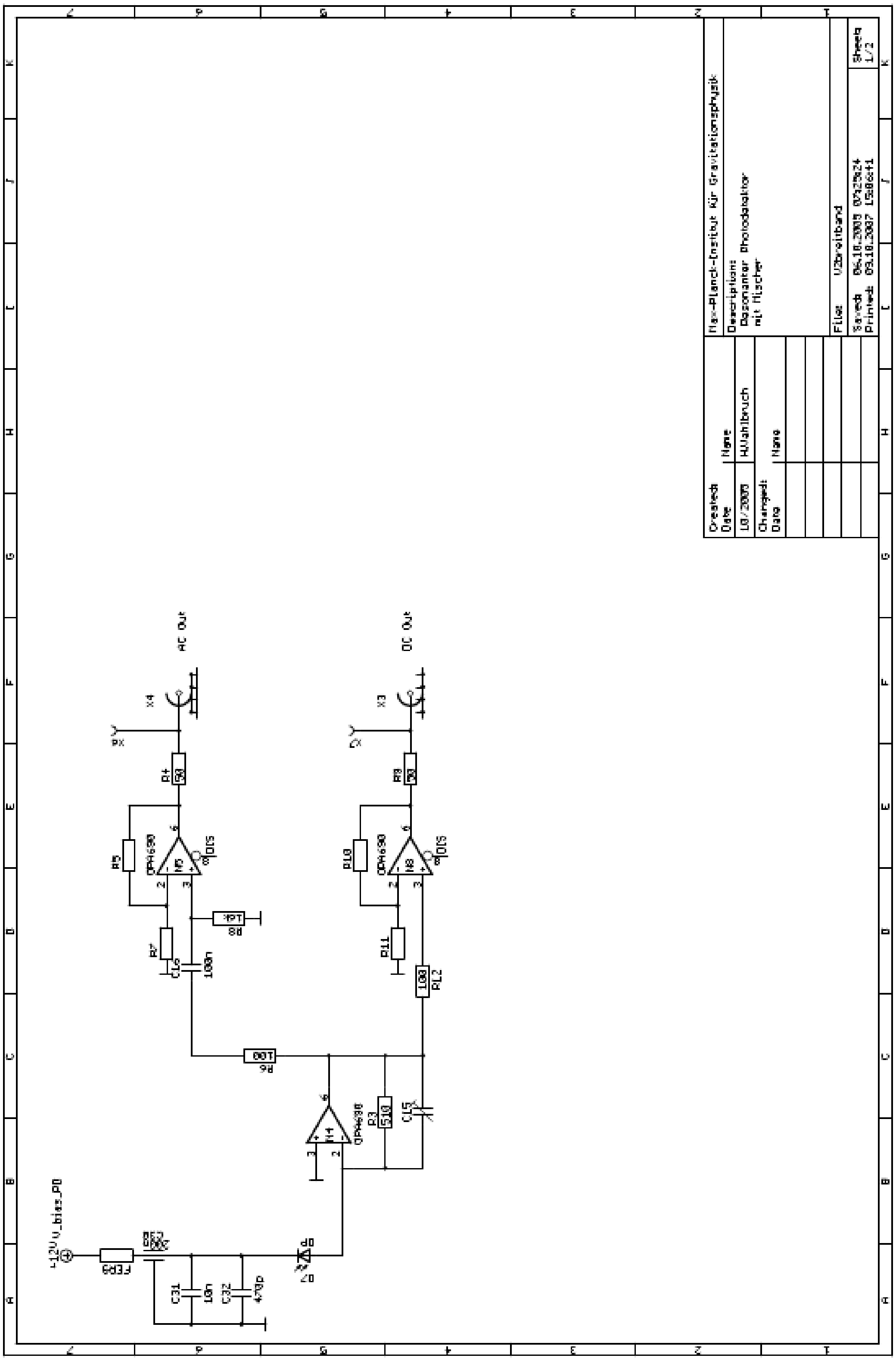

Figure D.2.: Photodector. Part 2/2

D.2. Subtractor

The circuit diagrams of the Subtractor device for both the homodynes detectors are displayed in Figures D.3 and D.4.

D.3. Servo

The circuit diagrams of the servos devices used to control the cavity and the two homodyne detectors loop are displayed in Figures D.5, D.6 and D.7

D.4. Mixer

The circuit diagrams of the mixer used to control the cavity are displayed in Figures D.8, D.9, D.10 and D.11.

D.5. Local oscillator

The circuit diagram of the oscillator used for the demodulation of the light is shown in Fig. D.12.

D.6. Active Buffer

An active buffer has been used to inject a swept-sine signal and simultaneously feedback signal Fig. D.13 on the input cavity mirror.

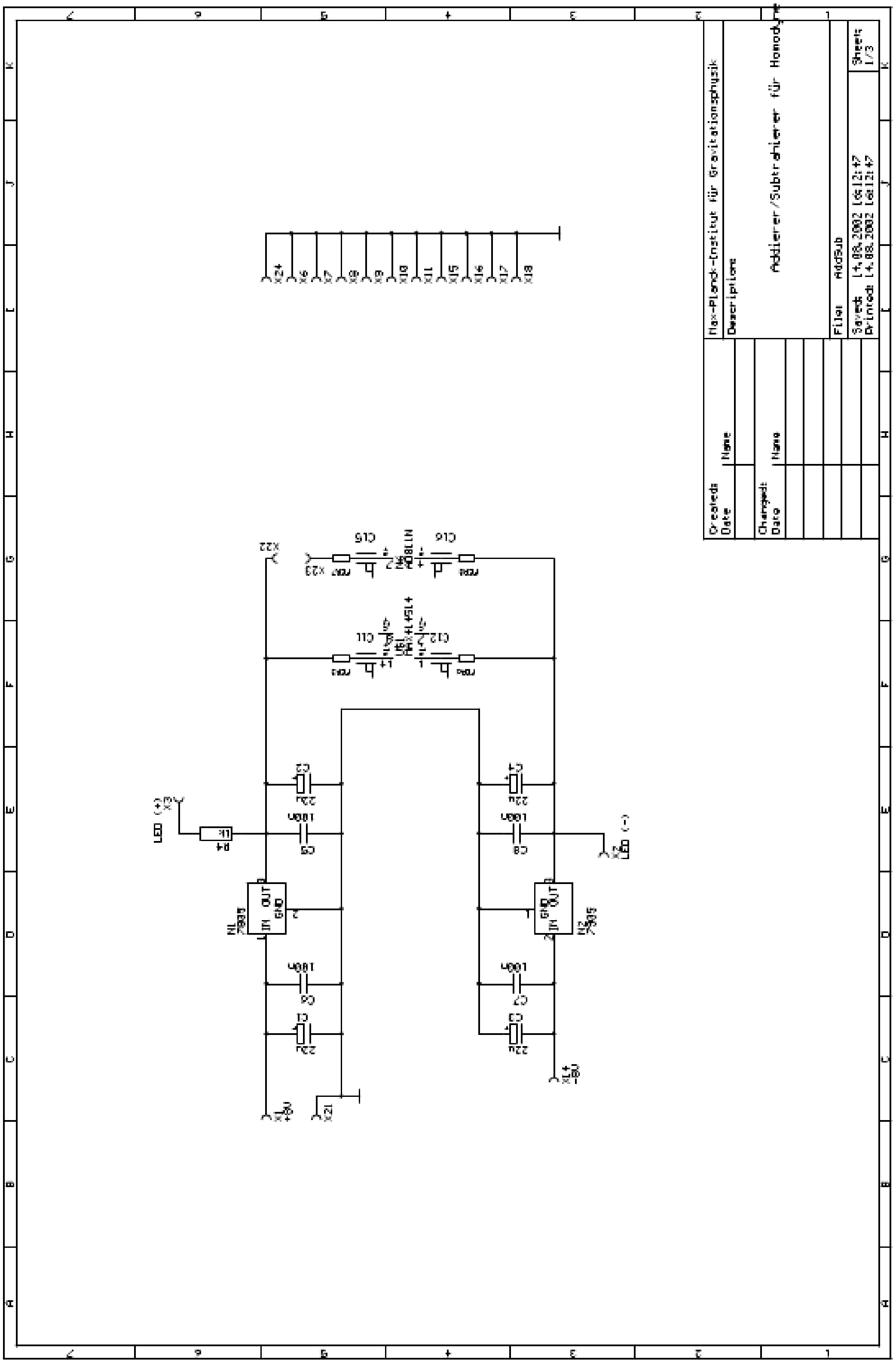

Figure D.3.: Subtractor. Part 1/2

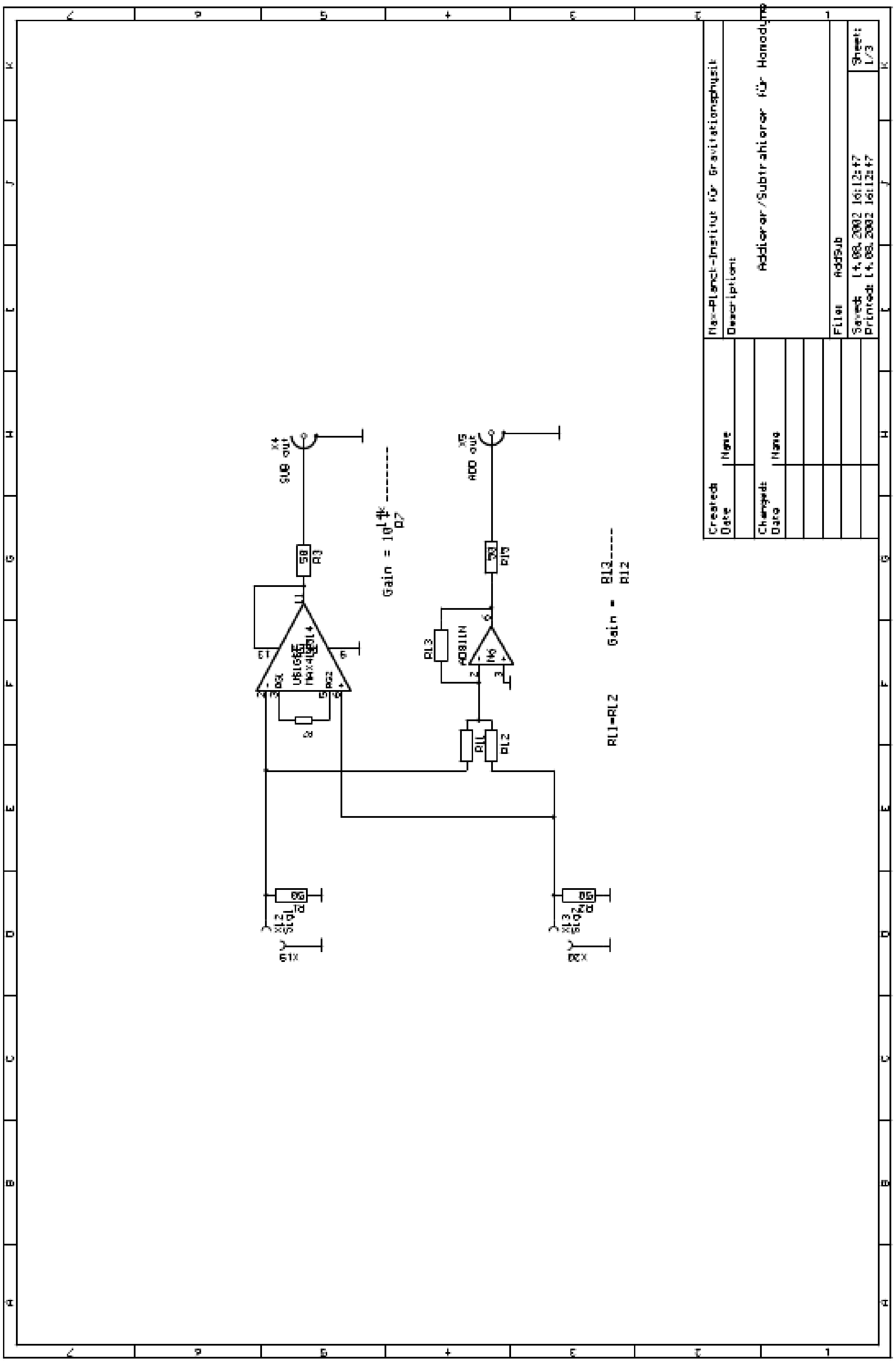

Figure D.4.: Subtractor. Part 2/2

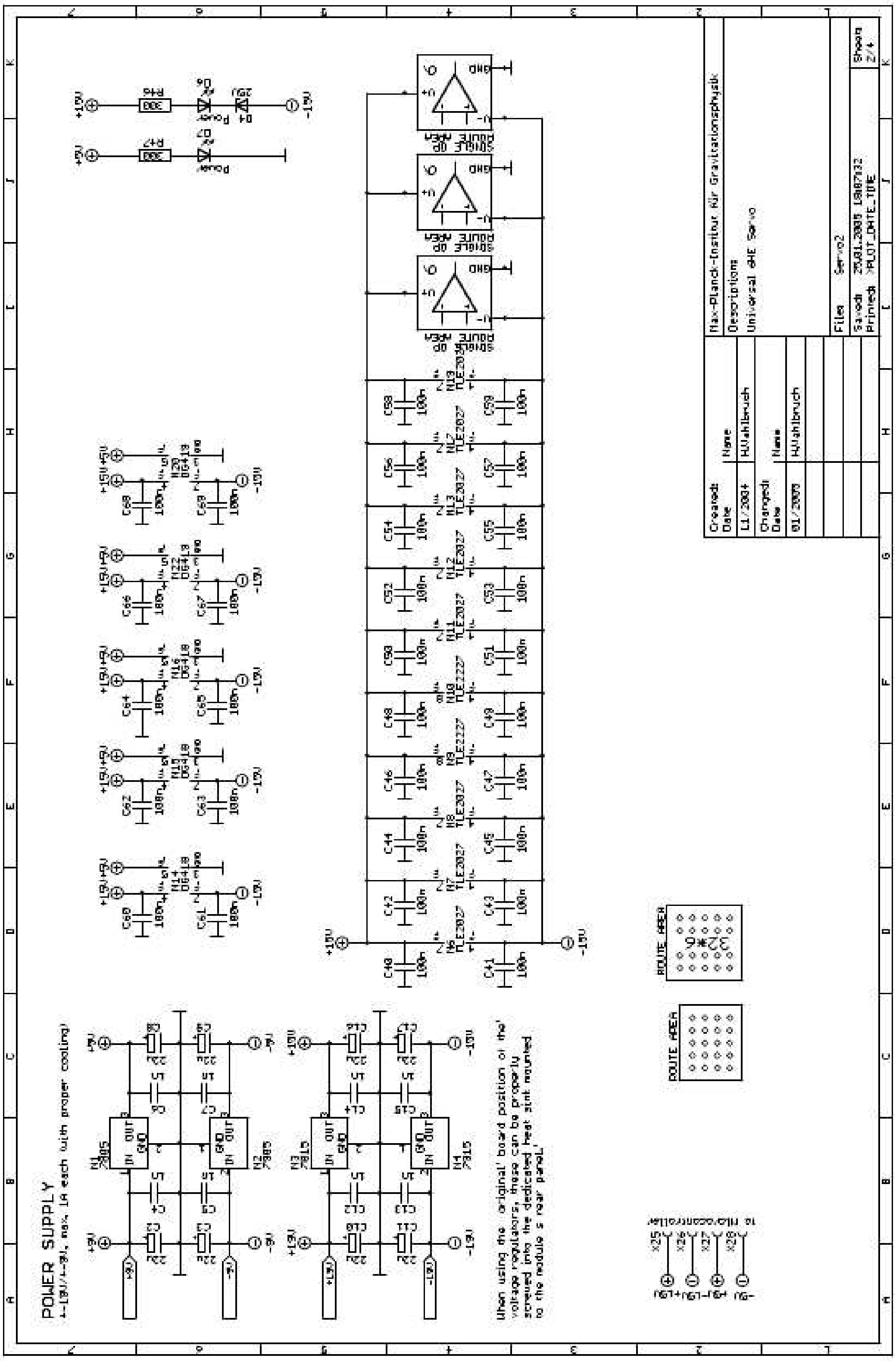

Figure D.5.: Servo. Part 1/3

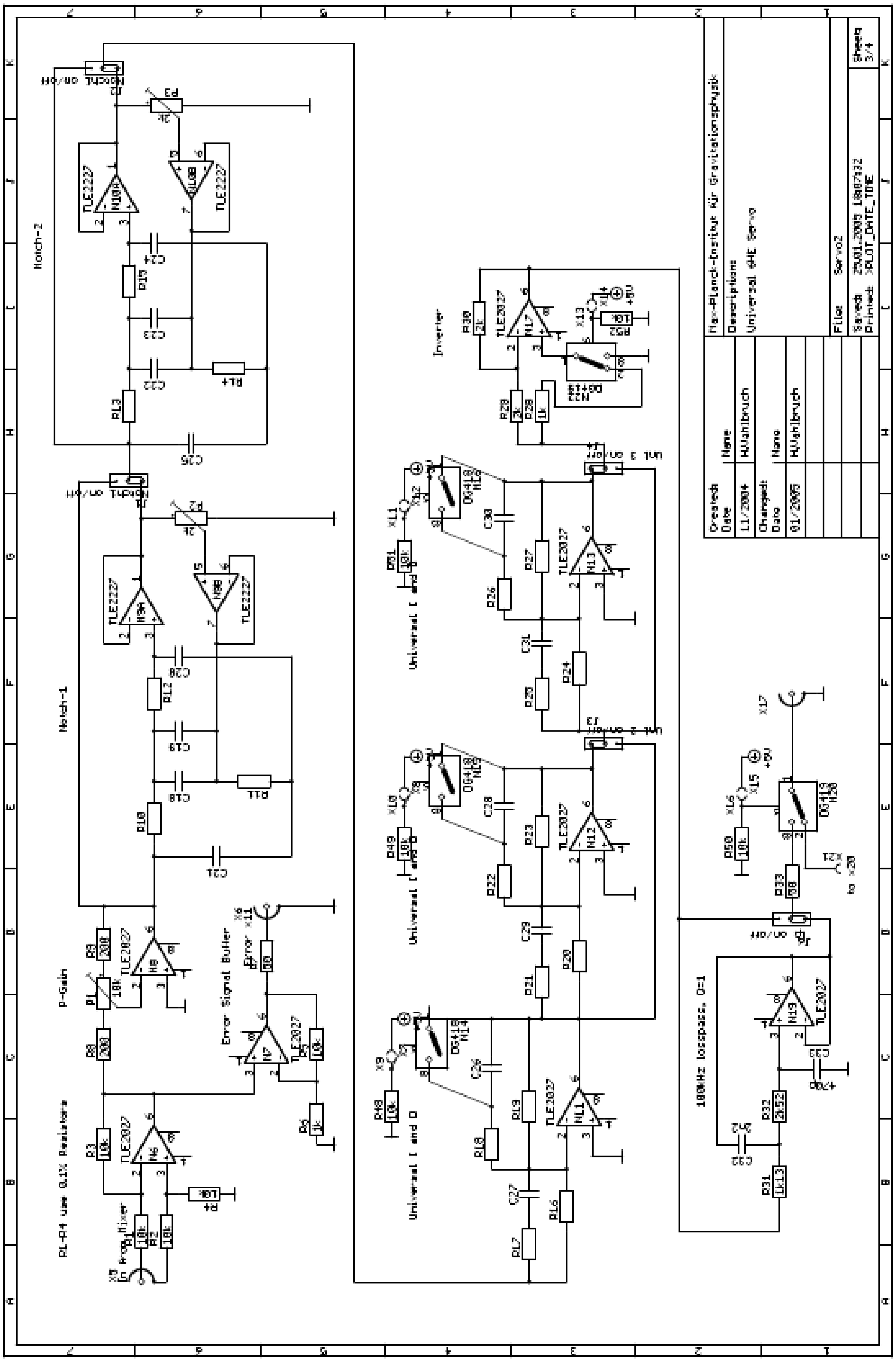

Figure D.6.: Servo. Part 2/3

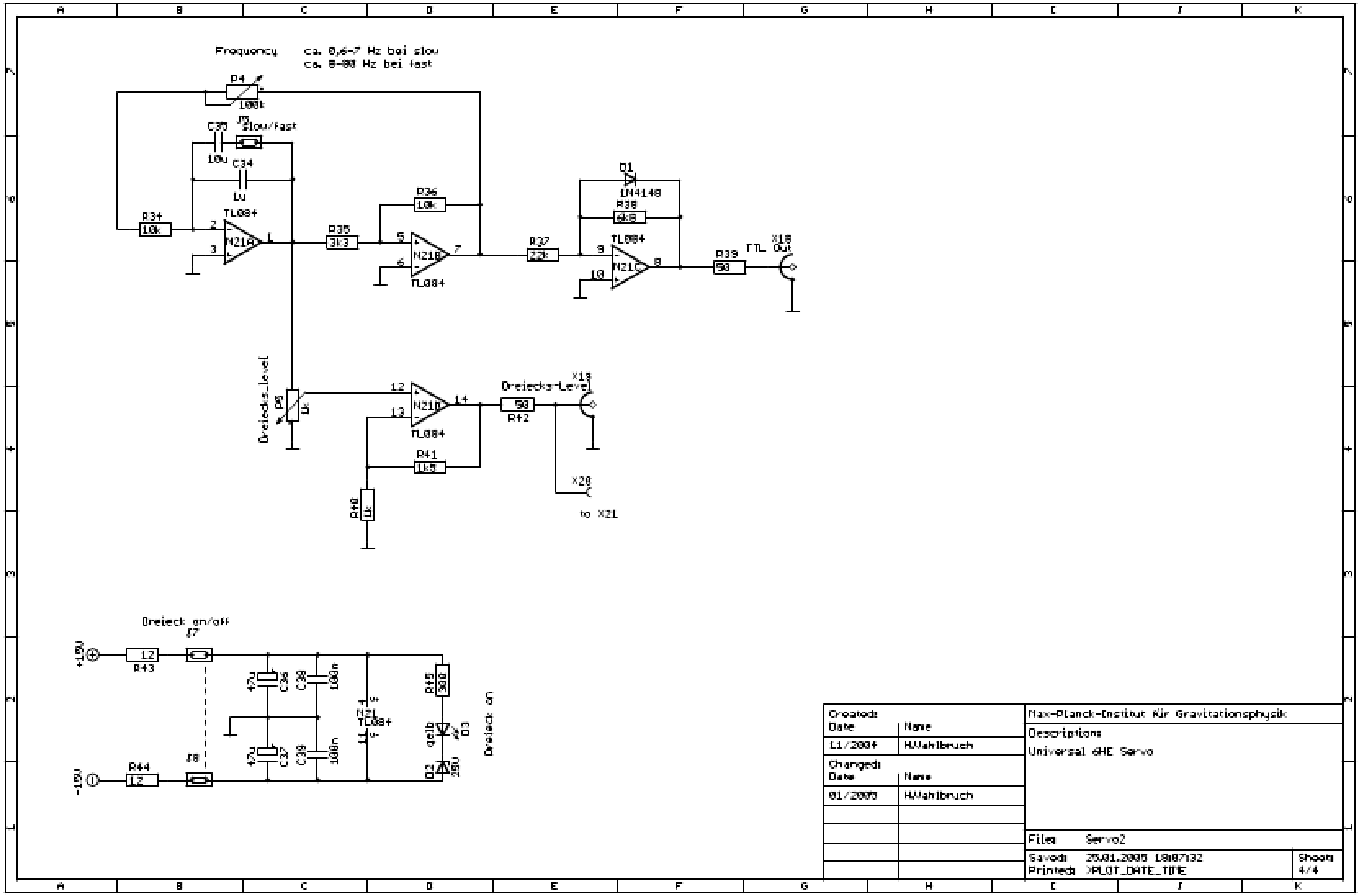

Figure D.7.: Servo. Part 3/3

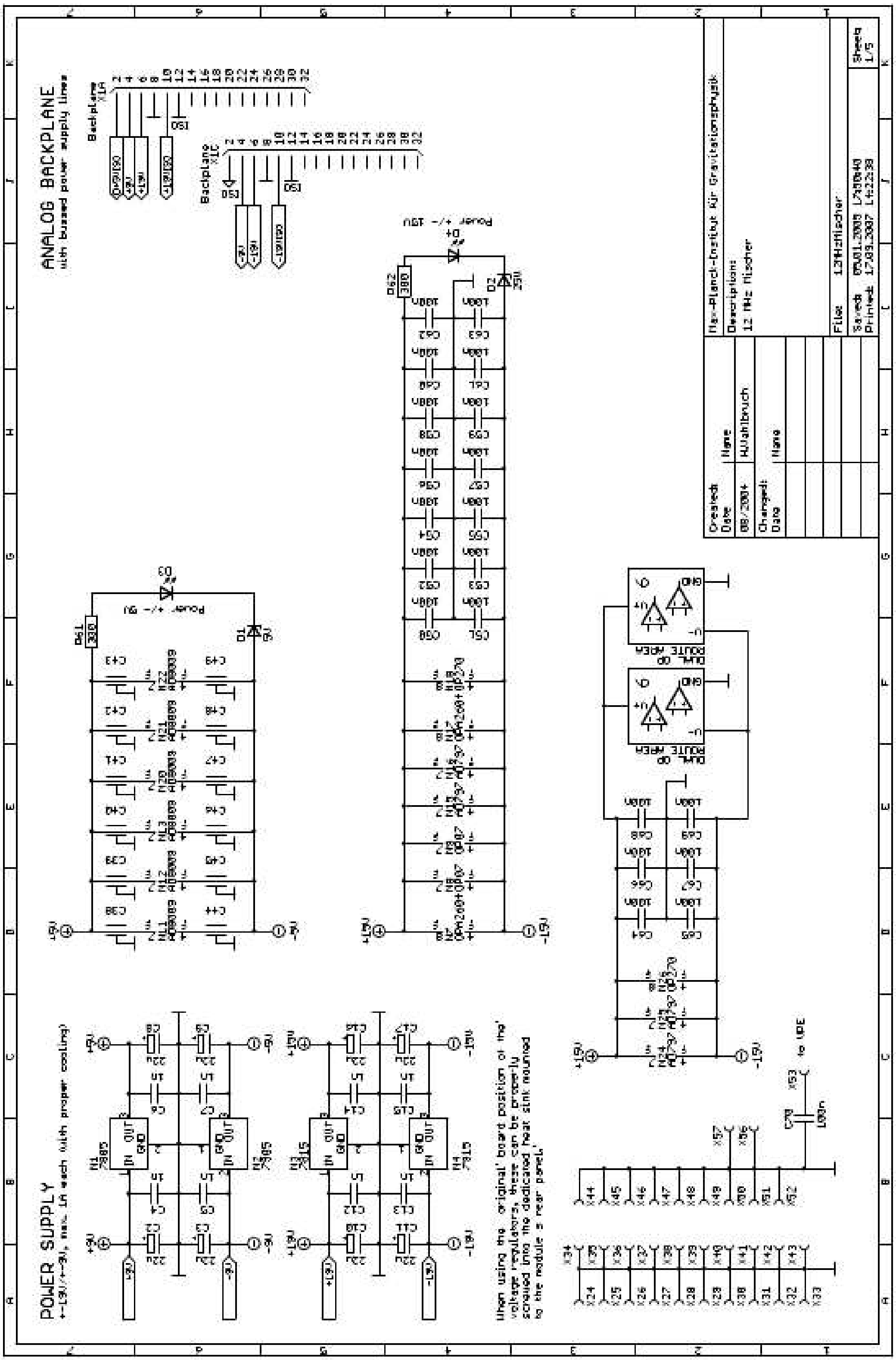

Figure D.8.: Mixer. Part 1/4

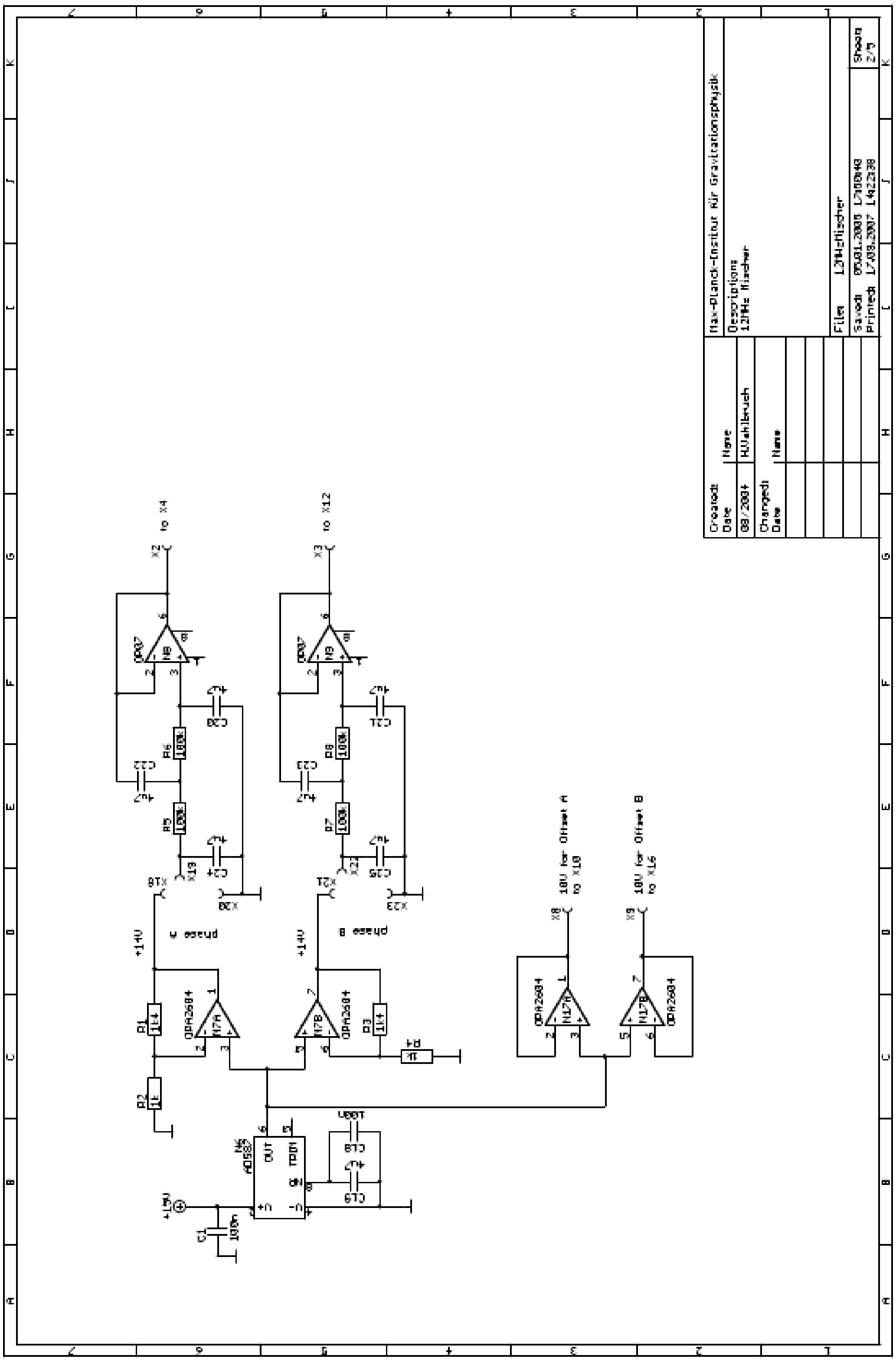

Figure D.9.: Mixer. Part 2/4

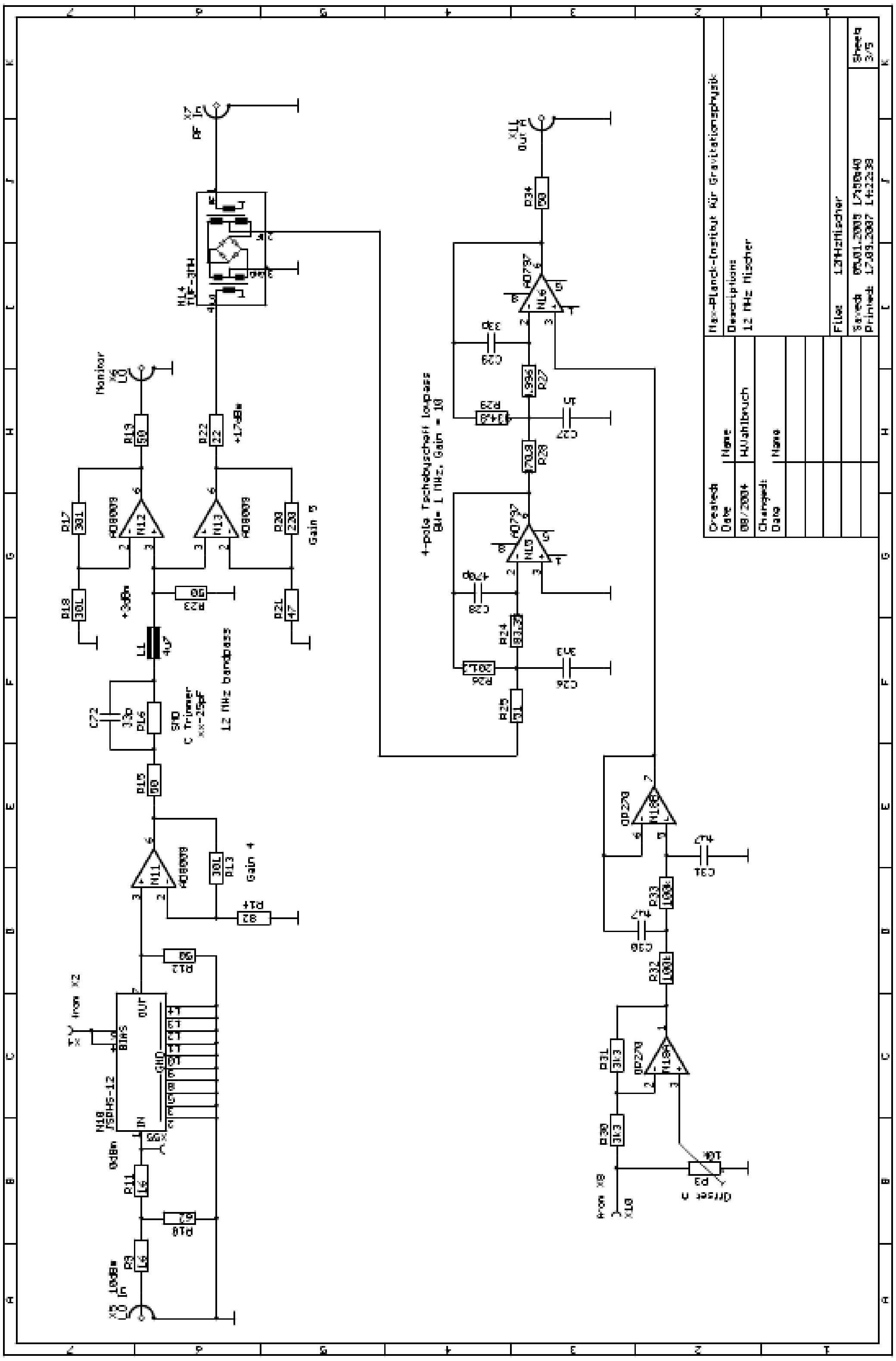

Figure D.10.: Mixer. Part 3/4

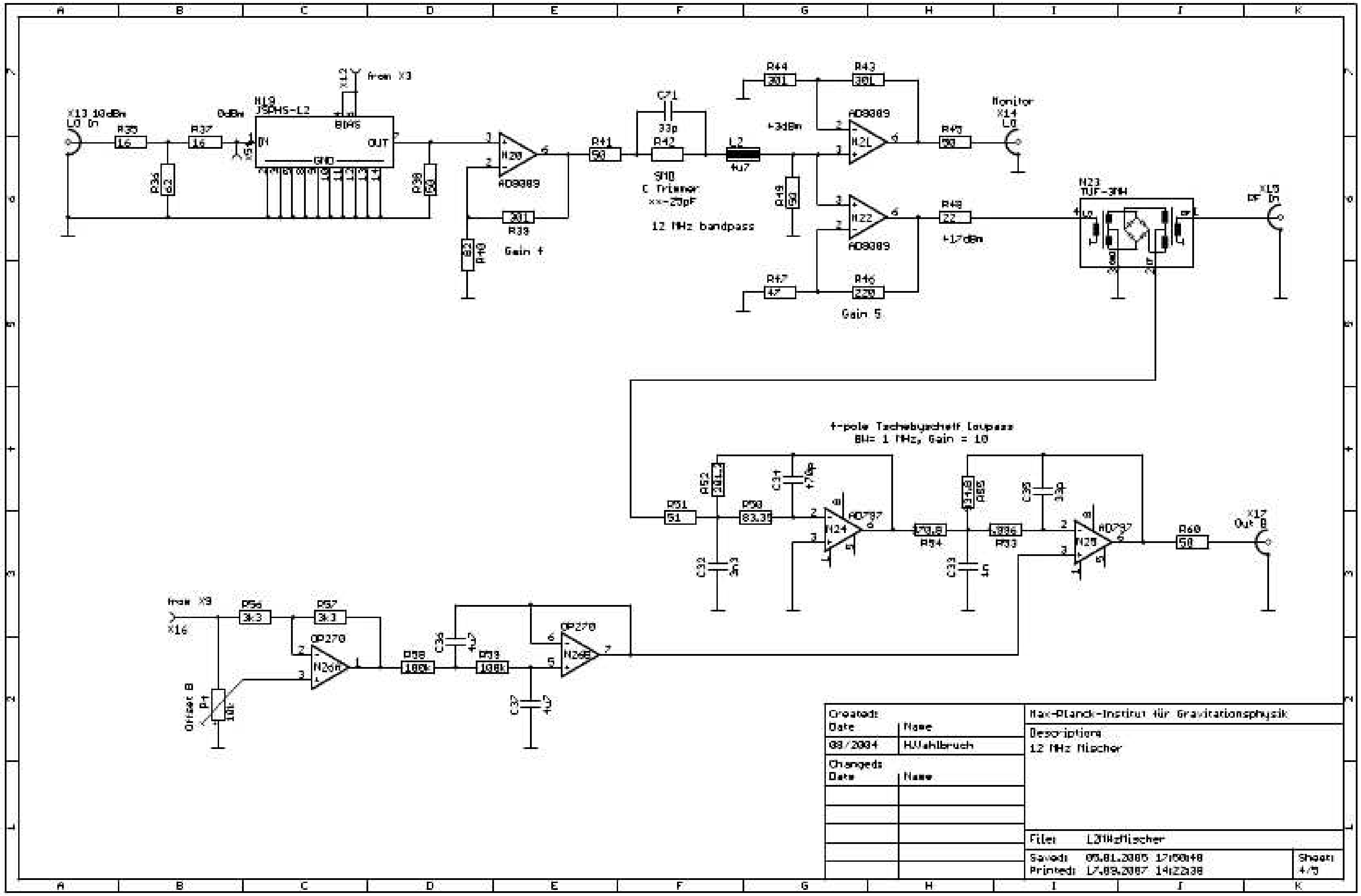

Figure D.11.: Mixer. Part 4/4

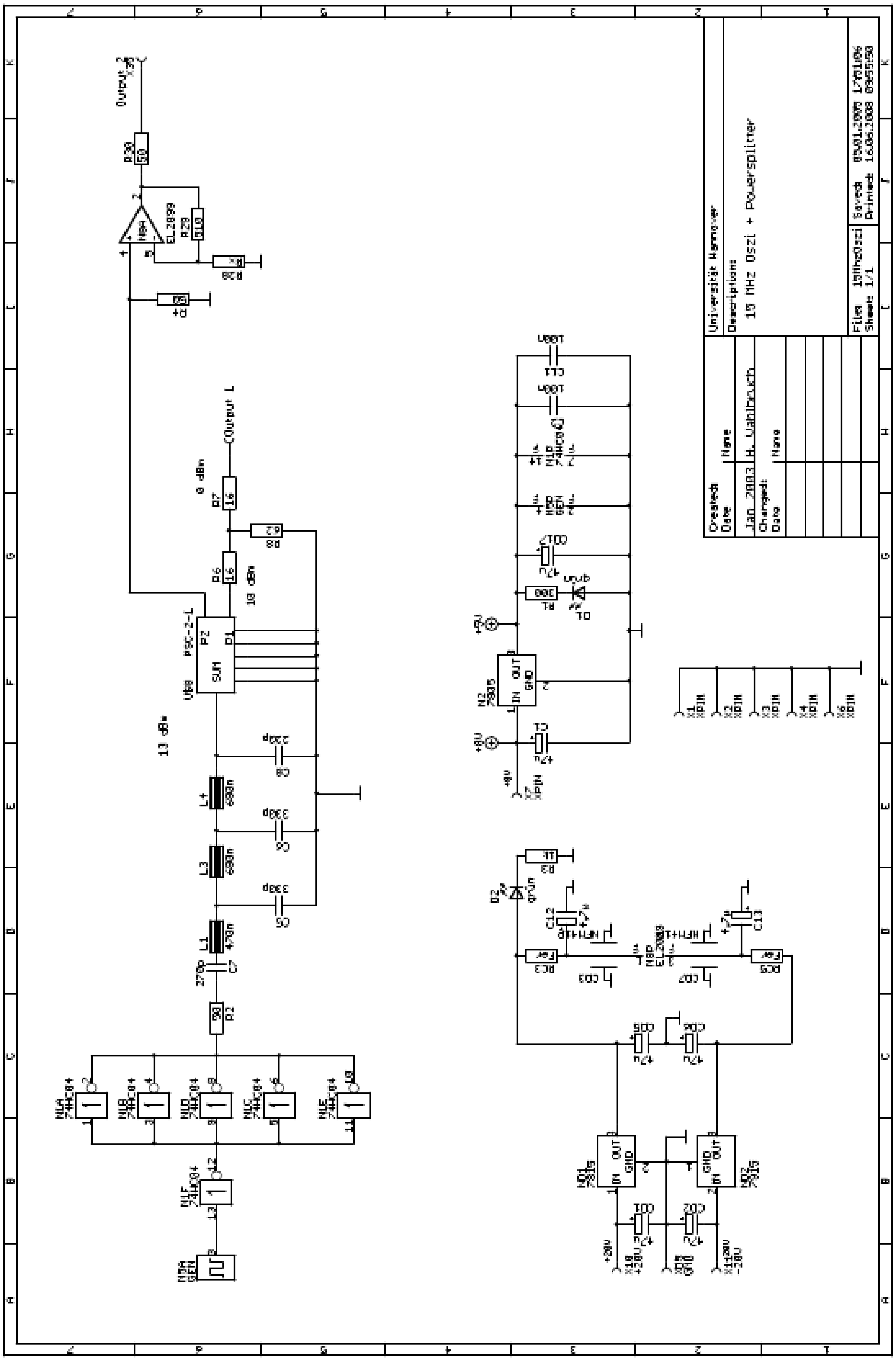

Figure D.12.: Oscillator.

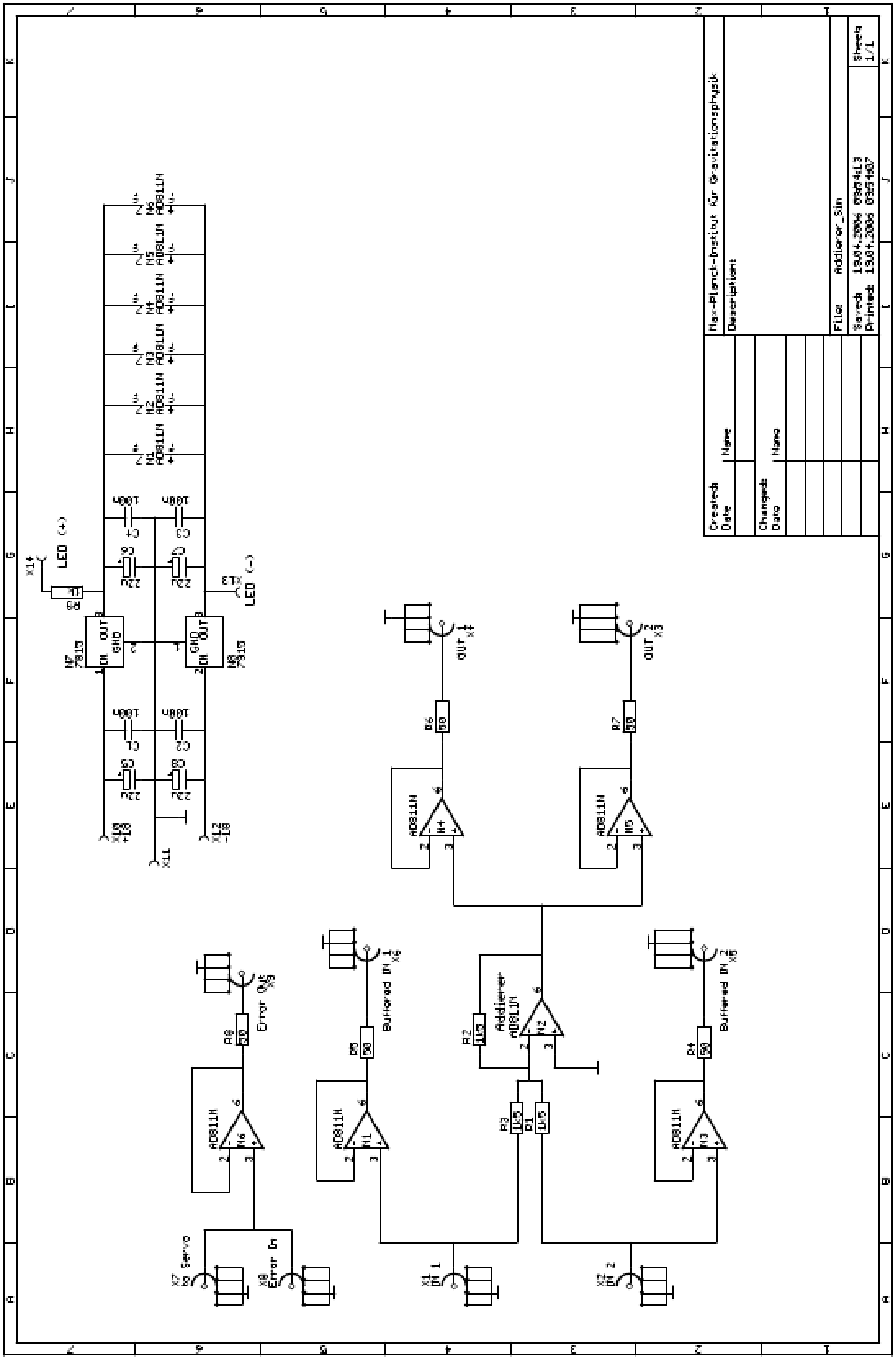

Figure D.13.: Active buffer.

Bibliography

[AAA+08] F Acernese, M Alshourbagy, P Amico, F Antonucci, S Aoudia, K G Arun, P Astone, S Avino, L Baggio, G Ballardin, F Barone, L Barsotti, M Barsuglia, Th S Bauer, S Bigotta, S Birindelli, M A Bizouard, C Boccara, F Bondu, L Bosi, S Braccini, C Bradaschia, A Brillet, V Brisson, D Buskulic, G Cagnoli, E Calloni, E Campagna, F Carbognani, F Cavalier, R Cavalieri, G Cella, E Cesarini, E Chassande-Mottin, S Chatterji, F Cleva, E Coccia, C Corda, A Corsi, F Cottone, J-P Coulon, E Cuoco, S D'Antonio, A Dari, V Dattilo, M Davier, R De Rosa, M Del Prete, L Di Fiore, A Di Lieto, M Di Paolo Emilio, A Di Virgilio, M Evans, V Fafone, I Ferrante, F Fidecaro, I Fiori, R Flaminio, J-D Fournier, S Frasca, F Frasconi, L Gammaitoni, F Garufi, E Genin, A Gennai, A Giazotto, V Granata, C Greverie, D Grosjean, G Guidi, S Hamdani, S Hebri, H Heitmann, P Hello, D Huet, P La Penna, M Laval, N Leroy, N Letendre, B Lopez, M Lorenzini, V Loriette, G Losurdo, J-M Mackowski, E Majorana, N Man, M Mantovani, F Marchesoni, F Marion, J Marque, F Martelli, A Masserot, F Menzinger, L Milano, Y Minenkov, M Mohan, J Moreau, N Morgado, S Mosca, B Mours, I Neri, F Nocera, G Pagliaroli, C Palomba, F Paoletti, S Pardi, A Pasqualetti, R Passaquieti, D Passuello, F Piergiovanni, L Pinard, R Poggiani, M Punturo, P Puppo, O Rabaste, P Rapagnani, T Regimbau, A Remillieux, F Ricci, I Ricciardi, A Rocchi, L Rolland, R Romano, P Ruggi, D Sentenac, S Solimeno, B L Swinkels, R Terenzi, A Toncelli, M Tonelli, E Tournefier, F Travasso, G Vajente, J F J van den Brand, S van der Putten, D Verkindt, F Vetrano, A Viceré, J-Y Vinet, H Vocca, and M Yvert. Virgo status. *Classical and Quantum Gravity*, 25(18):184001 (9pp), 2008. 8, 23

[AAB$^+$08] R. Abbott, R. Adhikari, S. Ballmer, L. Barsotti, M. Evans, P. Fritschel, V. Frolov, G. Mueller, B. Slagmolen, and S. Waldman. Advligo interferometer sensing and control conceptual design. Technical Report LIGO-T070247-00-I, LIGO, 2008. 134, 138

[AET99] J. W. Armstrong, F. B. Estabrook, and M. Tinto. Time-Delay Interferometry for Space-based Gravitational Wave Searches. *The Astrophysical Journal*, 527:814–826, 1999. 29

[AET03] J. W. Armstrong, F. B. Estabrook, and M. Tinto. Time delay interferometry. *Classical and Quantum Gravity*, 20:283–+, May 2003. 29

[Bac98] H. A. Bachor. *A guide to experiments in Quantum Optics*. Wiley-VCH, 1998. 80, 89, 106

[BBB$^+$01] G. Ballardin, L. Bracci, S. Braccini, C. Bradaschia, C. Casciano, G. Calamai, R. Cavalieri, R. Cecchi, G. Cella, E. Cuoco, E. D'Ambrosio, V. Dattilo, A. di Virgilio, L. Fabbroni, F. Fidecaro,

F. Frasconi, A. Gaddi, A. Gennai, G. Gennaro, A. Giazotto, G. Losurdo, L. Holloway, P. La Penna, F. Lelli, E. Majorana, M. Mazzoni, F. Paoletti, M. Pasotti, A. Pasqualetti, R. Passaquieti, D. Passuello, R. Poggiani, P. Puppo, F. Raffaelli, P. Rapagnani, F. Ricci, P. Ruggi, R. Stanga, R. Taddei, F. Vetrano, A. Vicerè, and Z. Zhang. Measurement of the VIRGO superattenuator performance for seismic noise suppression. *Review of Scientific Instruments*, 72:3643–3652, 2001. 18

[Bla01] E. D. Black. An introduction to Pound-Drever-Hall laser frequency stabilization. *American Journal of Physics*, 69:79–87, 2001. 74

[BM72] D. Bramanti and K. Maischberger. Construction and operation of a Weber-type gravitational-wave detector and of a divided-bar prototype. *Nuovo Cimento Lettere*, 4:1007–1013, 1972. 2

[BV02] S. Braccini and VIRGO Collaboration. The VIRGO suspensions. *Classical and Quantum Gravity*, 19:1623–1629, April 2002. 19

[BW99] B. C. Barish and R. Weiss. LIGO and the detection of gravitational waves. *Physics Today*, 52:44–50, 1999. 8

[Cav80] C. M. Caves. Quantum-Mechanical Radiation-Pressure Fluctuations in an Interferometer. *Physical Review Letters*, 45:75–79, 1980. 15, 16

[Cav81] C.M. Caves. Quantum-mechanical noise in an interferometer. *Physical Review D*, 23:1693–1708, 1981. 15

[CDKME09] Y. Chen, S. L. Danilishin, F. Y. Khalili, and H. Muller-

Ebhardt. Qnd measurements for future gravitational-wave detectors. *arXiv:0910.0319v1*, 2009. 29

[Che07] S. Chelkowski. *Squeezed Light and Laser Interferometric Gravitational Wave Detectors*. PhD thesis, University of Hannover, 2007. 6, 9, 57, 58

[CK06] Y. Chen and S. Kawamura. Displacement- and timing-noise-free gravitational-wave detection. *Physical Review Letters*, 96(23):231102–+, 2006. 3, 34

[CLS$^+$06] S. Chatterji, A. Lazzarini, L. Stein, P. J. Sutton, A. Searle, and M. Tinto. Coherent network analysis technique for discriminating gravitational-wave bursts from instrumental noise. *Phys. Rev. D*, 74(8):082005–+, 2006. 30

[Cor08] T. R. Corbitt. *Quantum Noise and Radiation Pressure Effects in High Power Optical Interferometers*. PhD thesis, MASSACHUSETTS INSTITUTE OF TECHNOLOGY, 2008. 17

[CPS$^+$06] Y. Chen, A. Pai, K. Somiya, S. Kawamura, S. Sato, K. Kokeyama, R. L. Ward, K. Goda, and E. E. Mikhailov. Interferometers for displacement-noise-free gravitational-wave detection. *Physical Review Letters*, 97(15):151103–+, 2006. 3, 34, 35

[Cut98] C. Cutler. Angular resolution of the LISA gravitational wave detector. *Phys. Rev. D*, 57:7089–7102, 1998. 30

[CYWM00] J. B. Camp, H. Yamamoto, S. E. Whitcomb, and D. E. McClelland. Analysis of light noise sources in a recycled Michelson interferometer withFabryPerotarms. *Journal of the Optical Society of America A*, 17:120–128, 2000. 17

[DFT91] J. C. Doyle, B. A. Francis, and A. R. Tannenbaum. *Feedback Control Theory*. Prentice Hall Professional Technical Reference, 1991. 62

[EBN$^+$09] M. P. Edgar, B. W. Barr, J. Nelson, M. V. Plissi, K. A. Strain, O. Burmeister, M. Britzger, K. Danzmann, R. Schnabel, T. Clausnitzer, F. Brückner, E.-B. Kley, and A. Tünnermann. Experimental demonstration of a suspended diffractively coupled optical cavity. *Opt. Lett.*, 34(20):3184–3186, 2009. 29

[ETA00] F. B. Estabrook, M. Tinto, and J. W. Armstrong. Time-delay analysis of LISA gravitational wave data: Elimination of spacecraft motion effects. *Phys.Rev.D*, 62(4):042002–+, 2000. 29

[ETd] Einstein gravitational-wave Telescope 2007 Design study proposal submitted to European Union. Framework 7, INFRA-2007-2.1-01, Design studies for research infrastructures in all S&T fields. 29

[ETh07] H. Lück *et al.* 2007. Plans for E.T. (Einstein Telescope). A European 3rd generation gravitational wave observatory, presented at the AMALDI 7 conference, Sydney. 29

[FBBM86] D. Fattaccioli, A. Boulharts, A. Brillet, and C. N. Man. Sensitivity of multipass and fabry-perot delay lines to small misalignments. *Journal of Optics*, 17(3):115–127, 1986. 10

[FCH$^+$09] A. Freise, S. Chelkowski, S. Hild, W. Del Pozzo, A. Perreca, and A. Vecchio. Triple michelson interferometer for a third-generation gravitational wave detector. *Classical and Quantum Gravity*, 26(8):085012 (14pp), 2009. 3, 28, 29, 30, 31

[FFG+05] R. Flaminio, A. Freise, A. Gennai, P. Hello, P. La Penna, G. Losurdo, H. Lueck, N. Man, A. Masserot, B. Mours, M. Punturo, A. Spallicci, and A. Vicerre. Advanced virgo white paper. Technical Report VIR-NOT-DIR-1390-304, Virgo, 2005. 25

[FH05] É. É. Flanagan and S. A. Hughes. The basics of gravitational wave theory. *New Journal of Physics*, 7:204, 2005. 41

[FHL+04] A Freise, G Heinzel, H Lück, R Schilling, B Willke, and K Danzmann. Frequency-domain interferometer simulation with higher-order spatial modes. *Classical and Quantum Gravity*, 21(5):S1067–S1074, 2004. 88

[FHS+00] A. Freise, G. Heinzel, K. A. Strain, J. Mizuno, K. D. Skeldon, H. Lück, B. Willke, R. Schilling, A. Rüdiger, W. Winkler, and K. Danzmann. Demonstration of detuned dual recycling at the Garching 30 m laser interferometer. *Physics Letters A*, 277:135–142, 2000. 9, 27

[Fri03] P. Fritschel. Gravitational-wave detection. Edited by M. Cruise and P. Saulson, Proc. SPIE 4856, 282291, 2003. 25

[Gos04] S. Gossler. *The suspension systems of the interferometric gravitational-wave detector GEO600*. PhD thesis, Universitat Hannover, 2004. 19

[Har03] J.B. Hartle. *Gravity: An introduction to Einstein's general relativity*. Information and system science series. Addison Wesley. San Francisco, CA, 2003. 1

[Hei95] G. Heinzel. Resonant sideband extraction – neuartige interferometrie fuerr gravitationswellendetektoren. Master's thesis, Universitaet Hannover, 1995. 60

[Hei99] G. Heinzel. *Advanced optical techniques for laser-interferometric gravitational-wave detectors.* PhD thesis, MPI fuer Quantenoptik, 1999. 26, 71

[Hil07] S. Hild. *Beyond the first Generation: Extending the science range of the Gravitational Wave Detector GEO600.* PhD thesis, Hannover, February 2007. 28

[HMPF09] S. Hild, M. Mantovani, A. Perreca, and A. Freise. Advanced virgo design: The advanced ligo approach for choosing modulation frequencies. Technical Report VIR-066A-08, Virgo, 2009. xv, 134, 135, 136, 139, 141, 143, 145

[HRH$^+$97] C. C. Harb, T. C. Ralph, E. H. Huntington, D. E. McClelland, H.-A. Bachor, and I. Freitag. Intensity-noise dependence of Nd:YAG lasers on their diodelaser pump source. *J. Opt. Soc. Am. B*, 60:225, 1997. 57

[HRS05] J. Hough, S. Rowan, and B. S. Sathyaprakash. The search for gravitational waves. *Journal of Physics B Atomic Molecular Physics*, 38, May 2005. 15, 18, 21, 22, 24, 26

[HSM$^+$98] G. Heinzel, K. A. Strain, J. Mizuno, K. D. Skeldon, B. Willke, W. Winkler, R. Schilling, A. Rüdiger, and K. Danzmann. Experimental demonstration of a suspended dual recycling interferometer for gravitational wave detection. *Phys. Rev. Lett.*, 81(25):5493–5496, December 1998. 9, 27

[HT75] R. A. Hulse and J. H. Taylor. Discovery of a pulsar in a binary system. *The Astrophysical Journal*, 195:L51–L53, 1975. 2

[HT98] S. A. Hughes and K. S. Thorne. Seismic gravity-gradient noise in interferometric gravitational-wave detectors. *Phys. Rev. D*, 58(12):122002, November 1998. 29

[HWK$^+$91] J. Hough, H. Ward, G.A. Kerr, N.L. Mackenzie, B.J. Meers, G.P. Newton, D.I. Robertson, N.A. Robertson, and R. Schilling. The stabilisation of lasers for interferometric gravitational wave detectors. In D.G. Blair, editor, *The detection of gravitational waves*, pages 329–352. Cambridge University Press, 1991. 17

[JKS98] P. Jaranowski, A. Królak, and B. F. Schutz. Data analysis of gravitational-wave signals from spinning neutron stars: The signal and its detection. *Phys. Rev. D*, 58(6):063001–+, 1998. 30

[KC04] S. Kawamura and Y. Chen. Displacement-noise-free gravitational-wave detection. *Physical Review Letters*, 93(21):211103–+, 2004. 3, 33

[KSN$^+$09] K. Kokeyama, S. Sato, A. Nishizawa, S. Kawamura, Yanbei Chen, and Akio Sugamoto. Development of a displacement- and frequency-noise-free interferometer in a 3d configuration for gravitational wave detection. *Physical Review Letters*, 103(17):171101, 2009. 34

[KtLC06] K. Kuroda and the LCGT Collaboration. The status of lcgt. *Classical* *and Quantum Gravity*, 23(8):S215–S221, 2006. 25

[Lev98] Y. Levin. Internal thermal noise in the LIGO test masses: A direct approach. *Phys. Rev. D*, 57:659–663, January 1998. 20

[Mee88] B. J. Meers. Recycling in laser-interferometric gravitational-wave detectors. *Phys. Rev. D*, 38:2317–2326, 1988. 9, 12

[Miz95] J. Mizuno. *Comparison of optical configurations for laser-interferoemtric gravitational-wave detectors*. PhD thesis, Hannover, 1995. 7, 14

[MS91] B. J. Meers and K. A. Strain. Modulation, signal, and quantum noise in interferometers. *Phys. Rev. A*, 44:4693–4703, 1991. 9, 27

[New01] Manual for the new focus electro-optic phase modulator, model series 400x, 2001. 64, 65, 70

[PCHF10] A. Perreca, S. Chelkowski, S. Hild, and A. Freise. Experimental demonstration of a displacement noise free interferometry scheme for gravitational wave detectors showing displacement noise reduction at low frequencies. *Physical Review D*, 81(6), 2010. 105, 127

[Pun04] M. Punturo. The Virgo sensitivity curve. *Virgo note VIR-NOT-PER-1390-51*, 2004. 22

[Rak05] M. Rakhmanov. Response of test masses to gravitational waves in the local Lorentz gauge. *Phys. Rev. D*, 71(8):084003–+, 2005. 34, 41, 42

[RV08] A. A. Rakhubovsky and S. P. Vyatchanin. Displacement noise free gravitational wave detection with two fabry-perot cavities. *arXiv:0807.3824v1 [gr-qc]*, 1(1), 2008. 105

[Sau84] P. R. Saulson. Terrestrial gravitational noise on a gravitational wave antenna. *Phys. Rev. D*, 30(4):732–736, August 1984. 19

[Sau90] P. R. Saulson. Thermal noise in mechanical experiments. *Phys.Rev. D*, 42:2437–2445, 1990. 20

[Sau94] P.R. Saulson. *Fundamentals of Interferometric Gravitational Wave Detectors*. World Scientific, 1994. 6, 7, 11, 15, 18, 21

[SKW$^+$07] S. Sato, K. Kokeyama, R. L. Ward, S. Kawamura, Y. Chen, A. Pai, and K. Somiya. Demonstration of displacement- and frequency-noise-free laser interferometry using bidirectional mach-zehnder interferometers. *Physical Review Letters*, 98(14):141101–+, 2007. 34

[SM91] K. A. Strain and B. J. Meers. Experimental demonstration of dual recycling for interferometric gravitational-wave detectors. *Physical Review Letters*, 66:1391–1394, 1991. 9, 27

[SY09] K. Somiya and K. Yamamoto. Coating thermal noise of a finite-size cylindrical mirror. *Physical Review D (Particles, Fields, Gravitation, and Cosmology)*, 79(10):102004, 2009. 20

[TA99] M. Tinto and J. W. Armstrong. Cancellation of laser noise in an unequal-arm interferometer detector of gravitational radiation. *Phys.Rev.D*, 59(10):102003–+, May 1999. 29

[Tar07] S. P. Tarabrin. Interaction of plane gravitational waves with a fabry-perot cavity in the local lorentz frame. *Phys. Rev. D*, 75(10):102002–+, May 2007. 41, 42

[TS08] S. P. Tarabrin and A. A. Seleznyov. Optical position meters analyzed in the noninertial reference frames. *Physical Review D (Particles, Fields, Gravitation, and Cosmology)*, 78(6):062001, 2008. 42

[TTA+07] D. Tatsumi, R. Takahashi, K. Arai, N. Nakagawa, K. Agatsuma, T. Yamazaki, M. Fukushima, M.-K. Fujimoto, A. Takamori, A. Bertolini, V. Sannibale, R. DeSalvo, S. Márka, M. Ando, K. Tsubono, T. Akutsu, K. Yamamoto, H. Ishitsuka, T. Uchiyama, S. Miyoki, M. Ohashi, K. Kuroda, N. Awaya, N. Kanda, A. Araya, S. Telada, T. Tomaru, T. Haruyama, A. Yamamoto, N. Sato, T. Suzuki, and T. Shintomi. Current status of Japanese detectors. *Classical and Quantum Gravity*, 24:399–+, 2007. 8

[TV08] S. P. Tarabrin and S. P. Vyatchanin. Displacement-noise-free gravitational-wave detection with a single fabry-perot cavity: A toy model. *Phys. Letters A*, 372:6801–6812, 2008. 3, 34, 35, 36, 37, 38, 39, 40, 42, 44, 45, 46, 47, 50, 52, 55, 71, 77, 105, 108, 124, 127

[TW99] K. S. Thorne and C. J. Winstein. Human gravity-gradient noise in interferometric gravitational-wave detectors. *Phys. Rev. D*, 60(8):082001–+, 1999. 29

[VCH+05] H. Vahlbruch, S. Chelkowski, B. Hage, A. Franzen, K. Danzmann, and R. Schnabel. Demonstration of a squeezed-light-enhanced power- and signal-recycled michelson interferometer. *Phys. Rev. Lett.*, 95(21):211102, November 2005. 29

[WAA+04] B Willke, P Aufmuth, C Aulbert, S Babak, R Balasubramanian, B W Barr, S Berukoff, G Cagnoli, C A Cantley, M M Casey, S Chelkowski, D Churches, C N Colacino, D R M Crooks, C Cutler, K Danzmann, R Davies, R J Dupuis, E Elliffe, C Fallnich, A Freise, S Goßler, A Grant, H Grote, S Grunewald, J Harms, G Heinzel, I S Heng, A Hepstonstall, M Heurs, M Hewitson, S Hild, J Hough, R Ingley, Y Itoh, O Jennrich, R Jones, S H Hutter, K Kawabe, C Killow, K Kötter, B Krishnan, V Leonhardt, H Lück, B Machenschalk, M Malec, R A Mercer, C Messenger, S Mohanty, K Mossavi, S Mukherjee, S Nagano, G P Newton, M A Papa, M Perreur-Lloyd, M Pitkin, M V Plissi, V Quetschke, V Re, S Reid, L Ribichini, D I Robertson, N A Robertson, S Rowan, A Rüdiger, B S Sathyaprakash, R Schilling, R Schnabel, B F Schutz, F Seifert, A M Sintes, J R Smith, P H Sneddon, K A Strain, I Taylor, C I Torrie, C Ungarelli, A Vecchio, H Ward, U Weiland, H Welling, P Williams, W Winkler, G Woan, and I Zawischa. Status of geo 600. *Classical and Quantum Gravity*, 21(5):S417–S423, 2004. 9

[WAA$^+$06] B Willke, P Ajith, B Allen, P Aufmuth, C Aulbert, S Babak, R Balasubramanian, B W Barr, S Berukoff, A Bunkowski, G Cagnoli, C A Cantley, M M Casey, S Chelkowski, Y Chen, D Churches, T Cokelaer, C N Colacino, D R M Crooks, C Cutler, K Danzmann, R J Dupuis, E Elliffe, C Fallnich, A Franzen, A Freise, I Gholami, S Goßler, A Grant, H Grote, S Grunewald, J Harms, B Hage, G Heinzel, I S Heng, A Hepstonstall, M Heurs, M Hewitson, S Hild, J Hough, Y Itoh, G Jones, R Jones, S H Huttner, K Kötter, B Krishnan, P Kwee, H Lück, M Luna, B Machenschalk, M Malec, R A Mercer, T Meier, C Messenger, S Mohanty, K Mossavi, S Mukherjee, P Murray, G P Newton, M A Papa, M Perreur-Lloyd, M Pitkin, M V Plissi, R Prix, V Quetschke, V Re, T Regimbau, H Rehbein, S Reid, L Ribichini, D I Robertson, N A Robertson, C Robinson, J D Romano, S Rowan, A Rüdiger, B S Sathyaprakash, R Schilling, R Schnabel, B F Schutz, F Seifert, A M Sintes, J R Smith, P H Sneddon, K A Strain, I Taylor, R Taylor, A Thüring, C Ungarelli, H Vahlbruch, A Vecchio, J Veitch, H Ward, U Weiland, H Welling, L Wen, P Williams, W Winkler, G Woan, and R Zhu. The geo-hf project. *Classical and Quantum Gravity*, 23(8):S207–S214, 2006. 25

[Yar89] A. Yariv. *Quantum electronics.* J. Wiley & Sons, 1989. 70

Acknowledgements

I have to thank my supervisor Andreas Freise who has been the one who gave me the opportunity to be an his students. May be I was not ready to be so far from home, but Andreas was my opportunity to step forward in my professional life. He has been sometimes apparently very severe and sometimes very nice, reading between the lines always what I was not able to read and giving me exactly the right hints I needed at moment to grow up, either for scientific or private life. I will be forever in debt with him. I learnt a lot from Simon Chelkowski, who was my scientific guide for my experiment. He was most of the time stressed by me and he repaid stressing me as well. Apparently it could have been misleading but we worked very well in a very productive way. Stefan Hild offered always the chance to speak with him and gain from his experience which has been helpful for my work and my attitude as well. Thanks to Andreas, Simon and Stefan together I could achieve my results.

I also would like to thank S.P. Tarabrin and S.P. Vyatchanin for their patience in explaining their DFI scheme to all of us and for the many fruitful discussion that followed. In particular S.P. Tarabrin was over stressed by me in the last period of my work.

I had many difficult moments and as much as good moments during my phD. I must say that Alberto Vecchio has been always present from each point of view and in any cases. He might not be realized how important was for me. Unreplaceable.

A special thank to Adriana Gargiulo who has been helping me constantly for everything and always illuminating my life: She has been my SUN...and my SEA...

Thanks to my colleagues Jonathan Hallam, Paul Fulda, Deepali Lodhia, and Hasnain Panjwani for their kindness in proof reading the english of my thesis, to Walter Del Pozzo and Genni Testa for many useful discussions and to David Stops, the best assistent computer manager I could have met, who made my laptop always working (because of him I had to work all the time with no excuse...)

At the end of the first year I had many difficulties in my private life and I must thank firstly all the members of my family (always present) especially my sister Teresa, reminding my mother in many occasions, to my fantastic friends Conny, Rino, and Luisa for their crabbing me out of ”the deepest place on the earth”, supported by Marco Capuano, Mariano Biasiucci, Pasquale D'Angelo, Felicia De Laurentis and the always present Biagio Spinelli. I had many and many friends in Birmingham who I cannot name all of them here but I need to specially thank to Giacomo Volpe who was always available for me (...and much more) and Ludovico Carbone with whom I spent a lot of time. Alberto Sesana for his encouraging me when I was experiencing ”some” difficulties. Ali Dariush for his help when me and Walter arrived in Birmingham and Smriti Marhajan for her ”strong” kindness. Once again I say thanks to Walter who I met the first time at the airport in Rome for the way out to Birmingham. We shared together the house for more than two years and it was a great experience, later continued, thanks to Luca Scarpantonio (my personal trainer) for this and many other things, with Cosimo Ducani and Natalia Calle Alonso; they have been very nice with me.

Finally I have to say that all this results and my life in Birmingham have been possible for me only because my daughter Lucienne gives me always the power to do things. Unfortunately this power fights with my being so far from her but here the beauty of being his father comes, since she let me feel the most lucky guy in the world. ”Once again” I have to say that I’m honored to be the Lucienne’s father.